CHARACTERIZATION OF TYPE-II GaSb QUANTUM RINGS IN GaAs SOLAR CELLS

Juanita Saroj James Asirvatham

M.Sc. (Physics); M.Tech. (Nanotechnology)

Lancaster University

Physics

Department of Physics

Lancaster University

September 2015

A thesis submitted to Lancaster University for the degree of Doctor of Philosophy in the Faculty of Science and Technology

Contents

CHARACTERIZATION OF TYPE-II GaSb QUANTUM RINGS IN GaAs SOLAR CELLS

Juanita Saroj James Asirvatham

September 2015

A thesis submitted to Lancaster University for the degree of Doctor of Philosophy in the Faculty of Science and Technology

Abstract

The use of nanostructured materials in solar cells enables one to tune their absorption properties leading to a better match to the solar spectrum and subsequently an increased photocurrent through the solar cell. Type II GaSb/GaAs quantum rings (QRs) can significantly extend the spectral response beyond the visible out towards 1.4 μm giving a near optimum band gap for concentrator solar cell applications. Also, in type II band alignment the electrons are weakly localized and the built in electric field drifts the electrons across the depletion region easily. However, the introduction of GaSb QRs in GaAs solar cells degrades the open circuit voltage (V_{oc}) and the incorporation of QRs needs to be optimized to minimize the V_{oc} degradation while maximizing short circuit current density (J_{sc}) enhancement due to sub-bandgap absorption. The analysis of the photoresponse under the white light illumination has shown that some photogenerated minority holes from the base region can be re-

captured by the QRs, which reduces the Jsc and the Voc. Hence, in this thesis, the carrier dynamics and extraction mechanisms occurring in the GaSb QRs is investigated by photoluminescence spectroscopy and current voltage characteristics. The characteristic S-shaped behaviour of the WL peak energy with increasing temperature indicates the prominent carrier trapping in the band tail states leading to potential fluctuations. Systematic measurements of dark current versus voltage characteristics are carried out from 100 to 290 K. Compared with the reference GaAs solar cell, the QRSC exhibits larger dark current, however its ideality factor n is similar at 290 K.

QRs are directly probed by using an infrared laser (1064 nm) where the photon energy is conveniently chosen below the bandgap of the GaAs matrix. This enables to investigate the carrier dynamics and extraction mechanisms occurring in the GaSb QRs under a high light concentration. The dependence of the photocurrent on the laser intensity, the bias and the temperature is also discussed. The QR photocurrent exhibits a linear dependence on the excitation intensity over several decades. The thermal activation energy was found to be weakly dependent on the incident light level and increased by only a few meV over several orders of excitation intensity. The magnitude of the relative absorption in QRs when directly probed by using a 1064 nm laser with an incident power density of ~ 2.6 W cm^{-2} is found to be ~ 1.4×10^{-4} per layer. The thermal escape rate of the holes was calculated and found to be ~ 10^{11} to 10^{12} s^{-1}, which is much faster than the radiative recombination rate 10^{9} s^{-1}. This behaviour is promising for concentrator solar cell development and has the potential to increase solar cell efficiency under a strong solar concentration.

Experiments have shown that QDs embedded in the depletion region could generate both additional photocurrent and dark current. The electron-hole recombination in QDs is the reason for the additional dark current which reduces the open circuit voltage and keeps the conversion efficiency of QD solar cells below the Shockley-Queisser limit. Therefore, the reduction in open circuit voltage and the influence of the location of QR layers and their delta doping within the solar cell is investigated in this work. Devices with 5 layers of delta doped QRs placed in the intrinsic, n and p regions of a GaAs solar cell are experimentally investigated and the deduced values of Jsc, Voc, Fill factor (FF), efficiency (η) are compared. A trade-off is needed to minimize the Voc degradation while maximizing the short circuit current density (Jsc) enhancement due to sub-bandgap absorption. The voltage recovery is attributed to the removal of the QDs from the high field region which reduces SRH recombination. The devices with p or n doped QDs placed in the flat band potential (p or n region) show a recovery in Jsc and Voc compared to devices with delta doped QDs placed in the depletion region. However there is less photocurrent arising from the absorption of sub-band gap photons. Furthermore, the long wavelength photoresponse of the n doped QRs placed in the n region shows a slight improvement compared to the control cell. The approach of placing QRs in the n region of the solar cell instead of the depletion region is a possible route towards increasing the conversion efficiency of QR solar cells.

The effect of the introduction of dopants on the morphology of GaSb/GaAs nanostructures is analyzed by HAADF-STEM. The results show the presence of well-developed GaSb QRs in both p-doped and n-doped heterostructures. However, in the undoped sample grown under the same conditions such well-developed QRs have not

been observed. It is found that p-doping with Be stimulates the formation of QRs, whereas n-doping with Te results in the formation of GaSb nanocups. Therefore, the introduction of dopants in the growth of GaSb nanostructures has a significant effect on their morphology.

Bias and temperature dependent EQE measurements are performed to understand the hole extraction from the QRs. In order to study the absorption strength of quantum dots and the various transition states, an approach to derive the below-bandgap absorption in GaSb/GaAs self-assembled quantum ring (QR) devices using room temperature external quantum efficiency measurement results is presented. The importance of incorporating an extended Urbach tail absorption in analyzing QR devices is demonstrated. The theoretically integrated absorbance via QR ground states is calculated as 1.04×10^{15} cm^{-1}s^{-1}, which is in a reasonable agreement with the experimental derived value 8.1×10^{15} cm^{-1}s^{-1}. The wetting layer and QR absorption contributions are separated from the tail absorption and their transition energies are calculated. Using these transition energies and the GaAs energy gap of 1.42 eV, the heavy hole confinement energies for the QRs (320 meV) and for the WL (120 meV) were estimated.

Declaration

This thesis is my own work and no portion of the work referred to in this thesis has been submitted in support of an application for another degree or qualification at this or any other institute of learning.

Acknowledgement

I express my foremost deepest gratitude to Professor Antony Krier for giving me the wonderful opportunity to pursue research under his guidance. This Research could not have been accomplished without his invaluable supervision and motivation.

I am grateful to Dr Peter Carrington for introducing me to Photoluminescence, I-V and Photoresponse measurements and also for growing my samples by MBE.

I thank Dr Susan Krier, Dr. A.R. Marshall, Dr. Abu Syed, Dr.Kylie O'Shea, Dr. Alex Robson, Dr. Lu Qi, Dr. Ezekiel Anyebe for their helpful assistance and support in doing experiments. I also thank Dr.Atif Aziz for teaching me how to process solar cells and use the clean room tools.

I would like to thank Hiromi Fujita from Asahi-Kasei Microdevices, Japan for his valuable input in my research paper and also for growing my samples by MBE.

I am also thankful to Dr Isodiana Crupi for helping in doing solar cell characterization during my secondment at IMM,Catania.

I owe my sincere thanks to EU Marie Curie Photonics training network (EC Grant agreement Number: 264687) for providing funds for this research.

Above all, I express my warm thanks to my beloved husband, my daughter and my parents for their constant love, support and encouragement and I feel very blessed to have them all.

Publications

"Delta doping and positioning effects of type II GaSb quantum dots in GaAs solar cell" **Juanita Saroj James**, Hiromi Fujita, N. Fernández-Delgado, M. Herrera, S. I. Molina, Andrew R.J. Marshall, Anthony Krier, Manuscript submitted at Materials Research Innovations'2015 (PVSAT-11 special issue)

"Effect of doping on the morphology of GaSb/GaAs nanostructures" N. Fernández-Delgado, M. Herrera, C. Castro, S. Duguay, **J. S. James**, A. Krier, S. I. Molina,Applied surface science '2015

"Open-circuit voltage recovery in type II GaSb/GaAs quantum ring solar cells under high concentration" Hiromi Fujita, Peter J. Carrington, Magnus C. Wagener, Johannes R. Botha, Andrew R. J. Marshall, **Juanita James**, Anthony Krier, Kan-Hua Lee and Nicholas John Ekins-Daukes, Prog. Photovolt: Res. Appl. (2015)

"Carrier extraction behaviour in type II GaSb/GaAs quantum ring solar cells" H. Fujita, **J. James**, P. J. Carrington, A. R. J. Marshall, A. Krier, M. C. Wagener, and J. R. Botha, Semicond. Sci. Tech., 29 (3), 035014 (2014).

"Carrier extraction from GaSb quantum rings in GaAs solar cells using direct laser excitation" **J. S. James**, H. Fujita, P. J. Carrington, A. R. J. Marshall, and A. Krier, IET Optoelectronics, 8 (2), 76–80 (2014).

Antimonide quantum dot nanostructures for novel photonic device applications
Krier, A., Carrington, P., Zhuang, Q., Young, R., Hayne, M., Lu, Q., James Asirvatham, J., Wagener, M., Botha, J. R., Koenraad, P. M. & Smakman, E. P. 5/11/2013 The wonder of nanotechnology: quantum optoelectronic devices and applications . SPIE -Research output: Contribution in Book/Report/Proceedings › Chapter (peer-reviewed)

Presentation at Conferences

Symposium, "The impact of surface science" by RSC Solid Surfaces Group and IOP Thin Films and Surfaces Group , Manchester, 12th December 2012 (Attended)

"Photoresponse of GaSb Quantum dots in GaAs solar cells using 1064 nm Laser excitation", UK Semiconductors Conference 2012, Sheffield (**awarded 3rd prize** for poster)

"GaSb Quantum dot solar cell with extended Photoresponse", Science and Technology Christmas Conference 2012, Lancaster, UK (**awarded 1st prize** for poster).

"Type II GaSb Quantum Dots for Solar Cells based on GaAs" **Juanita James**, H.Fujita*, P. J. Carrington , Q.D. Zhuang, A.R. Marshall & A. Krier, Semiconductor and Integrated OptoElectronics (SIOE), 2013 (Oral presentation)

"Delta doping and positioning effects of type II GaSb quantum dots in GaAs solar cell" **Juanita Saroj James**, Hiromi Fujita, N. Fernández-Delgado, M. Herrera, S. I. Molina, Andrew R.J. Marshall, Anthony Krier, 11th Photovoltaic Science Application and Technology (PVSAT-11) Conference and Exhibition, 2015, Leeds, UK (Oral presentation)

Chapter 1

Introduction

1.1. Global energy potential

Different forms of energy are being consumed to produce electricity, which are necessary for everyday life. In 2014 globally 87% of energy requirement is fulfilled by fossil fuels (30% coal, 24% gas, and 33% oil), 4% by nuclear fission and 7% by hydro and 2% by renewable sources [1]. According to the International Energy Agency (IEA) the proven reserves of coal are around 900 billion tonnes, which would sustain the current production rate until 2051 at a 5% growth per annum [2]. Current consensus of oil supply profile is that the peak of extraction will occur in 2020 at the rate of 93 billion barrels per day. Environmental concerns related to global warming and sustainability are expected to move the world's energy consumption away from fossil fuels.
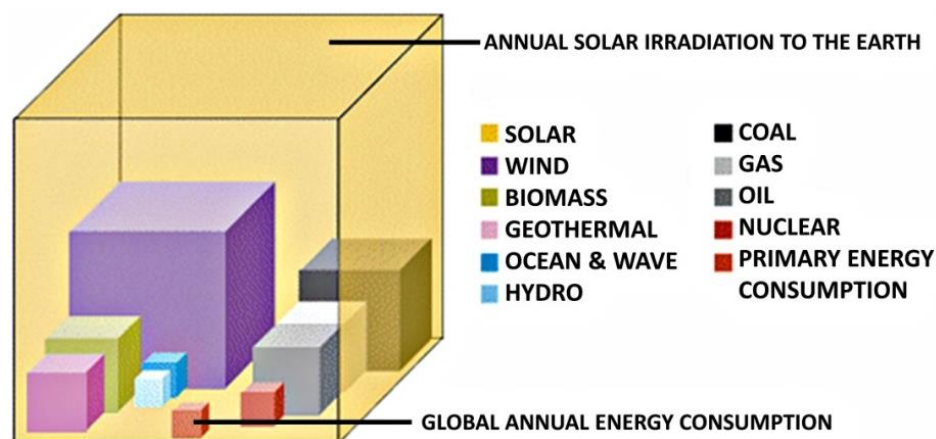
Figure 1.1: Outstanding solar potential compared to all other energy sources [3] Fossil fuels are expressed with regard to their total reserves, renewable energies to their yearly potential. Source: Greenpeace and European Photovoltaic Industry's Report Solar Generation 6

Assuming current consumption rate, present oil reserves would be completely depleted by the year 2050. Many countries have been taking efforts to develop a sustainable energy especially "green energy" that is friendly to the environment obtained from renewable resources, such that the provision of this form of energy serves the needs of the present without compromising the ability of future generations to meet their needs. Compared to nuclear and hydroelectric power, solar energy is safer, non- polluting, unconstrained by the geography (especially suitable for desert) and abundantly available.
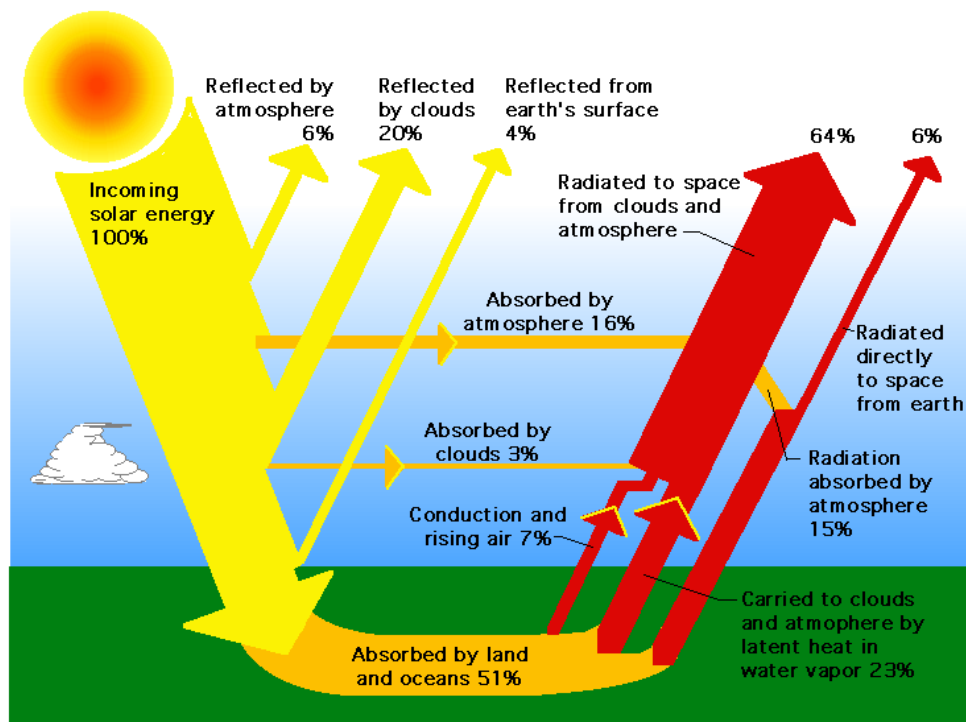
Figure 1.2: Solar energy loss mechanism in the atmosphere [4]

The sun's radiation reaching the earth is reduced by scattering and absorption in the atmosphere. Fig 1.2 shows the loss mechanism of the incoming solar energy reaching the earth's surface. Annually 51 % of solar energy available from the sunlight passes

Earth's surface. On a clear day, approximately one kilowatt of solar energy per square metre is incident on the Earth's surface and harnessing this energy for one hour would be sufficient to supply the world's energy needs for an entire year. That is, if a tiny fraction of the energy earth receives could be converted to useful energy, all our energy needs would suffice. If so, what is preventing us from tapping into the enormous amount of energy that strikes the earth every day? The development of high efficiency and cost-effective solar cells is a major challenge we face today but it is an important part of the solution.

1.2.   Commercial Solar cells: Silicon or GaAs?

Researchers from all over the world try to make huge progress in the solar cell technology (figure 1.3).
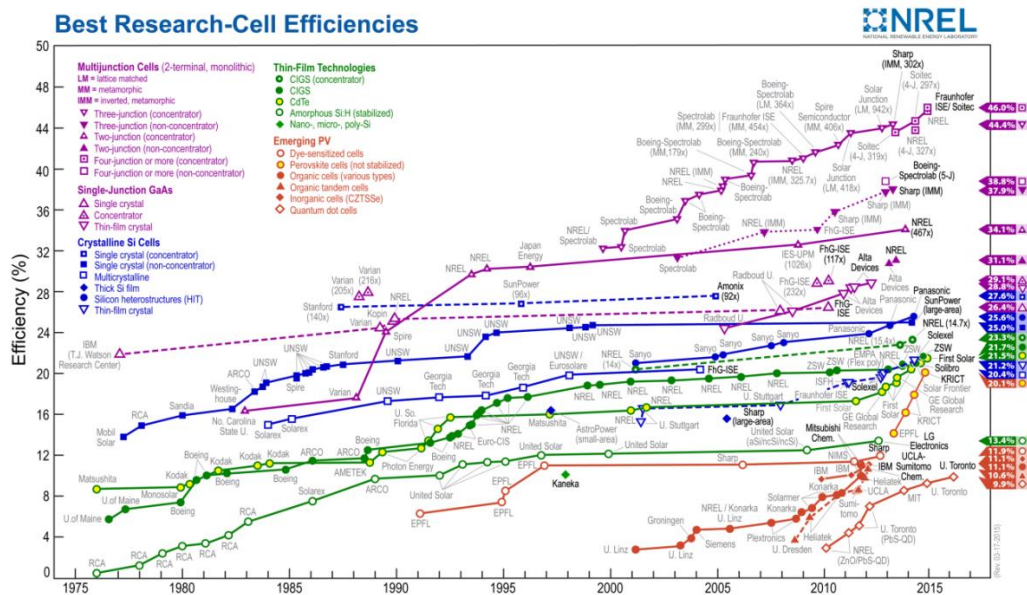

Figure 1.3: Conversion efficiencies of the best research solar cells worldwide from 1976 through 2015 for various photovoltaic technologies [5]

Commercial solar cells are mostly made in crystalline silicon because it is available abundantly on earth, cheap (including Si crystal wafer), and developed on technologies of purification, growth and fabrication. But, Silicon has lower absorption coefficient because of its indirect band gap. Therefore the solar cells must be much thicker to absorb sunlight efficiently resulting in higher production cost. This has led many companies focus towards the research of low cost second generation thin film solar cells. Crystalline solar panel cells are 0.15-0.2 mm thick, whereas thin film cells can be as thin as 0.001 mm making them weigh less and flexible.

The most common types of commercial thin film solar cells are hydrogenated amorphous silicon, cadmium telluride and copper indium gallium selenide (CIS or CIGS) [6].Flexibility, good performance in indirect sun light and resistance to high heat makes these thin film solar panels more attractive. However, the disadvantages of amorphous silicon based solar cells are low efficiency and high equipment cost. Though CdTe solar cells have medium efficiency the rigid glass substrate is its big disadvantage. CIGS solar cells have the challenge of achieving film uniformity on large substrates. These (a-Si-H, CaTe, CIGS) thin film solar cells efficiencies (20-30 %) drop with prolonged use as well. GaAs thin film solar cells have several advantages over silicon in terms of use in electronics such as high electron mobility and a direct band gap, which allows the material to absorb light efficiently. In addition, its larger direct band gap of 1.42 eV compared to 1.1 eV for silicon is better matched to the solar spectrum in a single junction cell leading to a higher efficiency. GaAs also holds the world record for the highest efficiency single junction solar cell at 28.3% [7].

1.3.   Efficiency limit of solar cells

In solar cells the absorption of photons, which results in the generation of the charge carriers and their subsequent separation take place in semiconductor materials. Hence the semiconductor layers are the most important parts of a solar cell. As the solar spectrum has a broad distribution of wavelengths from 250 to 2500 nm (see Fig. 1.6), all semiconductors having band gaps between 0.35eV and 3.5eV, can absorb above bandgap photons in solar cells. For smaller band gaps, most photons would be absorbed thereby increasing current density but a good portion of their energy would be wasted through thermalization. In addition, since the cell operates at a potential difference proportional to the band gap, each extracted carrier's potential energy will be small. For larger band gaps, a good portion of the incident photons would not be absorbed and current density would decrease. In both cases, efficiency drops off due to the current density being inversely proportional to the operating voltage.
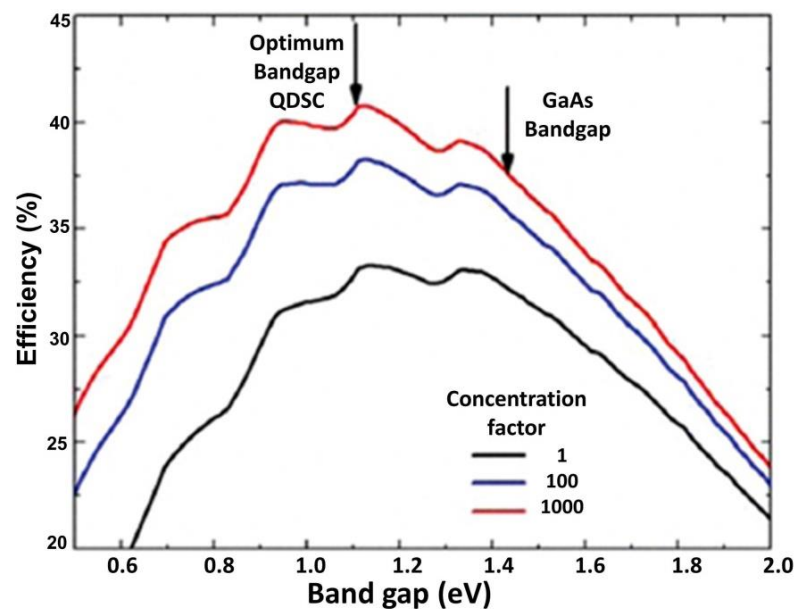

Figure 1.4: Solar efficiency limit with the function of concentration factor [8]

But there is an optimal bandgap for solar cells based on the detailed balance principle. The theoretical efficiency limit of 31 % for a single junction solar cell was obtained at bandgap between 0.95 and 1.6 eV [9] by Shockley and Queisser. The maximum efficiency limit as a function of the band gap (E_g) for concentrated and unconcentrated light is shown in figure 1.8. In a single junction solar cell, the maximum theoretical efficiency ranges from 33 to 41% over 1 to 1000 suns concentration (figure 1.4) but the optimal bandgap changes from 1.2 eV (1 Sun) to near 1 eV (1000 Suns). More specifically, as the concentration factor increases so does the limiting efficiency up to the maximum of 41%. Therefore the efficiency is highly dependent on the device's band gap and that photons with energy near the band gap are used most efficiency. Some semiconductors like Si (Silicon), GaAs (Gallium Arsenide), CdTe (Cadmium Telluride), CIGS (Copper Indium Gallium Selenide), a-Si:H (hydrogenated amorphous silicon) have their band gap within this optimum range and suitable for efficient solar cells .

Figure 1.5 shows that the main energy loss in solar cells is due to thermalization and lack of absorption that limits the efficiency. The work done per photon decreases as the photon's energy increases beyond the band gap with losses occurring from thermalization and goes to zero when the photon's energy is less than the band gap. These losses are realized in the conventional solar cell because our solar resource has a broad energy spectrum and poorly matches the band gap, as reflected in the limiting efficiency values. The single junction GaAs solar cells available today can only process visible sunlight. That means over half of the energy available from IR and the remainder in the UV is not being absorbed to produce electricity. Hence the solution to the problem is to introduce the light trapping structures (Example: Silver

nanoparticles) and engineering the density of states (Example: Quantum dots) in solar

cell structures.
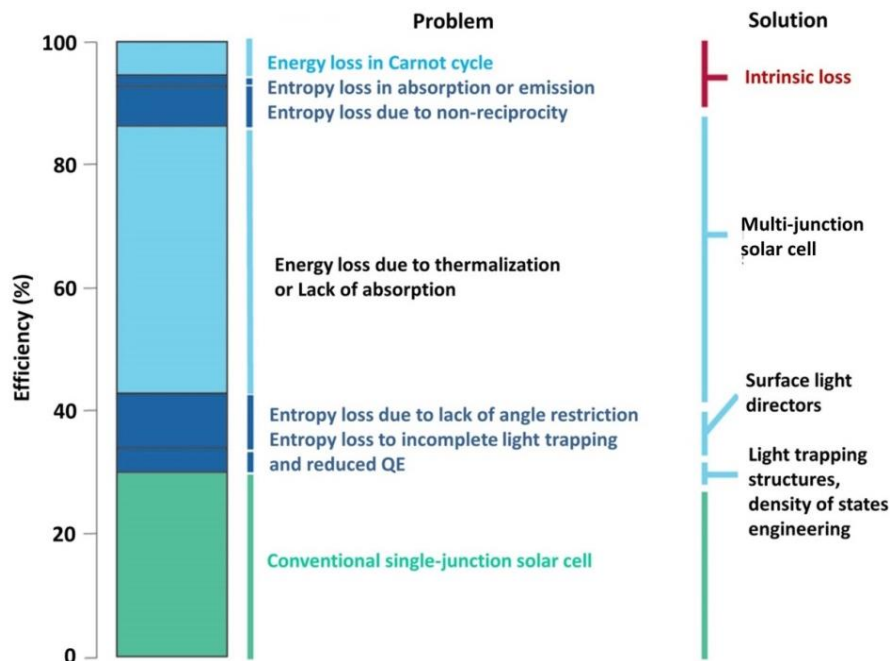
Figure 1.5: The maximum efficiency realized for a conventional single-junction solar cell is 28.3%
(indicated in green). Dark blue bars indicate entropy-related losses and light blue bars indicate energy-
related losses. The solutions to reducing the entropy and energy-loss problems are listed on the right
[10].

Nanoscale semiconductors like quantum dots (QDs) are novel nanostructures with

huge potential to become the basis of next generation solar cells, capable of producing

additional electricity by absorbing the Infrared and near infrared photons (fig 1.7).

1.4.   Quantum dots for solar cells (QDSC)

In single junction solar cells, the low energy photons that are smaller than the band

gap are not absorbed, but instead they are transmitted through the device. Hence, these

cells lack the long wavelength response and the conversion efficiency. The devices

embedded with quantum dots between the barrier materials can produce large short-

circuit currents due to the absorption of sub band gap photons through the intermediate band formation (fig 1.7). The barrier material can absorb wavelengths below 800 nm while the quantum dots can be used to absorb wavelengths up to 2 µm (figure 1.6).
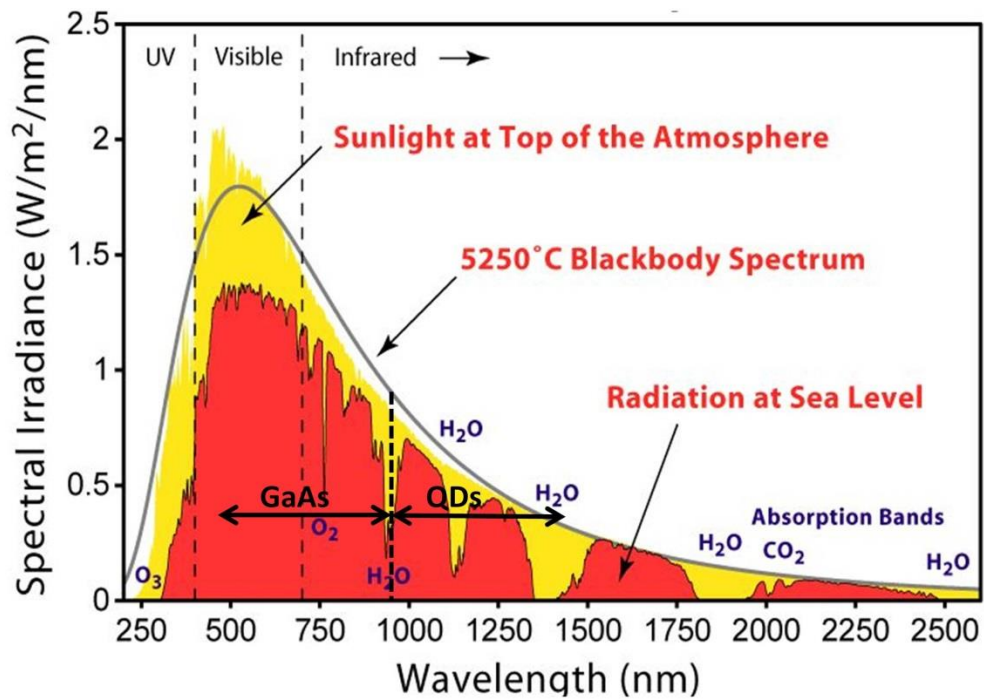
Figure 1.6: Solar spectrum showing the absorption wavelength range of GaAs and QDs

[Modified from11]

Quantum dots (QDs) continue to attract considerable interest because of their potential to significantly improve the performance of III–V based single-junction solar cells. The use of QDs allows one to reduce the effective bandgap and the ability to tune the band gap to spectral conditions under concentration as the electrical and optical properties can be controlled by the QD size, shape and composition. Although quantum dot solar cells have not yet reached the potential of silicon or GaAs solar cells, the theoretical efficiencies predict much higher results within the near future.
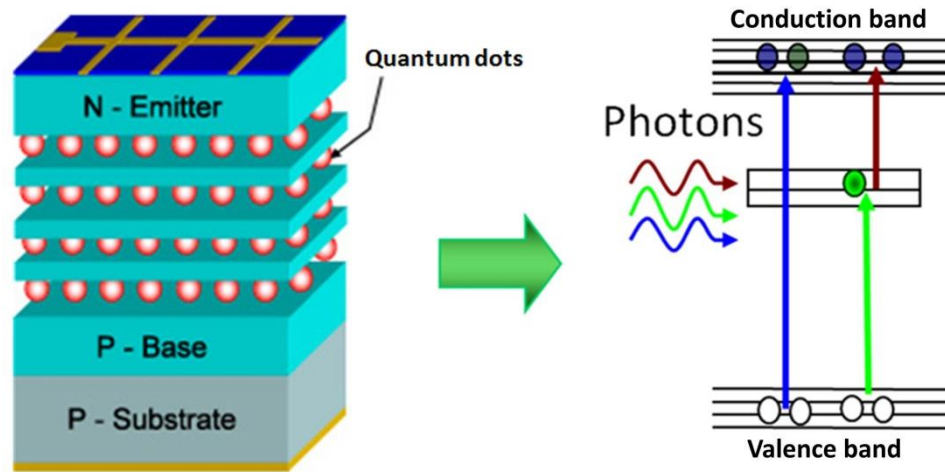
Figure 1.7: Schematic of operation principle of quantum dot solar cell [12]

The main reason for interest behind the QD solar cell is that it has been shown theoretically that the calculated efficiency can reach as high as 63% for Intermediate band solar cell (IBSC) [13]. If realised, this percentage will set a new record for solar cell efficiency. The coupling of discrete levels in close-stacked epitaxial QDs forms an intermediate band in the host semiconductor bandgap, enabling an absorption of sub-bandgap photons from the valence band (VB) to the intermediate band (IB), and from the intermediate band (IB) to the conduction band (CB) (figure 1.7). Since the Intermediate band is electrically isolated from valence band (VB) and conduction band (CB), their introduction increases short circuit current (I_{sc}) and keeps open circuit voltage (V_{oc}) unreduced.

1.5. Type II GaSb QD/QR solar cells

Many material systems like the common InAs/GaAs quantum dots show a type-I band alignment, meaning that both electrons and holes are confined within the nanostructure. Among the proposed quantum structures, type-I QD is one of the most popular choices for the Intermediate band solar cell (IBSC). Many researches focused

on multiple layer stacking and high quantum efficiency which have been published previously [14].As an alternative system, type-II GaSb/GaAs QD structure has been proposed and demonstrated [15].This structure has a staggered or type-II" band alignment with only one sort of charge carriers being confined exhibiting a strong confinement for holes but a repulsive potential for electrons. Figure 1 .8 shows a quantum dot and its band structure in which the hole is trapped by the potential of the dot. The electron is able to move around the dot, but is attracted to the hole by the Coulomb force.
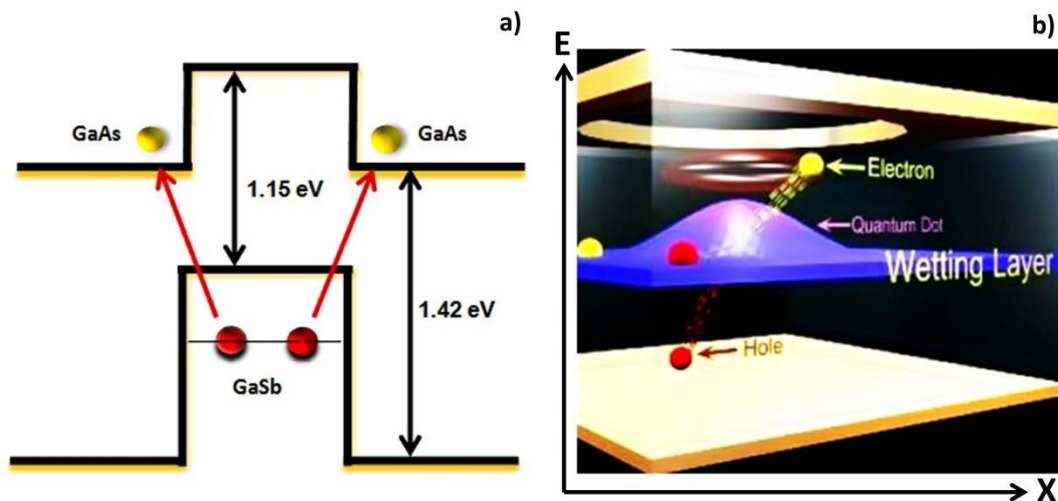
Figure 1.8: a) Type II band alignment of GaSb quantum dot on GaAs structure b) 3D view of type II QDs in which the electron is able to move around the dot and the hole is trapped by the potential of the dot. X indicates a spatial axis, whilst E corresponds to energy [16]

Because of this electron–hole spatial separation, type-II QDs show unique optical properties different from those of type-I QDs, such as dot-shape-dependent oscillator strength and long radiative lifetime [17] which improves carrier extraction .Compared with type I InAs QDs, type-II GaSb/GaAs QD structure has an optimal bandgap of 1.15 eV which produces larger red-shift of the photo-response and captures more of the infrared solar spectrum [18]. However, the introduction of GaSb QDs in GaAs

solar cells degrades the open circuit voltage (V_{oc}) and hence lowers the overall efficiency of the device. Under a white light illumination (1 sun intensity), the GaSb QR solar cells display an enhanced J_{sc} compared with the GaAs control cell (~6%) but the open-circuit voltage (V_{oc}) is reduced. The origin of the V_{oc} reduction may be because of the increased recombination within the GaSb QRs and thermal coupling between the valence bands [19], or the crystalline quality of the surrounding GaAs.

The analysis of the photoresponse under the white light illumination has shown that some photogenerated minority holes from the base region can be re-captured by the QRs, which reduces the J_{sc} and the V_{oc}. In this thesis, the QRs are directly probed by using an infrared laser (1064 nm) where the photon energy is conveniently chosen below the bandgap of the GaAs matrix. This enables us to investigate the carrier dynamics and extraction mechanisms occurring in the GaSb QRs under a high light concentration. The dependence of the photocurrent on the laser intensity, the bias and the temperature is also discussed. For detailed understanding of thermal influence on device performance as well as carrier dynamics, temperature dependant photoluminescence spectroscopy is performed. Experiments have shown that QDs embedded in the depletion region could generate additional photocurrent. But, electron-hole recombination in QDs results in additional dark current which reduces the open circuit voltage and keeps the conversion efficiency of QD solar cells below the Shockley-Queisser limit. To address this problem, the approach of placing QDs in the n or p region of the solar cell and the effects of delta doping of quantum dots has been investigated in this thesis. GaSb QRs have exhibited an enhanced infrared photoresponse extending beyond 1 μm and an increase in the short-circuit current (J_{sc}). This improvement is achieved by sub-bandgap photon absorption below the

absorption edge of the host material. The extended tail energy states (also known as Urbach tail) lead to an effective reduction of the bandgap, to an increase of the photo-generated current and to a reduction of the open-circuit voltage [138]. The effect of below-bandgap absorption of extended Urbach tail in a QD device using room temperature external quantum efficiency measurements is evaluated in this thesis. In summary, this thesis reports the study of single junction solar cells containing GaSb multi-layered (5 and 10 layers) QDs in GaAs, which is one of the most promising and novel type II solar cell structures. GaSb QDs/QRs have been investigated to determine how QDs impact the operation of GaAs-based solar cells, and how they can be implemented to achieve higher conversion efficiency.

Chapter 2

Background theory

2.1. Solar cell fundamentals

In solar cells, the energy in the sunlight is transformed directly to electric energy. Photons excite electrons from states with low energy to states higher in energy. Using proper devices, it is possible to extract some of the exited electrons and let them go through an external electric circuit before they end up in the low energy states of the solar cell, where they started. This is called photovoltaic effect.
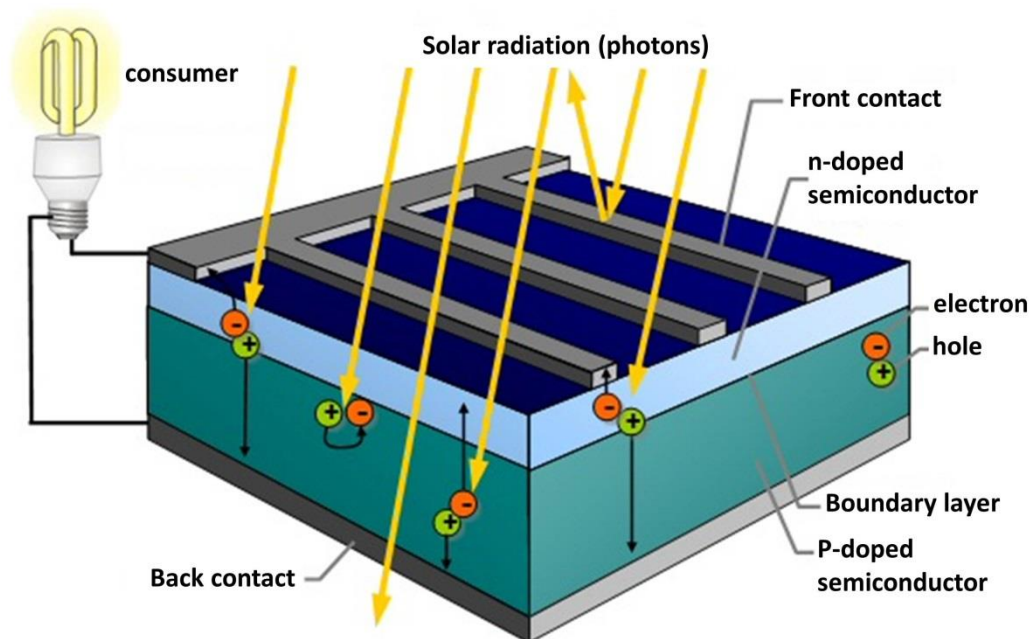

Figure 2.1: Solar cell structure [20]

The most common implementation of the photovoltaic concept is the semiconductor pn-junction solar cell. The generation of current in a solar cell, known as the "light

generated current", involves two key processes. The first process is the absorption of incident photons to create electron-hole pairs. Electron-hole pairs will be generated in the solar cell provided that the incident photon has an energy greater than that of the band gap. A second process is the collection of these carriers and prevention of recombination by using a p-n junction to spatially separate the electron and the hole. The carriers are separated by the action of the electric field existing at the p-n junction. If the light-generated minority carrier reaches the p-n junction, it is swept across the junction by the electric field at the junction, where it is now a majority carrier. If the emitter and base of the solar cell are connected together (i.e., if the solar cell is short-circuited), the light-generated carriers flow through the external circuit. In addition to semiconductor layers, solar cells consist of a top and bottom metallic grid or an electrical contact that collects the separated charge carriers and connects the cell to a load (consumer) as shown in figure 2.1. Usually, a thin layer that serves as an antireflective coating covers the topside of the cell in order to decrease the reflection of light from the cell. In case of thin-film solar cells, layers that constitute the cell are deposited on a substrate material.

2.1.1.   P-N junction

When a semiconductor is doped with donor impurities, the number of electrons in the conduction band is increased and it is called n-type material. Similarly when the semiconductor is doped with acceptor impurities, it is called p-type material. The interface formed between p type material and n type material when they are joined together is called p-n junction. The electrons will tend to diffuse across the junction into the p-type material as the electron concentration in the n-type material is much higher than in the p-type material, (fig 2.2 b). Similarly, the holes will tend to diffuse from the p-type to the n-type material.
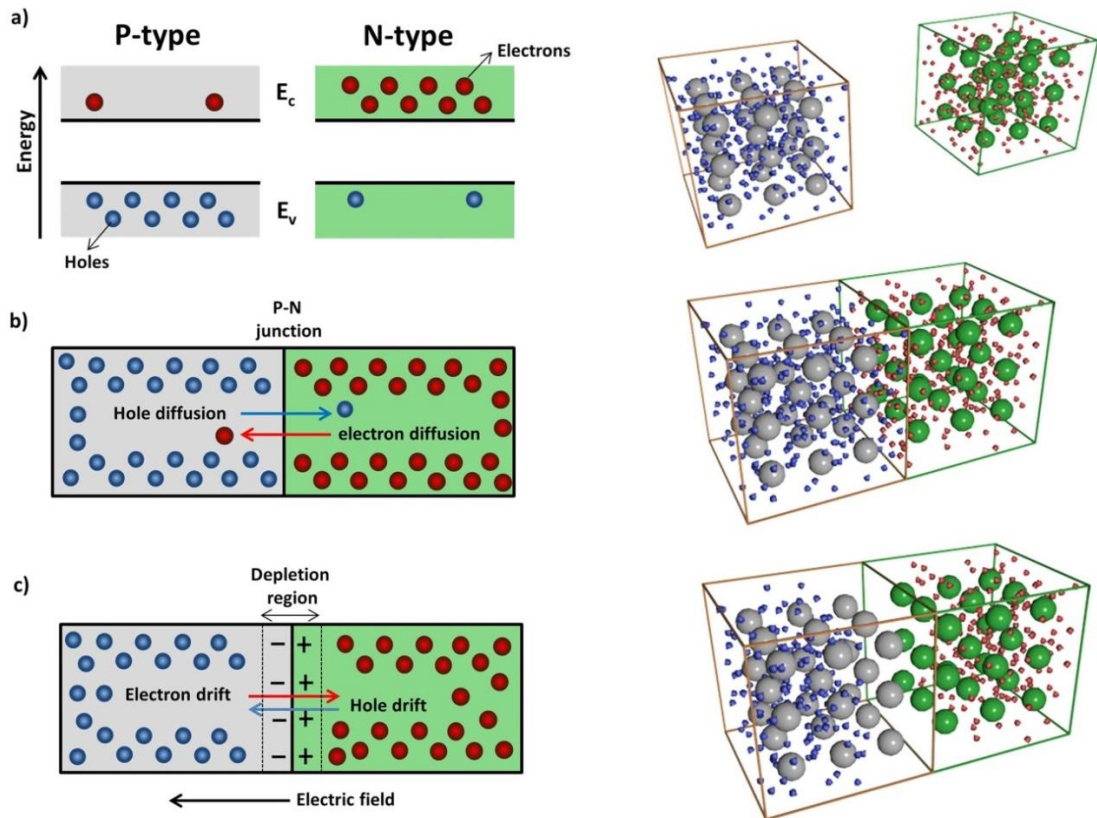
Figure 2.2: a) P type semiconductor material having conduction predominantly by holes in valence band and N type semiconductor material having conduction predominantly by electrons in conduction band b) Formation of ideal P-N junction when the two materials are brought in contact with each other c) Formation of depletion region. (Virtual reality semiconductor pictures are shown on the right side of the corresponding diagrams [21] (E_C refers to conduction band edge and E_V refers to valence band edge)

The charge density of the p-type material along the junction is filled with negatively charged acceptor ions (N_A), and the charge density of the n-type material along the junction is filled with positively charged donor ions (N_D). The charge transfer of electrons and holes across the p-n junction is known as diffusion. The width of P and N semiconductor layers depends on the amount of doping on each side with acceptor density N_A, and donor density N_D, respectively. The charge due to the ionized donors and acceptors causes an electric field, which in turn causes a drift of carriers in the opposite direction and creates a potential difference between the two types of material. This opposing flow of charge under a potential difference is called drift (fig 2.2 c). A

region near the junction will have no charge carriers present, as they have recombined with their counterparts from the other material type. This area is called depletion region, or space-charge region [22].If D is depletion region thickness, it penetrates into the semiconductor by a distance of D_p on p side, and a distance of D_n on n side. The relation between the charge density and the depletion width is $D_p.N_A = D_n.N_D$ in order to maintain the equilibrium. The change in depletion width can be characterised through the measurement of the junction capacitance (C) as a function of the applied voltage (V).

The depletion width is given by [23]

$$D = \frac{\varepsilon_o \varepsilon_r A}{C(V)}$$

(2.1)

where ε_o and ε_r are the permittivity of a free space and relative permittivity of the semiconductor, A is the junction area and D is the width of the space charge region. For an abrupt junction, where one side of the junction is much more heavily doped than the other, the doping concentration is given by [23]

$$N(W) = \frac{2}{q\varepsilon_o \varepsilon_r A^2} \left(\frac{dV_t}{d\left[\frac{1}{C^2} \right]} \right)$$

(2.2)

where V_t is the total bias across the junction including the built in voltage(V_{bi}). The built in voltage can be determined from a plot of $1/C^2$ versus the applied voltage, which should be a straight line for an abrupt single sided junction with constant doping concentration. The built-in potential that exists at equilibrium across the junction opposes both the flow of holes and electrons across the junction. The built-in potential is called the potential barrier.
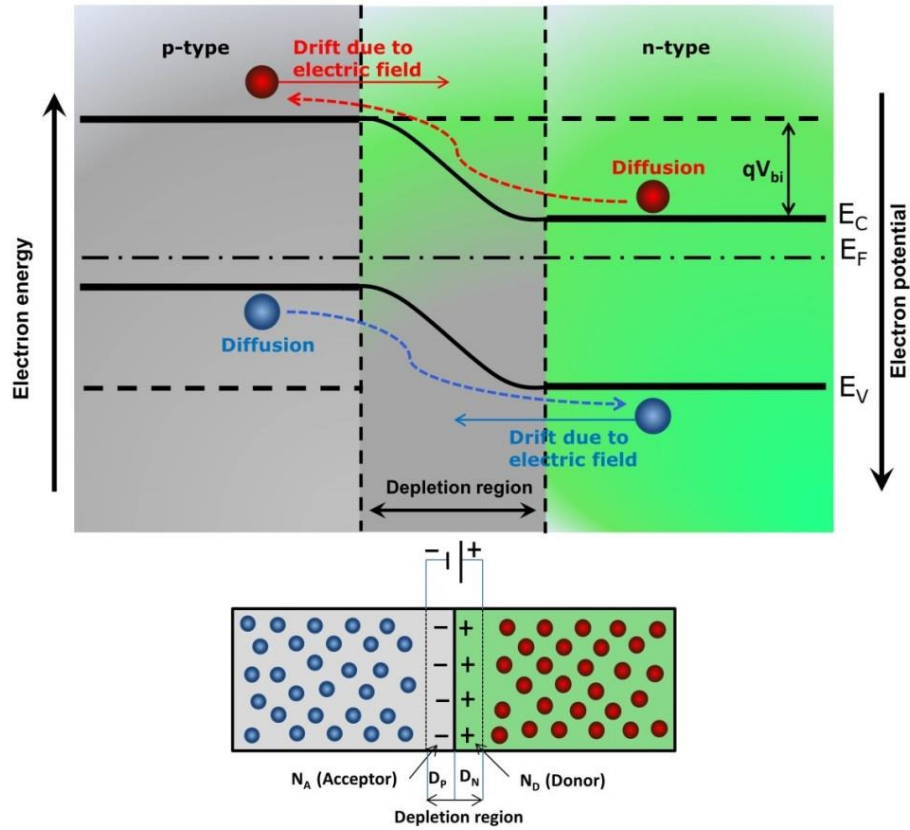
Figure 2.3: Energy band diagram of p-n junction and the formation of potential difference across the junction at Zero bias condition.

The built-in potential difference across the junction with an open-circuit voltage (zero bias) or potential barrier is given by [24] :

$$V_{bi} = V_T \ln\left[\frac{N_D N_A}{n_i^2}\right] \qquad (2.3)$$

Where V_T the thermal voltage of 26 mV at room temperature, N_D and N_A are the impurity concentrations and n_i is the intrinsic concentration. For free charge carriers to cross the depletion region junction, they require some additional energy to overcome the potential barrier. A suitable positive voltage or forward bias applied between the two ends of the p-n junction can supply the free electrons and holes with the additional energy they require to cross the junction as the width of the depletion

layer around the PN junction is decreased. If this external voltage becomes greater than the value of the potential barrier, the potential barriers opposition will be overcome and current will start to flow. The top of the filled electron energy levels at low temperatures is given by Fermi level (E_F). The position of fermi level in relation to the conduction band is a crucial factor in determining electrical properties of a p-n junction, essential for all semiconductor technologies.

2.1.2. The PIN diode structure

In this thesis, the GaSb/GaAs solar cells are pin semiconductor structures in which an intrinsic region (i-region) separates the heavily doped p-type and n-type regions. Figure 2.4 shows a schematic representation for the pin structure.
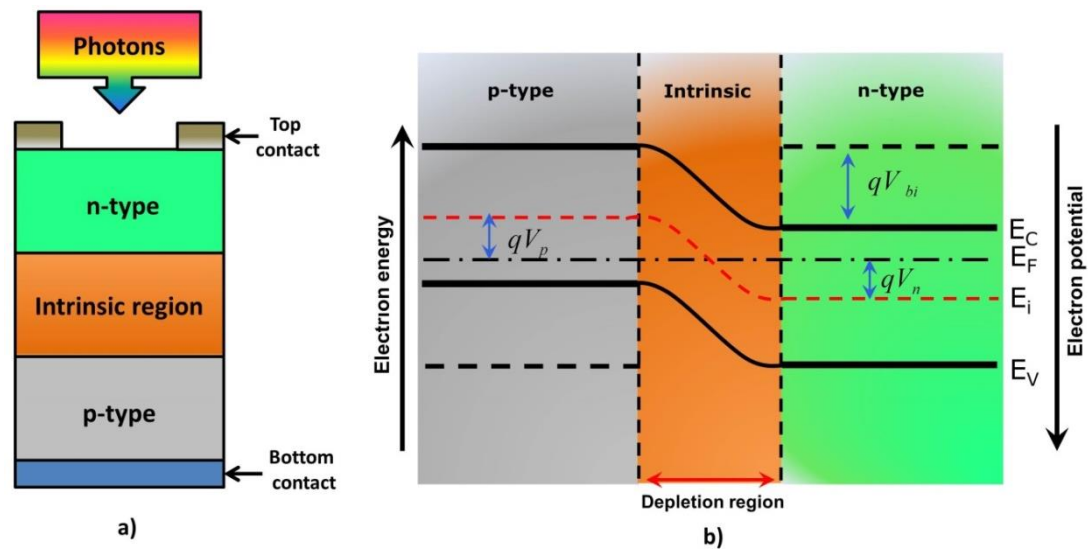

Figure 2.4: a) schematic representation of pin solar cell structure b) Energy band diagram of pin structure where qV_n is the barrier for the electrons to move from n-side to P-side, qV_p is the barrier for the holes to move from P-side to n-side and E_i refers to the intrinsic Fermi level [25].

The photogenerated excess minority carries in the n and p-type regions diffuse toward the i-region and get swept across to the metal contacts. In this design the electric field created between the n-type and p-type regions stretch across the intrinsic layer to

increase the depletion region thickness. The carriers are transported more efficiently by drift as opposed to diffusion. This process is essential for the QD layers when placed in the intrinsic region.

2.2.   The solar spectrum

In a commercial solar cell, more than 50% losses are associated with the spectral mismatch i.e. the inability of the semiconductor material bandgap to absorb energy of the full solar spectrum. This states the importance of solar simulation systems to match the spectral distribution of solar radiation, incident on the earth's surface. When sunlight reaches the earth's surface, its intensity is dependent on the path taken through the atmosphere.
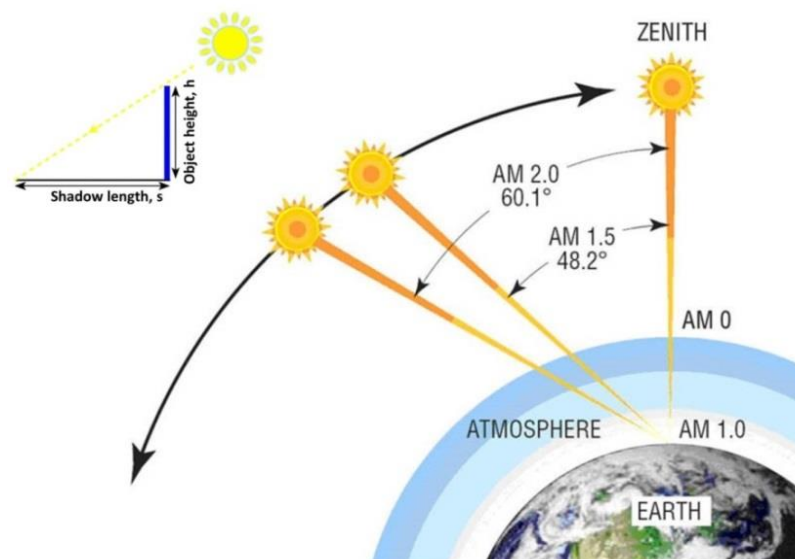

Figure 2.5: Illustration of the global average of sunlight travelling through 1.5 Air Mass or 1.5 atmosphere thickness at an incidence angle of 48.2º. [26] The inset shows the relation of Air mass to the length of the shadow and the object height h.

The solar spectrum and irradiance is established by the air mass. Air mass (AM) refers to the amount of air a beam of sunlight must go through before reaching the solar converter. The optical air mass (AM) is the ratio of an actual path length of sunlight to

the minimum path length (when the sun is directly overhead). When the sun is at an angle θ from the horizon and s is the length of a shadow cast by a vertical object with height h, the air mass is given by [27]

$$Air.mass = \frac{1}{\cos\theta} = \sqrt{1 + \left(\frac{s}{h}\right)^2}$$

(2.4)

The AM0 radiation can be practically used from sunlight capture outside the atmosphere. We never receive AM0 radiation once the sunlight has reached earth's surface.
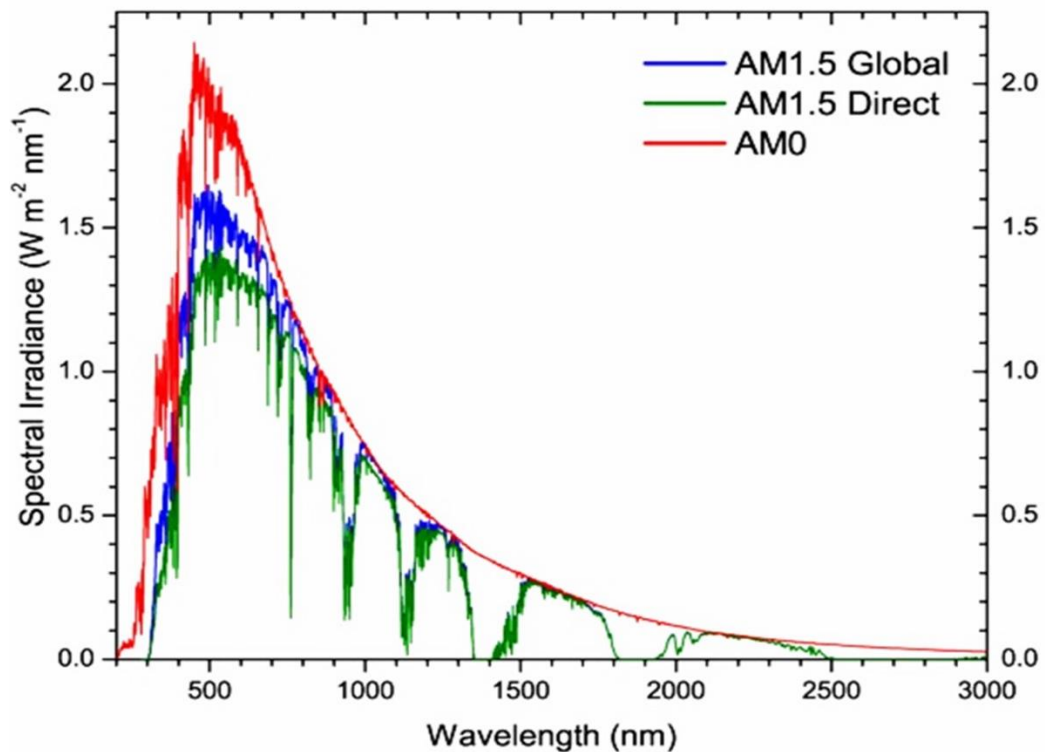
Figure 2.6: Standard Solar Spectra for space (AM0) and terrestrial use (AM1.5) [28].

We receive the AM1 radiation when sun is directly overhead, whereas the AM1.5 radiation is received when the sun is at an angle of 41.8° above the horizon (or 48.2° from directly above). AM1.5 radiation corresponds to a mean irradiance of about 900 W/m^2, but has been standardized to 1000 W/m^2 or 1 kW/m^2. AM1.5 characterises the

ideal spectrum of sunlight received at temperate latitudes. Most of the solar cell research is performed using the AM1.5 solar simulation systems. Figure 2.6 shows the solar irradiance spectrum. The notches in the spectrum are attributed to the absorption bands of different atmospheric gases such as H_2O, CO_2, O_3, and O_2. Absorption by ozone is essentially complete below a wavelength of 300 nm. The relatively large attenuation below 800 nm is due to scattering of molecules and particulates. These scattering processes become weaker at longer wavelengths. There are two standards used for terrestrial purpose. The AM1.5 Global spectrum is designed for flat plate modules with an integrated power of 1000 W/m^2 (100 mW/cm^2).

The AM1.5 direct (+circumsolar) spectrum is defined for solar concentrator work. It includes the direct beam from the sun plus the circumsolar component in a disk, 2.5 degrees around the sun with an integrated power density of 900 W/m^2. In this work, AM 1.5 Global spectrum is used.

2.3.   Generation and recombination in solar cells

The range of the solar spectrum that can be absorbed by a semiconductor is limited by its band gap energy (E_g). Figure 2.7 outline the generation and recombination mechanisms in a semiconductor solar cell. (1) The solar cell is transparent to the photons with an energy $E < E_g$ which will not have enough energy to excite an electron across the band-gap and the energy is wasted. (2) A photon with energy $E = E_g$ will have the right amount of energy to excite an electron across the bandgap and into the conduction band creating an electron-hole pair. (3) A photon with $E > E_g$ will be excited higher into the conduction band and will relax back quickly to the band-gap edge through phonon interactions. In this case, the energy is lost in the form of heat. (4) Radiative recombination occurs as an electron in the conduction band drops to the

valence band and recombines with a hole, thereby losing energy by emitting a photon.

(5) Shockley-Read-Hall (SRH) recombination occurs when an electron recombines

with a hole via defect and impurity states in the semiconductor [29].
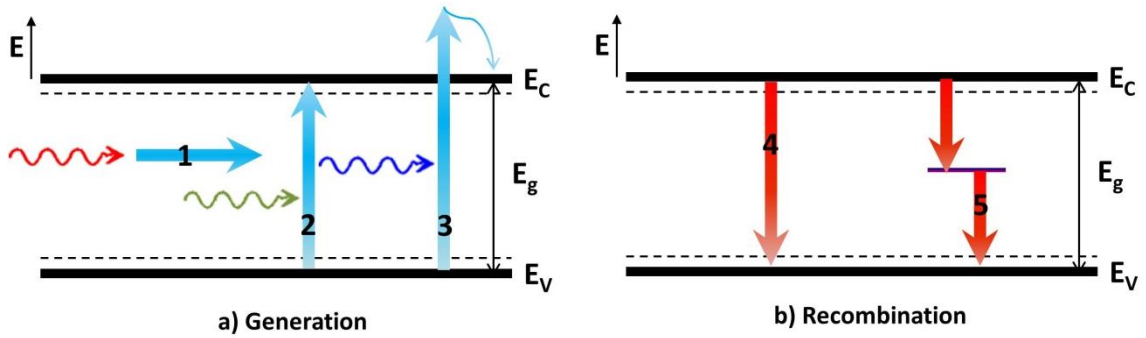
Figure 2.7: a) Radiative generation in a semiconductor solar cell. (1) Transparent for incoming photon

with E < Eg.(2) Incoming photon with E = Eg will have enough energy to excite an electron across the

band-gap.(3) Incoming photon with energy E > Eg will excite an electron high into the conduction band

and quickly relax to the band gap edge b)Radiative and non-radiative recombination in a semiconductor

solar cell.(4) Electron drops to across the band-gap and emits a photon. (5) SRH recombination,

electrons and holes recombine via defects energy is lost in the form of heat.

2.4.   Solar cell parameters

2.4.1.   Current voltage characteristics

The ideal diode equation gives an expression for the current through a diode as a

function of voltage:

$$I = I_0 \left(e^{\frac{qV}{kT}} - 1 \right)$$

(2.5)

where I is the net current flowing through the diode, I_0 is the dark saturation current-

the diode leakage current density in the absence of light, V is the applied voltage

across the terminals of the diode, q is the absolute value of electron charge, k is the

Boltzmann's constant and T is the absolute temperature (K). I_0 is a measure of the recombination in a device. A diode with a larger recombination will have a larger I_0 [30]. For non- ideal diodes (actual diodes), the expression becomes:

$$I = I_0\left(e^{\frac{qV}{nkT}} - 1 \right)$$

(2.6)

Where, n is the ideality factor, a number between 1 and 2 which typically increases as the current decreases.

The IV curve of a solar cell is the superposition of the IV curve of the solar cell diode in the dark with the light-generated current [31]. The light has the effect of shifting the IV curve down into the fourth quadrant where power can be extracted from the diode. Illuminating a cell adds to the normal "dark" currents in the diode so that the diode law becomes:

$$I = I_0\left(e^{\frac{qV}{nkT}} - 1 \right) - I_L$$

(2.7)

where I_L id the light generated current.

The equation for the IV curve in the first quadrant is:

$$I = I_L - I_0\left(e^{\frac{qV}{nkT}} - 1 \right)$$

(2.8)

The -1 term in the above equation can usually be neglected. The exponential term is usually >> 1 except for voltages below 100 mV. Further, at low voltages the light generated current I_L dominates the I_0 term so the -1 term is not needed under illumination.

$$I = I_L - I_0 \left(e^{\frac{qV}{nkT}} \right)$$

(2.9)

Hence, in a solar cell, total current I is equal to the difference between the current I_L generated by the photoelectric effect and the diode current I_D, according to the equation:

$$I = I_L - I_D = I_L - I_0 \left(e^{\frac{qV}{nkT}} \right)$$

(2.10)
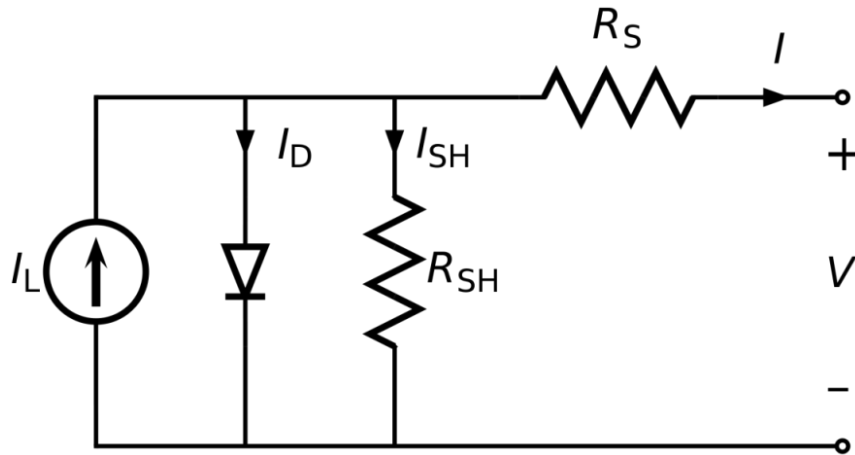
Figure 2.8: Equivalent circuit of a solar cell

To understand the electronic behaviour of a solar cell, it is useful to create a model which is electrically equivalent, and is based on discrete electrical components whose behaviour is well known. An ideal solar cell may be modelled by a current source in parallel with a diode; in practice no solar cell is ideal, so a shunt resistance (R_{SH}) and a series resistance (R_S) component are added to the model.[32] The resulting equivalent circuit of a solar cell is shown in figure 2.8. Hence the current produced by the solar cell is equal to that produced by the current source, minus that which flows through the diode, minus that which flows through the shunt resistor [33][34]. The equation 6 becomes,

$$I = I_L - I_D - I_{SH} = I_L - I_0 \left(e^{\frac{qV}{nkT}} \right) - I_{SH} \tag{2.11}$$

where I_{SH} is the shunt current. Hence the above expression can be rewritten including R_{SH} and R_S and the characteristic equation for the equivalent circuit of a solar cell is given as:

$$I = I_L - I_0 \left(\exp^{\frac{q(V+IR_s)}{nkT}} - 1 \right) - \frac{V + IR_s}{R_{SH}} \tag{2.12}$$

A typical idealised current-voltage (I-V) curve for a p-n junction solar cell in the dark and light is shown in figure 2.9a. The dark current curve shows only the recombination effect in a solar cell as no radiation is incident on the cell to produce generation effect. The light current curve has the same shape as the dark current curve but offset by a factor of J_{sc}. The short circuit current (J_{sc}) is the current when the applied bias is zero. In other words, it is a photogenerated current resulting from illumination of the cell. The open-circuit voltage (V_{oc}) is the maximum voltage measured from a solar cell, which occurs at zero current. V_{oc} is defined as the voltage at which the photogenerated current matches and cancels out the recombination current. An equation for Voc is found by setting the net current equal to zero in the solar cell equation (6) to give:

$$V_{oc} = \frac{nkT}{q} \ln \left(\frac{I_L}{I_0} + 1 \right) \tag{2.13}$$

As FF is a measure of the "squareness" of the IV curve, a solar cell with a higher voltage has a larger possible FF since the "rounded" portion of the IV curve takes up less area (figure 2.9b).
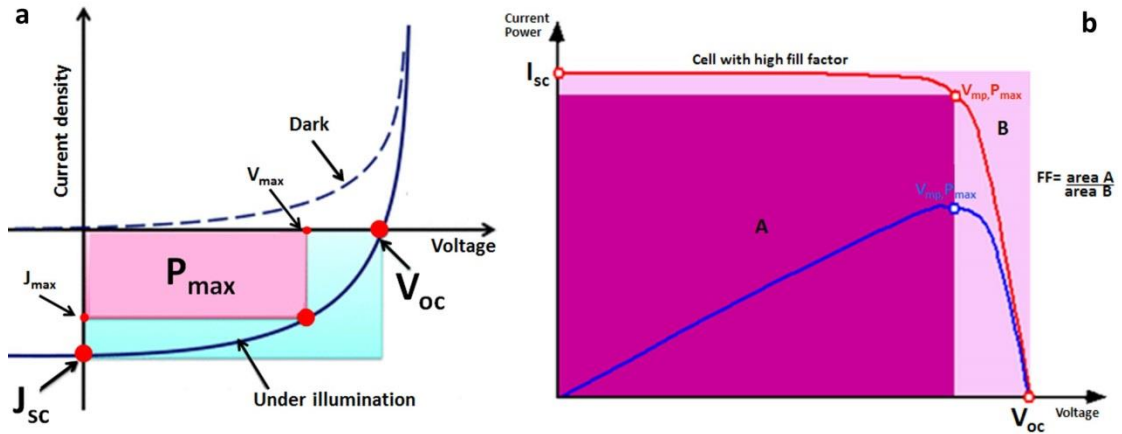
Figure 2.9: a) Idealised I-V curves for a solar cell in the dark and in the light indicating J_{sc}, V_{oc}, the voltage and current for maximum power V_{max} and J_{max} and the associated rectangle of maximum power b) Graph of cell output current (red line) and power (blue line) as function of voltage for cell with high fill factor [35]

The fill factor (FF), is a parameter which, in conjunction with V_{oc} and I_{sc}, determines the maximum power that can be obtained from a solar cell. The fill factor is defined by the following equation:

$$FF = \frac{V_{max} J_{max}}{J_{sc} V_{oc}} \tag{2.14}$$

The efficiency is the most commonly used parameter to compare the performance of one solar cell to another. Efficiency is defined as the ratio of energy output from the solar cell to input energy from the sun. In addition to reflecting the performance of the solar cell itself, the efficiency depends on the spectrum and intensity of the incident sunlight and the temperature of the solar cell. The efficiency of a solar cell (η) is determined as the fraction of incident power converted to electricity and is defined as:

$$P_{max} = V_{oc} J_{sc} FF$$

$$\eta = \frac{V_{oc} J_{sc} FF}{P_{in}}$$

(2.15)
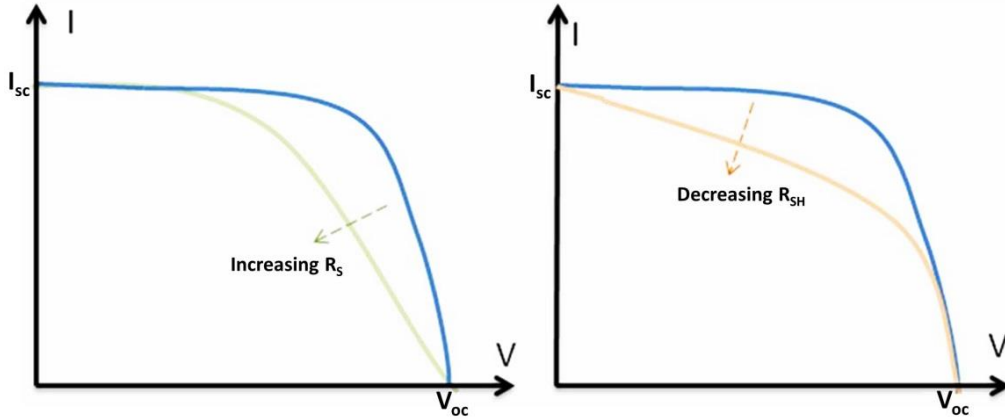
**Figure 2.10:** Effect of Diverging R_S & R_{SH} from ideal curve [36]

The input power P_{in} for efficiency calculations is 1 kW/m2 or 100 mW/cm^2. For an ideal cell, R_{SH} would be infinite and would not provide an alternate path for current to flow, while RS would be zero, resulting in no further voltage drop before the load. Decreasing R_{SH} and increasing R_S will decrease the fill factor (FF) and P_{max} as shown in the figure 2.10. If R_{SH} is decreased extremely, V_{oc} will drop, while increasing R_S excessively cause I_{SC} to drop instead.

2.4.2. Quantum efficiency

The quantum efficiency (QE) is the ratio of the number of carriers collected by the solar cell to the number of absorbed photons of a given energy incident on the solar cell. The amount of current that the cell will produce when exposed to sunlight can be determined by integrating the quantum efficiency over the whole solar spectrum. The External Quantum Efficiency (EQE) is the ratio of the number of charge carriers collected by the solar cell to the number of photons incident on the solar cell.

$$EQE = \frac{I/q}{P_{ph}/E_{ph}} = \frac{electrical\ power\ out}{optical\ power\ in} \qquad (2.16)$$

where I, q, P_{ph} and E_{ph} are current, charge of one electron, total power of photons and energy of one photon. Internal quantum efficiency refers to the efficiency with which photons that are not reflected or transmitted out of the cell can generate collectable carriers.
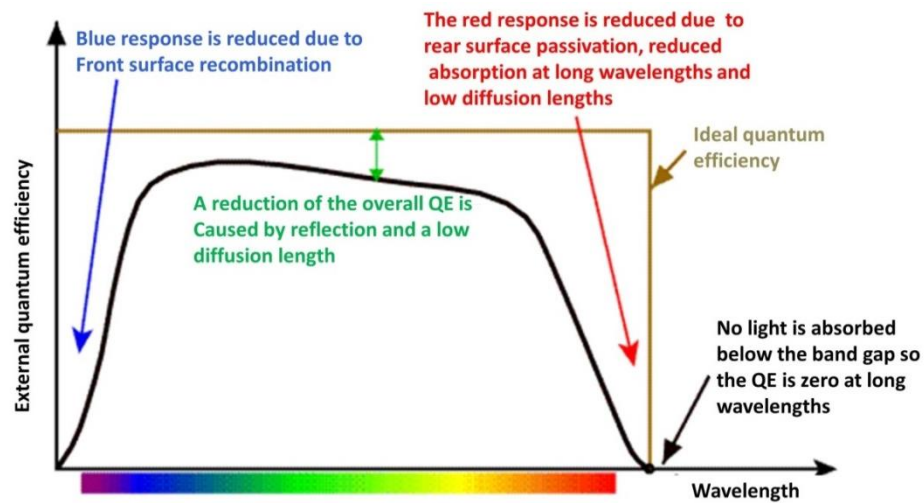
Figure 2.11: Quantum efficiency of the GaAs solar cell [37]

By measuring the reflection and transmission of a device, the external quantum efficiency curve can be corrected to obtain the internal quantum efficiency curve.

External quantum efficiency is the more commonly published result, and can be affected by factors 'external' to the solar cell, such as reflections and absorption. Internal quantum efficiency considers only the collection of those photons which are incident on the junction (rather than the device). Since internal quantum efficiency is not reduced by reflection or absorption, it always exceeds external quantum efficiency, and is often close to unity over a significant spectral range. A low IQE indicates that the active layer of the solar cell is unable to make good use of the photons. The use of nanostructured materials like GaSb quantum dots allow one to

tune the band gap of semiconductor heterostructures thereby improving the absorption properties of the device. It leads to a better match to the solar spectrum and subsequently increased photocurrent through the solar cell. The external quantum efficiency curve ideally has a square shape as shown in the figure 2.11. But the quantum efficiency for most solar cells is reduced due to recombination effect. Since the high energy (blue light) is absorbed very close to the surface, front surface passivation affects carriers generated near the surface thereby affecting the "blue" portion of the quantum efficiency. The absorbed green light in the bulk of a solar cell has a low diffusion length which will affect the collection probability from the solar cell bulk and thereby reduce the quantum efficiency in the green portion of the spectrum[38].The quantum efficiency of the GaAs solar cell is restricted to long wavelengths (~900 nm) photoresponse because no light is absorbed below the band gap.

2.5. Quantum dot solar cells

Figure 2.12 shows the generic structure of a quantum dot solar cell which shows that quantum dots are introduced into the intrinsic layer of the solar cell structure. At the top of the cell there are front contacts and an anti-reflective coating minimizing the reflection losses. A GaAs-cap layer is then placed as a barrier against oxidation since the following AlGaAs window layer oxides easily [39].This high band gap window layer reduces the front surface recombination. Beneath the window layer there is a heavily doped p+ layer which further reduces the front surface recombination. The p- and n-layers are then placed with an intrinsic layer sandwiched in between. A heavily doped n+-layer is placed beneath the n-layer to reduce the back surface recombination [40]. At the bottom of the cell there is a substrate where the upper layers are deposited

on and where the back contact is placed [39]. As discussed in the previous chapter, by introducing several layers of Quantum Dots into the active region of a solar cell, the spectral response of the cell can be extended so that more of the sun's radiation is absorbed and converted into electricity.
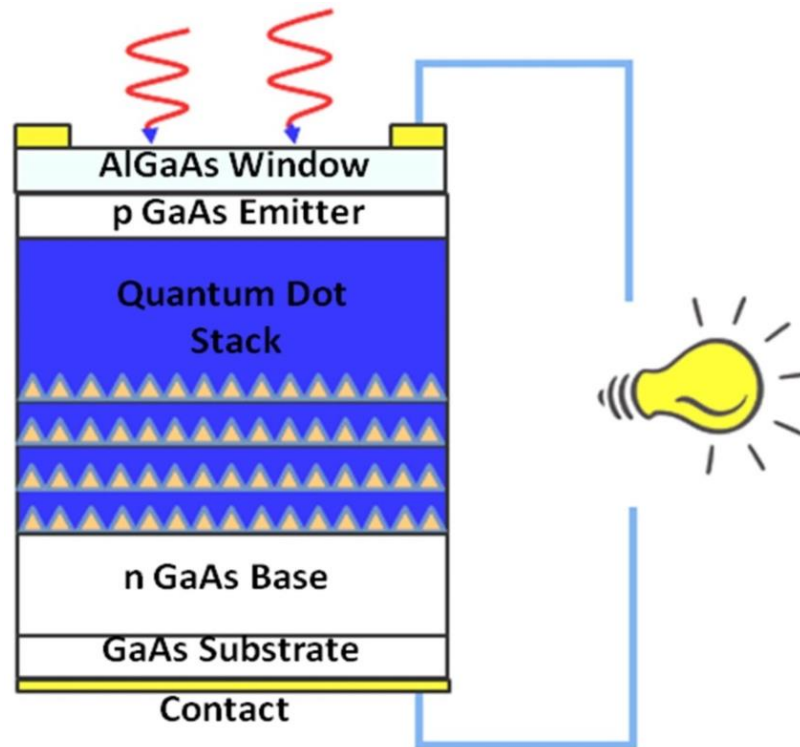

Figure 2.12: Structure of quantum dot solar cell

The use of QDs helps to reduce the effective band gap and the ability to tune the band gap to spectral conditions under concentration as the electrical and optical properties can be controlled by the QD size, shape and composition. The larger the size, the longer the wavelength of light absorbed. There is an optimum bandgap that corresponds to the highest possible solar electric energy conversion. GaAs based solar cells containing GaSb quantum dots (QD) have an optimal bandgap of 1.15 eV and could significantly extend the spectral response beyond 0.9 µm towards 1.4 µm.

2.6.   Band structure of GaSb/GaAs quantum dots

GaSb/GaAs structure represents a type-II alignment, exhibiting a strong confinement for holes but a repulsive potential for electrons, as shown schematically in figure 2.13. Just when a hole is confined within the QD but no corresponding electron is present due to the energetically unfavourable GaSb CB offset, the system gets charged, leading to a local band bending. This combination of the staggered band alignment, a strong hole confinement, and the low electron-hole recombination probability leads to two important consequences for the physics and applications of GaSb/GaAs nanostructures: Firstly, extraordinary long exciton lifetimes (~23 ns) can be achieved [41] [42]. Secondly, the confinement energy of holes in the QD and electrons in the CB of the surrounding matrix is considerably low. This helps to improve the carrier extraction in solar cells.
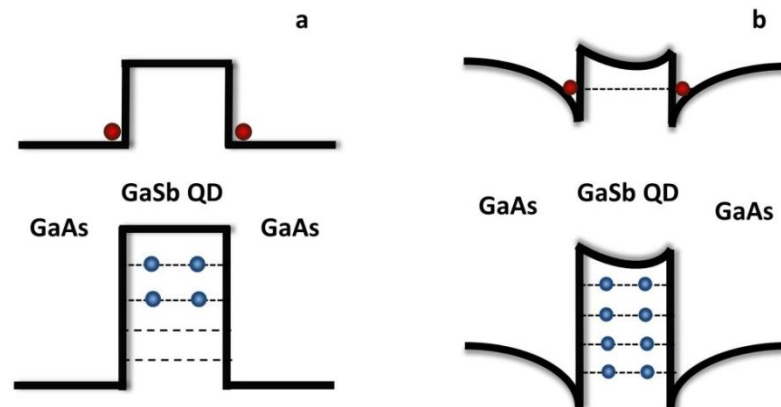
Figure 2.13: Energy band diagrams of GaSb/GaAs QDs a) uncharged and b) charged

2.7.   Photoluminescence

Photoluminescence (PL) data can help in understanding structure related to electronic states in a semiconductor. PL spectroscopy is a contact-less, versatile, non-destructive method which enables the study of the interaction of light and electron-hole

excitations in semiconductors [43]. PL is thus the spontaneous emission of light from a material under optical excitation. This light can be collected and analysed spectrally. In semiconductor systems, the most common radiative transition is between states in or near the conduction and valence band edges. Photo-excitation causes electrons within the material to move into allowed excited states, creating electron-hole pairs. When the electrons return to their equilibrium states through the recombination with a hole, the excess energy is released and may include the emission of light (a radiative process) or may not (a non-radiative process).
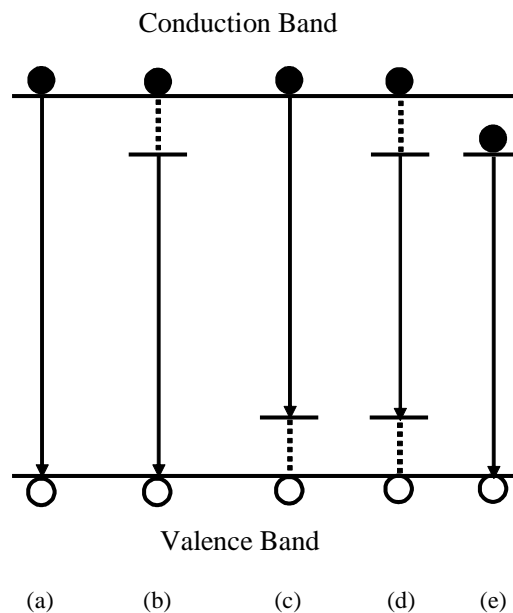
Figure 2.14: Schematic diagram of selected radiative recombination mechanisms, (a) band to band recombination, (b) donor to valance band recombination, (c) conduction band to acceptor recombination, (d) donor to acceptor recombination, (e) excitonic recombination. Straight lines represent photon emission and dotted lines represent phonon emission.

The energy of photoluminescence is related to the difference in energy levels between the electron and hole states involved in the transition. The quantity of the emitted light is related to the relative contribution of the radiative process. The most common

radiative transition in semiconductors is between states in the conduction and valence bands, with the energy difference being known as the bandgap. Radiative transitions in semiconductors can also involve localised defect levels. The photoluminescence energy associated with these levels can be used to identify specific defects, and the amount of photoluminescence can be used to determine their concentration. The amount of photoluminescence and its dependence on the level of photo-excitation and temperature are directly related to the dominant recombination process. Non-radiative processes are associated with localised defect levels, whose presence is detrimental to material quality and subsequent device performance. Thus, material quality can be measured by quantifying the amount of radiative recombination. A diagram of the principle emission processes is shown in Figure 2.14.

Band to band recombination describes the direct conduction band to valence band transitions where the maximum of the valence band and the minimum of the conduction band are in the same position in k-space. Carriers recombining in this way produce photons with an energy equal to (or slightly greater than) that of the band gap of the material described by

$$h\nu = E_{ph} = E_g(T) + \frac{1}{2}kT \tag{2.17}$$

In the donor to valence band recombination process, the loosely bound electron on the neutral donor atom recombines with a hole in the valence band thus emitting a photon of energy less than the band gap energy by an amount equal to the binding energy of the donor described by

$$h\nu = E_{ph} = E_g - E_i + \frac{1}{2}kT \tag{2.18}$$

E_i is the binding energy of the impurity, in this case the donor. Conduction band to acceptor recombination can be described in the same way by using the binding energy of the acceptor in place of the donor. Upon recombination, the vacant acceptor site is left negatively charged until another hole from the valence band fills the vacancy. The electron loses energy, usually in the form of phonons in order for the acceptor site to be re-occupied by a hole. As the temperature increases, thermal energy is more likely to cause the loosely bound donor / acceptor to be excited into the conduction / valence band hence leaving the site ionised. If both donors and acceptors are present in sufficient numbers in the same material, and the temperature is low enough, transitions can occur in which a donor electron recombines with a hole on an acceptor. If they are a distance r apart, they have a coulombic binding energy included in the radiative energy equation described by

$$h\nu = E_{ph} = E_g - \left(E_D + E_A\right) + \frac{e^2}{4\pi\varepsilon_0\varepsilon_r r}, \qquad (2.19)$$

where E_D and E_A are the ionisation energies of the isolated donor and acceptor respectively, ε_0 is the permittivity of free space, ε_r is the relative permittivity of the material. The final term of the expression accounts for the Coulomb interaction between the donor and acceptor atoms on substitutional sites. A series of distinct sharp lines are expected corresponding to the different allowed values of r. However, it is often found that a single broad band is observed in the emission spectrum, with the peak energy value determined by the average distance between the donors and acceptors. These transitions predominate at very low temperatures, where they are usually rather efficient. As the temperature is increased, the probability of the states becoming ionised is increased with the result that many donor-acceptor transitions are not observed at room temperatures unless the recombination centres are very deep.

In a semiconductor material where the carrier concentration is sufficiently low such that the Coulomb attraction between the electron-hole pair is not screened, then excitons can be formed. Thus, in order to observe excitonic recombination, a high quality material and low temperatures are required. Excitons are separated into two classes known as free excitons and bound excitons. A free exciton is comparable in energy level scheme to a hydrogen atom, with a proton being replaced by a heavy hole. When the electron and hole forming the exciton recombine, the emission wavelength peak is characterised by the equation:

$$h\nu = E_{ph} = E_g - E_{fe} \tag{2.20}$$

where, E_{fe} is the energy formation of the free exciton which can also be thought of as the energy required to dissociate the electron and hole pair which is usually only a few meV. When an exciton is localised in the vicinity of an impurity or defect state, the Coulomb interaction between the electron and hole is further enhanced, increasing the binding energy and the thermal stability of the pair. The pair is now a bound exciton. The emission energy of the photon is in this case reduced by the binding energy, E_b, of the exciton to the impurity state:

$$h\nu = E_{ph} = E_g - E_{fe} - E_b \tag{2.21}$$

The bound exciton radiative recombination may occur with or without phonon assistance, and its typical emission peak is narrower ($\sim 10\ \%$) than that associated with the free exciton recombination since there is no contribution from kinetic energy as the exciton is bound to the impurity.

Figure 2.15 shows the exciton formation and recombination for a type II QD such as the GaSb/GaAs encountered in this work. Excitation occurs when a photon of

frequency υ and an energy, $E = h\upsilon_L$ larger than the energy gap (E_g) of the material is directed onto the crystal surface.
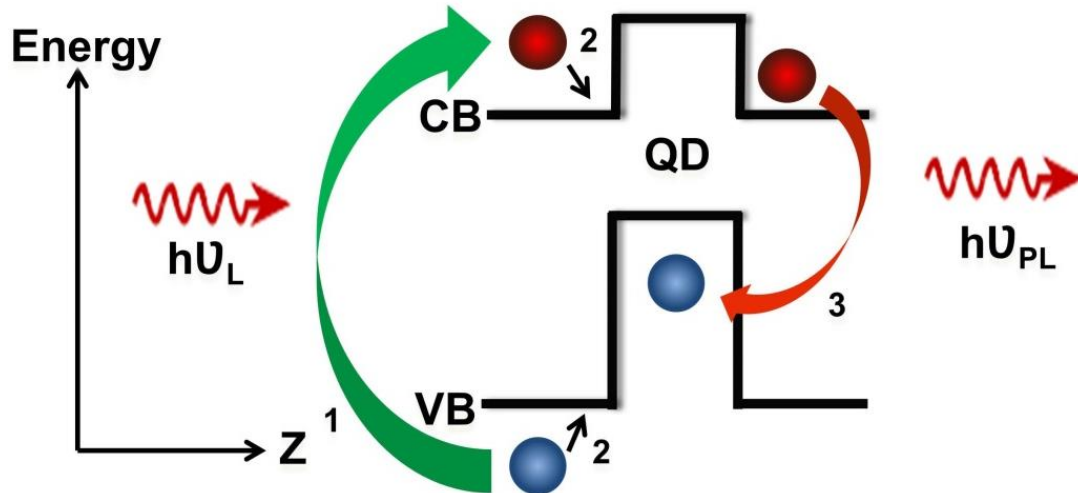
Figure 2.15: A typical 'life-cycle process' for an exciton: 1) an electron-hole pair is created by absorption of photon. 2) The carriers relax through phonon processes. 3) The exciton is formed and later recombines to emit a photon.

Absorption causes an electron from the valence band to be excited across the band gap into the lowest unoccupied energy band, i.e. the conduction band (1). The photo-excited carriers relax under the emission of phonons to the band edge (2). The electron sits on the minimum of the conduction band while the hole is at the maximum of the valence band. They are able to recombine and release spontaneous emission with an energy, $E = h\upsilon_{PL}$ (3).

The performance of quantum dot solar cells is believed to depend on the carrier escape sequence. For most III-V type I nanostructure systems, light holes are found to escape first. To prevent severe open circuit voltage degradation, it is desirable that electrons escape prior to heavy holes. If heavy holes escape before electrons, negative charge may accumulate in the quantum dots strengthening the built in electric field. Such a large negative carrier accumulation in the quantum dot material will locally weaken

the built in electric field in the depletion region and the corresponding escape probability. This is believed to increase the recombination rates resulting in a drop of the open circuit voltage. Because quantum dot solar cells with type II band alignment are characterized by weak electron localization, photogenerated electrons will excite directly to the interface of the GaAs matrix and the GaSb quantum dot. The built in electric field will drift electrons across the depletion region [44]. Thus the electrons are believed to escape from the quantum dots to the matrix prior to heavy holes in type II heterostructures. The holes are strongly confined to the quantum dots and the localization energy is about 450 meV [45]. In the many particle region, the hole-hole interaction of the strongly localized holes dominates the electron-electron and electron-hole interactions. As a result, the thermal activation energy for holes from discrete energy level in GaSb quantum dots to the GaAs matrix decreases from about 450 meV to about 140-150 meV [46] which corresponds to an increase in the average hole occupation of the quantum dots and repulsive force among accumulated holes. With increasing amount of charge in the quantum dots, state filling and coulomb interaction lowers the thermal activation energy and accelerates the rate of escape of holes. Due to these characteristics, a good understanding of the extraction of holes from the QRs is essential for the improvement of solar cell performance. There are three possible processes through which photo-generated holes can escape from the QRs, i.e., photo-excitation, tunnelling and thermionic emission.

2.8. Delta doping of quantum dot solar cells

The properties of semiconductors can be altered by doping. By incorporation of donors and acceptors, the conductance of a semiconductor can be enhanced by orders of magnitude. When the doping atoms release their surplus charges, ionized donors or

acceptors are left behind and act as Coulomb scatterers (ionized impurity scattering) which can inhibit the motion of free charges, blur energy levels, and disrupt the interference of electron waves. The solution of this problem is to separate the active region of the device from the doping atoms, a method which is called delta doping. Delta-Doping is a technique used to get thin layers of high dopant concentration, if combined with annealing to get homogeneous doping. The delta doping of QDs flattens the band structure [84] and can reduce Shockley–Read–Hall recombination in the QDs, which results in a reduced dark current and an improved open-circuit voltage.

2.9. Challenges in quantum dot solar cells

2.9.1. The issue of absorption

Although quantum dots extend the photoresponse of a solar cell, the contribution of quantum dots to the short circuit current density (J_{sc}) of the solar cell is very less due to a small absorption cross section and Quantum dots density. Absorption in quantum dot layers can be increased by increasing the number of quantum dot layers. But the high (7.8%) lattice mismatch between the GaSb epilayer and GaAs substrate complicates the growth of sophisticated device structures by Stranski- Kranstanov method (SK). Currently, this mismatch is accommodated with the necessity to grow thick buffer layers (~1 μm), poor thermal and electrical conductivity, and stacking of more quantum dot layers. It has resulted in significant material degradation through the presence of threading dislocations (TDs).

Another drawback of the Stranski-Krastanov technique to grow GaSb quantum dots is the presence of the wetting layer, which reduces the absorption quality of the quantum dots. Hence the solar cells need to be structured in order to trap the light inside for

increased absorption. Light trapping means increasing the path length of light and hence total absorption layers inside the solar cell. Depositing textures on the solar cell structure can enhance light trapping but reduce the maximum voltage produced by the cell due to the increased carrier recombination at the surface. Absorption of light by QDs can also be increased by coupling them with localized surface plasmons sustained by metal nanoparticles (MNPs).

2.9.2. The issue of open circuit voltage

The introduction of GaSb QDs in GaAs solar cells degrades the open circuit voltage (V_{oc}) and hence lowers the overall efficiency of the device. The reduced V_{oc} is mostly attributed to strain induced dislocations. The strain is always a drawback for epitaxial GaSb QDs. A moderate strain leads to QD formation; while excessive strain induces dislocations. The dislocations are significant for very closely stacked multiple QD layers, degrading both V_{oc} and I_{sc}. Also the dominant thermal escape mechanism in our solar cell structures [47], limits the quasi Fermi level split between the quantum dots and the barrier material leading to reduction in the open circuit voltage [48]. The reduction of bandgap by inserting the QDs can be compensated by using a large bandgap barrier material like $Al_xGa_{1-x}As$ instead of GaAs [49].Experiments have shown that QDs embedded in the depletion region could generate both additional photocurrent and dark current. But, electron-hole recombination in QDs results in additional dark current, which reduces the open circuit voltage and keeps the conversion efficiency of QD solar cells below the Shockley-Queisser limit. The reduction in V_{oc} is due to the accumulation of holes trapped within the quantum dots. The Photo-generated minority holes from the base region undergo drift across the depletion region and are captured by the QDs thereby reducing the short-circuit

current. These trapped holes then act as recombination centres, decreasing the open-circuit voltage. This V_{oc} reduction can be avoided by placing the quantum dots in the flat band region of the solar cell [50]. Previous studies have also shown that delta doping of quantum dots flattens the band structure and reduces SRH recombination and dark current leading to voltage preservation[51]. Hence, it is important to design the quantum dot solar cell by considering two major factors i.e. position of the quantum dots within the solar cell[52] and their doping profile[53].

In this work, single junction type II GaSb/GaAs QR solar cells are characterized to investigate the carrier extraction mechanisms, preservation of open circuit voltage and light absorption.

Chapter 3

Literature Review

3.1. Epitaxial thin film growth

The term epitaxy refers to the growth of a crystalline layer on (epi) the surface of a crystalline substrate, where the crystallographic orientation of the substrate surface imposes a crystalline order (taxis) onto the thin film [54]. Therefore in the process of epitaxial thin film growth, a thin layer of material is grown on the substrate and there is a precise crystal orientation of the film in relation to the substrate. For electronic devices, the substrate is a single crystal (usually Si or GaAs). In the most basic form of MBE, the substrate is placed in ultra-high vacuum (UHV) and the source materials for the film are evaporated from elemental sources.
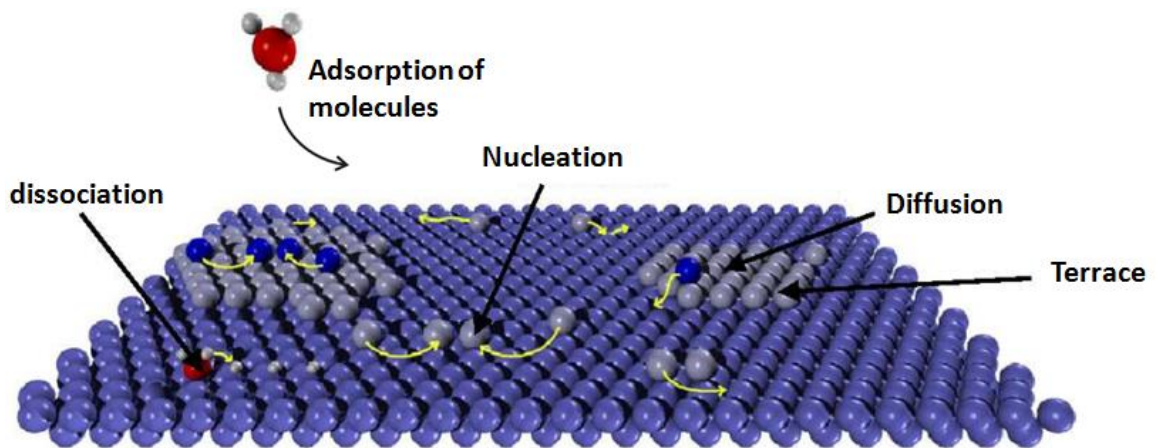
Figure 3.1: Elementary processes at the growth surface during epitaxial growth [55]

The evaporated molecules or atoms flow as a beam, striking the substrate, where they are absorbed on the surface. Once on the surface, the atoms move by surface diffusion

41

until they reach thermodynamically favourable location to bond to the substrate. Molecules will dissociate to atomic form during diffusion or to a favourable site. Figure 3.1 illustrates the processes that can occur on the surface. Because atoms require time for surface diffusion, the quality of the film will be better with slower growth. The typical growth rate is in the order of about one monolayer per sec.
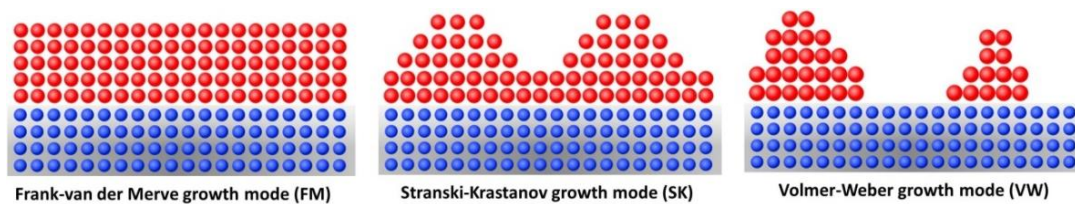
Figure 3.2: Modes of thin film growth [56]

There are three thin film growth modes for the fabrication of III-V heterostructures as shown in figure 3.2. They are, Frank-van der Merve growth mode (FM) Stranski-Krastanov (SK) growth mode, and Volmer-Weber growth mode, growth) Stranski–Krastanow growth is an intermediary process characterised by both 2D layer and 3D island growth. Transition from the layer-by-layer to island-based growth occurs at a critical layer thickness which is highly dependent on the chemical and physical properties, such as surface energies and lattice parameters, of the substrate and film [57] [58]. The coherent island formation during SK growth has attracted increased interest as a means for fabricating epitaxial nanoscale structures, particularly quantum dots (QDs) [59] [60].

3.1.1.   Growth of GaSb/GaAs structures

GaSb quantum dots grown on GaAs has lattice mismatch interface of 7.8 %. In the case of lattice-mismatched materials, strain energy should also be considered together with surface and interface energies.
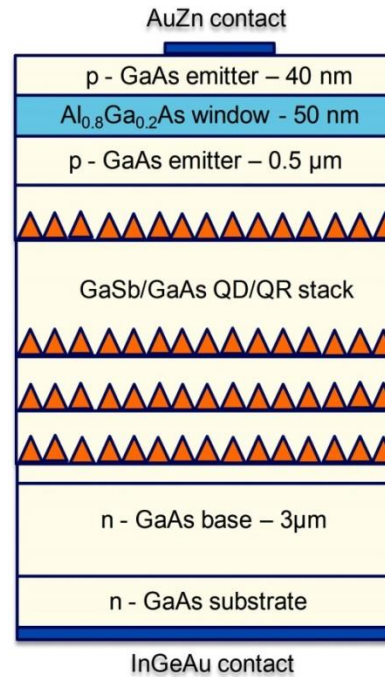
Figure 3.3: Structure of GaSb/GaAs solar cell grown by MBE [61]

The self-organization technique using the Stranski-Krastanov (SK) growth mode is one of the convenient methods to fabricate lattice mismatched QD structures with high dot density [62]. In this mode, wetting layer is formed followed by three dimensional island formation. GaSb QDs were grown using the Stranski–Krastanow self-assembled growth method following an optimised procedure. They were grown on an n-doped (001) oriented GaAs substrate as shown in figure. 3.3. First, a 3 μm thick n-type GaAs:Te base layer with a doping density of 10^{17} cm^{-3} was grown, followed by a 400 nm intrinsic region which contained five or ten layers of GaSb QRs separated by

40 nm GaAs barriers, a 0.5 μm p-type GaAs:Be (2×10^{18} cm^{-3}) emitter layer, a 30 nm

Al$_{0.8}$Ga$_{0.2}$As window layer and finally a thin 40 nm GaAs cap.

Nanostructures are first grown by exposing the GaAs surface to an Sb$_2$ flux for 30

seconds, exploiting an efficient As-Sb exchange reaction to form a thin ~ 0.5

monolayer (ML) of GaSb. Ga and Sb cells are then opened simultaneously and 2.1

ML of GaSb is deposited. The electron diffraction pattern was used to monitor the

growth. The growth changed from streaky to spotty after depositing 1.5 ML of GaSb

and it provided sufficiently high quality of QD layers.

3.1.2. Transformation of quantum dots to quantum rings (QRs)

During the growth process, the GaSb nanostructures tend to preferentially form QRs

rather than QDs, due to a combination of the large strain and strong Sb segregation

[63] as shown in figure 3.4.
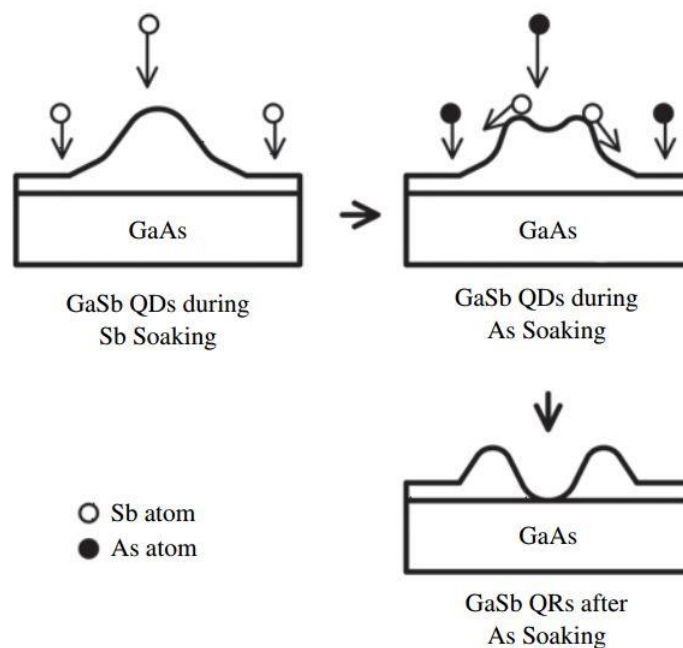
Figure 3.4: Schematic representation of the formation of quantum rings [64]

Figure 3.5 shows the image of scanning tunnelling microscopy of a single GaSb quantum dot and quantum ring. The formation of quantum rings is caused during the GaAs capping due to strong As-Sb exchange [64] and Sb segregation. Here Sb leaks from the centre of the dot and is redistributed towards the edge to stabilize the structure and reduce the net strain.
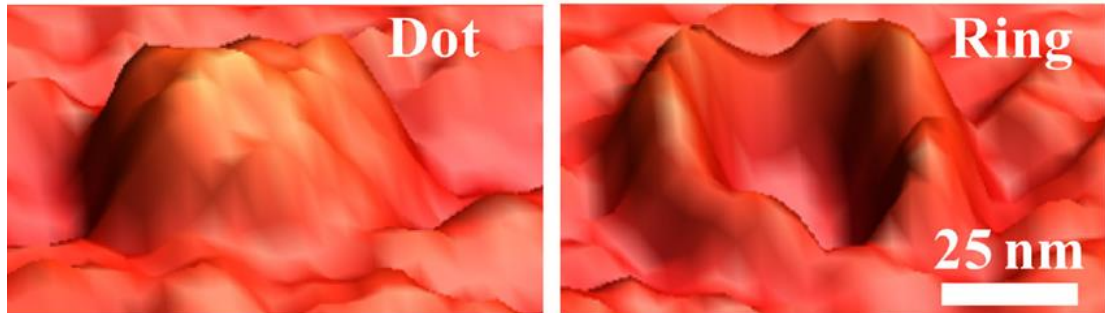
Figure 3.5: Scanning tunnelling microscopy images of a single GaSb dot and ring [65].

To grow predominately GaSb QDs, the growth temperature for the GaAs above the dots must be kept below 500˚C and capped with a thick ~10 nm cold cap. This is below the optimum growth temperature for high quality GaAs and GaSb QDs often contain dislocations. Hence the formation of QRs is allowed in the process. The dimensions of QRs were determined to be approximately 23 nm outer diameter 10 nm inner diameter and 1.7 nm in height from high-resolution transmission electron microscope measurements by using a JEOL 2000FX operating at 200 kV. The ring density per layer was found to be approximately 1×10^{10} rings/cm^2. Normally, threading dislocations are generated during stacking of QD layers due to the build-up of internal strain. But the redistribution of Sb from the centre of the dot towards the edge helps to stabilize the structure and reduce the strain. Hence, GaSb QRs contain fewer intrinsic defects compared to the GaSb QDs [66] making it possible to stack multiple layers in the solar cell to reduce the accumulation of internal strain.
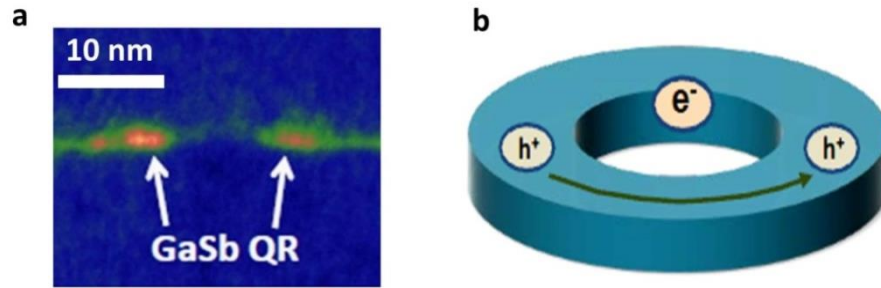
Figure 3.6: a) A cross-sectional Transmission electron microscopy (TEM) image of GaSb QDs. The bright regions show the presence of Sb and indicate the formation of small single monolayer QD; b) Illustration of the band structure of quantum rings, with a deep potential well in the valence band confining heavy holes to GaSb rich regions, and geometric confinement of the electrons in the centre of the rings. [67]

The reduced strain around the QR allows the electron to reside near or inside the QR and in close proximity to the confined holes (figure 3.6 b), which increases the exciton oscillator strength required for efficient light absorption. Peter Carrington and authors have presented an optimum growth method that avoids the cold cap procedure to produce stacked layers of high-purity GaSb/GaAs QRs showing excellent crystalline quality sample [68].

3.2. Single junction solar cells based on III-V semiconductors

Although silicon is the most commonly used material for integrated circuits, a significant number of semiconductor devices and circuits are developed by III–V technology. It is based on crystalline compounds formed by combining the metallic elements from column III and non-metallic elements from column V of the periodic table of chemical elements. III-V based solar cells are the most efficient photovoltaic materials currently available because of their excellent characteristic properties. The combination of these materials from binary to quaternary compounds allows the flexibility of bandgap engineering. Additionally, most of these compounds show

strong interaction with light because of direct bandgaps and high absorption coefficient suitable for optoelectronic applications. Due to its direct bandgap electronic structure they are capable of absorbing 97% of the AM1 radiation of about thickness of 2 μm [69]. Therefore they are good materials for high efficiency single junction and multi-junction solar cells. GaAs is considered to be the most important compound of the group because GaAs is often used as a substrate material for the epitaxial growth of other III-V semiconductors including: Aluminium gallium arsenide (AlGaAs), Gallium antimonide (GaSb) and Indium gallium arsenide. Also, GaAs is capable of producing higher efficiency than any other III-V materials in a single-junction solar cell design. Brendan M. Kayes and authors have demonstrated a new record of 27.6% conversion efficiency under AM1.5G simulated sunlight without concentration, with a thin-film GaAs device [70]. For a single-junction solar cell the maximum theoretical efficiency increases from 33 to 41% under concentration from 1 to 1000 suns. However, the optimum bandgap decreases from 1.2 eV (1 sun) to nearly 1 eV (1000 suns), which is significantly below the bandgap of GaAs (Eg =1.4 eV) [71].There is increasing interest in the incorporation of the quantum dots (QDs) within the active region of GaAs-based single or multi-junction solar cells as a means of absorbing long wavelength photons to extend the photoresponse and increase the quantum efficiency.

Previous studies of QD solar cells have focused on type-I InAs/GaAs [72] and InGaAs/GaAs [73] QDs, where an enhancement of the long wavelength photoresponse of up to ~1100 nm has been realised. An attractive alternative system is the GaSb/GaAs quantum dots (QDs), where the band alignment is type-II, such that the holes are localised within the GaSb QDs, but with no electron confinement. Such

GaSb QDs have exhibited an enhanced infrared photoresponse extending beyond 1 μm (figure 3.7) and an increase in the short-circuit current (J_{sc}) [74].
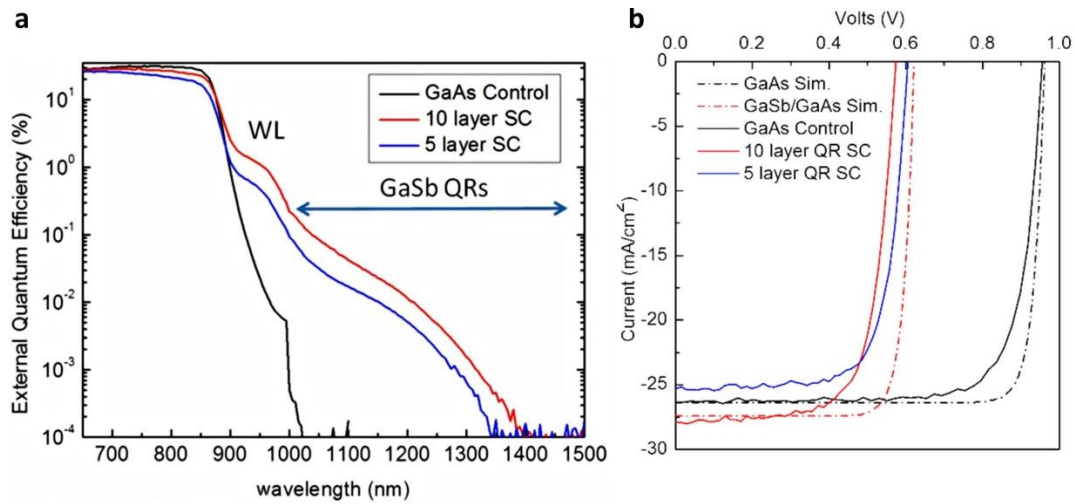
Figure 3.7: a) Extended spectral response and b) increased J_{sc} of GaSb/GaAs QR solar cell [74]

The type-II band alignment produces a red-shift of the photoresponse compared with the type-I QD structures such as InAs/GaAs [72]. In addition the lower electron-hole wave function overlap results in longer radiative lifetime which improves carrier extraction. The incorporation of type II GaSb QDs has also been proposed as a way to realise an intermediate band solar cell, because the spatial separation of electron and holes can be engineered, provided an intermediate band is closer to the theoretical optimum and reduces unwanted thermal emission and capture processes [75] [76]. But larger effective mass of the holes in GaSb compared with InAs could result in more confined states with a consequent reduction in the separation between the QD confined states and the valence band. The separation can ultimately result in the reduction of the effective band gap of the cell and a reduction in the V_{oc}. Also, V_{oc} reduction may be because of the increased recombination within the GaSb QRs and thermal coupling between the valence bands [77], or crystalline quality of the surrounding GaAs. Under AM1.5 illumination (1 sun intensity), these GaSb QD solar

cells displayed an enhanced J_{sc} compared with the GaAs control cell (~6%) but with a reduced open-circuit voltage (V_{oc}). The analysis of the photoresponse under the white light illumination has shown that some photo-generated minority holes from the base region can be re-captured by the QDs, which reduces the J_{sc} and the V_{oc}. Compared with GaSb QD, the GaSb QR nanostructures can provide epitaxial layers having less strain, which is very beneficial in stacking such layers to enhance the light absorption at longer wavelength. In strained QDs, there is a significant increase in the conduction band minimum energy of the GaAs close to the QD [78]. Therefore, gradients in the GaAs conduction band minimum may lead to strong electron repulsion from the highly strained QDs. Whereas the QR formation is very effective at relaxing the strain [68], hence producing a lower gradient in the GaAs conduction band, allowing greater electron-hole wave-function overlap. This results in more surrounding electrons over the GaSb QRs (figure 3.6), which results in the QRs having a higher optical recombination rate than the QDs. Recently, GaSb/GaAs QR solar cells with extended infrared response up to 1400 nm have been demonstrated [79]. Furthermore, in this system, it has also been shown that the sub-bandgap response is limited by the thermionic emission of holes from QRs [80]. In this thesis, QRs are directly probed by using an infrared laser (1064 nm) where the photon energy is conveniently chosen below the bandgap of the GaAs matrix. This enables us to investigate the carrier dynamics and extraction mechanisms occurring in the GaSb QRs under high light concentration. Dependence of the photocurrent on the laser intensity, the bias and the temperature is also discussed [81]. Experiments have shown that QDs embedded in the depletion region could generate additional photocurrent. But electron-hole recombination in QDs results in additional dark current which reduces the open circuit voltage and keeps the conversion efficiency of QD solar cells below the Shockley-

Queisser limit. Using a GaSb/GaAs type II QD absorber embedded in the p-doped region of an ideal solar cell but spatially separated from the depletion region is expected to lead to voltage preservation[82]. Meanwhile, improvements in voltage preservation through suppression of hole thermionic emission rates by n-type doping at the expense of reduction in short circuit current and by positioning of QD layers at the edge of the space charge region have been reported[83].
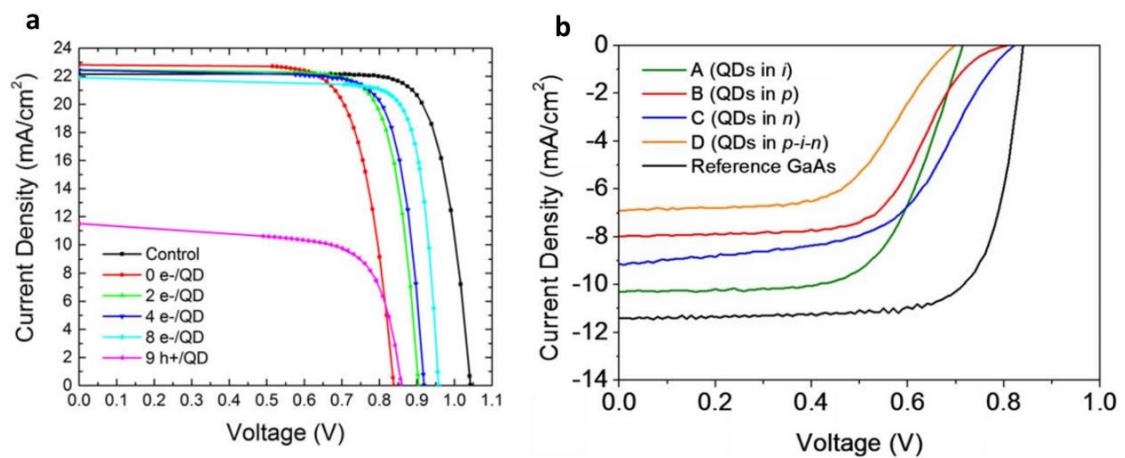
Figure 3.8: a) Delta doping effects on V_{oc} [84] and b) Positioning effects on V_{oc} [85]

Previous studies have also shown that delta doping of quantum dots flattens the band structure and reduces SRH recombination and dark current, leading to voltage preservation[84] . Hence, it is important to design the quantum dot solar cell by considering two major factors i.e. Position of the quantum dots within the solar cell [85] and their doping profile [86]. Therefore in this thesis, the approach of placing QDs in the n or p region of the solar cell and the effects of delta doping of quantum dots have been investigated. Though QDSC shows extended photoresponse, their contribution to J_{sc} is very small due to small QD absorption cross section. It has been demonstrated that the use of metal nanostructures in solar cells produces stronger field and greater absorption enhancement. But the light absorption in the solar cell is

sometimes overestimated [87]. This is because; some other materials can absorb light in addition to the absorption layer but do not contribute to the photocurrent. The light absorbed by the absorption layer can only contribute to the photocurrent. So it is not correct to estimate the solar cell efficiency just by calculating the whole absorption of the cell. Hence it is important to analyse the absorption in the absorption layer of the thin film solar cells in detail [88].

3.3. Carrier dynamics of GaSb/GaAs quantum dots/quantum rings

In GaSb/GaAs QD/QR structures, only holes are deeply confined and need to be efficiently extracted out of the QRs so that they can contribute to the photocurrent. However the photo-generated electrons are relatively weakly bound to QRs by Coulomb attraction and hence can easily diffuse away to the electrode.
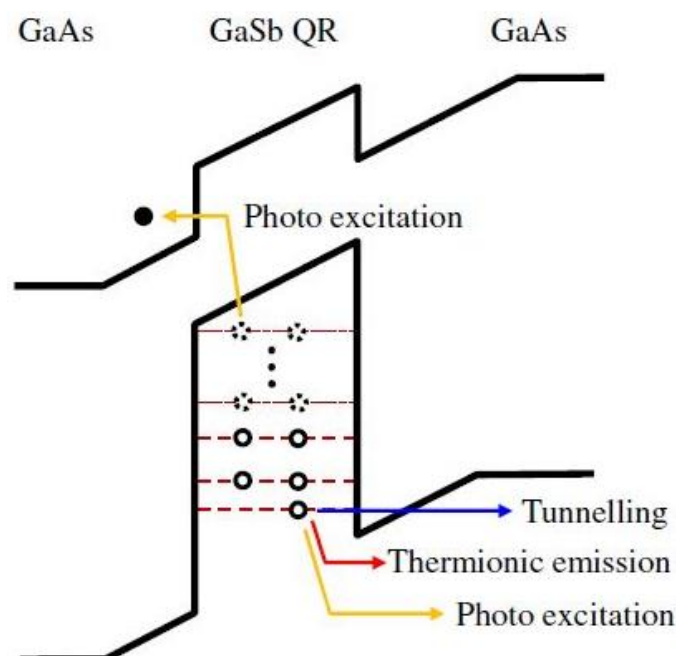
Figure 3.9: The schematic band diagram showing the possible hole extraction processes from type II GaSb QRs/GaAs [89].

This should lead to the reduction of electron–hole wave function overlap, resulting in longer carrier lifetime and improved photo-carrier extraction. The growth of GaSb/GaAs structure by MBE, leads to the introduction of carbon impurities into the sample. Hence in the dark, the dots are filled with holes from carbon acceptors. Due to these characteristics, a good understanding of the extraction of holes from the QRs is essential for the improvement of solar cell performance. There are three possible processes through which photo-generated holes can escape from the QRs, i.e., photo-excitation, tunnelling and thermionic emission as shown in figure 3.9.
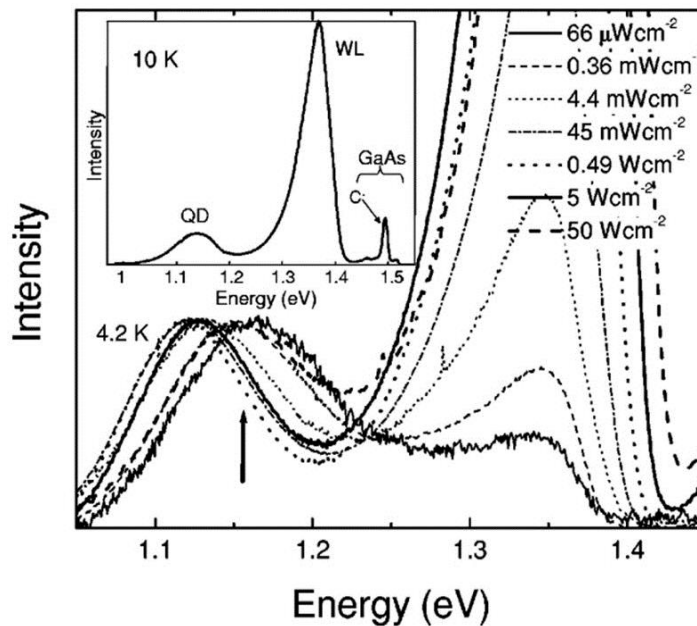
Figure 3.10: Dependence of the QD PL on incident laser power density P at 4.2 K. The inset shows a complete PL spectrum of sample A at 10 K [91].

Figure 3.10 shows the PL spectrum of QDs at 4.2 K. It is dominated by the WL peak at about 1.37 eV. The group of peaks around 1.5 eV are from the GaAs matrix [90]. The QD peak is seen around 1.15 eV as a low intensity line. The inset showing a peak labeled C− at 1.49 ev is attributed to recombination between free electrons and holes

bound to carbon acceptors. At high laser powers, the WL peak dominates, whereas at low laser powers it almost disappears. The QD PL energy decreases as the laser power is increased, reaches a minimum of around 0.05–0.5 W cm^{-2}, and then starts increasing. In other words, as the laser excitation is increased from very low levels, the PL shows a strong red shift, and then a blue shift, thereby presenting a U shaped curve. M.Hayne and authors explained this effect by population and depopulation of holes in the dots using photo excitation of Laser at different power densities [91].
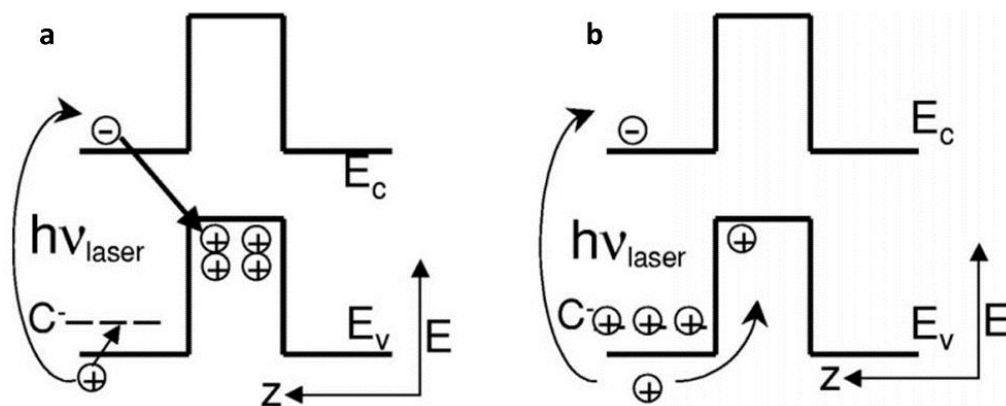
Figure 3.11: Schematic representation of the mechanisms for depopulation and repopulation of the dots with holes. a) at low laser power b) at high laser power [71]

The mechanism for depopulation and repopulation of the dots with holes are shown in the figure 3.11. The photoexcited holes are captured by unoccupied carbon acceptors, C- at low laser powers. Whereas, the photoexcited electrons recombine with the holes in the QDs leading to hole population reduction and red shift in the PL. At high Laser powers, all the carbon acceptors are occupied leading to rapid hole capture by the QDs and blue shift in the PL. Kai Cui and authors reported the temperature dependent photoexcitation by laser to study the thermal influence on carrier dynamics of GaSb quantum dots [92]. A slight blueshift in the PL peak was observed initially when increasing the temperature and then redshift after the temperature is raised beyond

about 110 K. Figure 3.12 shows the dependence of the QD PL peak position on the temperature. The redshift of the PL peak arises from the bandgap shrinkage when the temperature is raised.
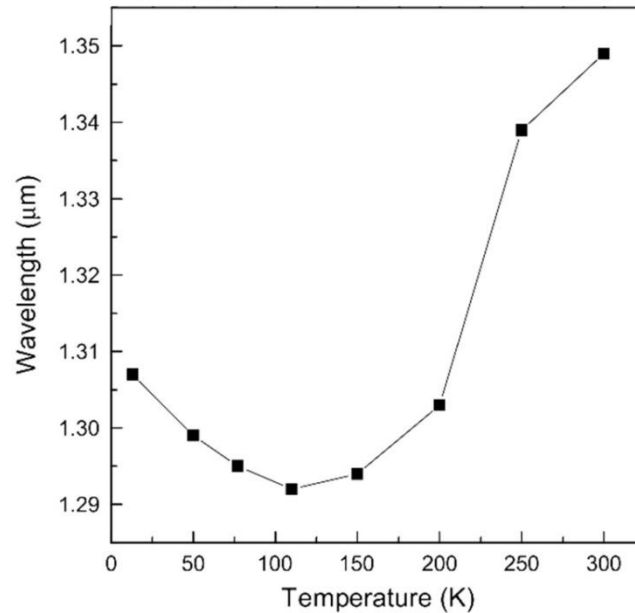
Figure 3.12: The dependence of the PL peak position on temperature for GaSb/GaAs QDs [92]

However, at low temperature range, the blue shift of the PL peak for an increased temperature can be accounted for by considering the dot size non-uniformity. The photogenerated holes tend to occupy the large dots; when temperature is increased, the holes in the large dots are easier to transfer into the small dots resulting in a blue shift dependence of the PL peak position on temperature. When temperature is above 110 K, the decrease in the bandgap energy due to an increased temperature starts to dominate the PL peak position and thus, a redshift dependence on temperature is observed.

PL.A. F. G. Monte and Fanyao Qu reported a nonlinear dependence of photocurrent on the laser excitation power. They predicted that the accumulation of holes trapped in QDs is responsible for the nonlinearity [93].
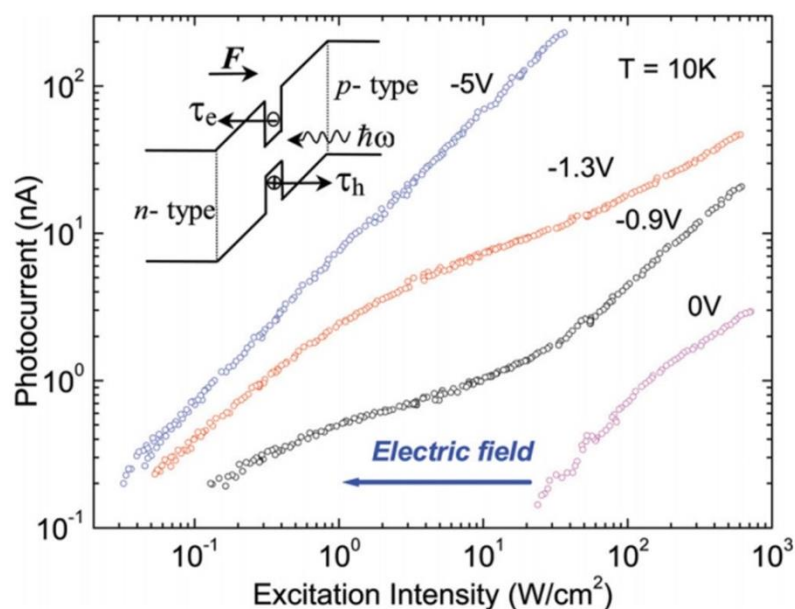
Figure 3.13: Schematic Photocurrent signal as a function of excitation intensity for four different bias voltages. Inset shows a schematic diagram of confinement potential and carrier escape process, where F represents electric field [93].

Figure 3.13 demonstrates the photocurrent signal of the sample excited by a Ti:sapphire laser versus excitation density for four different bias voltages. For the bias voltage (0 V and -5 V), photocurrent signal presents a linear dependence with power density. However, for the other values (-0.9 V and -1.3 V) the nonlinear behaviour is noticed. These observed nonlinearities arise from accumulation of photo-generated holes. The competition between quantum confinements (favours an accumulation of holes inside the QD) and the quantum stark effect (favours carrier tunnelling) results in the nonlinear photocurrent phenomena. However, the photocurrent of a solar cell is determined by the competition between the carrier

escape rate and the recombination rate in the QRs. Neglecting the later, the total escape rate is given by [94],

$$\frac{1}{\tau_{esc}} = \frac{1}{\tau_{tun}} + \frac{1}{\tau_{th}}$$

(3.1)

where, τ_{tun} and τ_{th} are tunnelling and thermionic emission lifetimes respectively. We assume that the photocurrent can therefore be described by

$$I = I_{tunnel} + I_{thermionic} \exp\left(-E_a\middle/kT\right)$$

(3.2)

where, the terms in I_{tunnel} and $I_{thermionic}$ represent the temperature independent tunnel current and temperature dependent thermionic current contributions respectively, k is Boltzmann's constant, and E_a is the thermal activation energy for the escape of holes from the GaSb QR [95]. With increasing temperature, the thermal escape rate increases and dominates over both the recombination rate and the tunnelling rate. As shown in figure 3.14, the activation energy for the QDs increases with reverse bias leading to the depletion of holes. This indicates a possible decrease in coulomb charging energy in the QDs, as holes are depleted with increasing reverse bias. The coulomb charging energy of the n holes in a QD is given by Hwang et al [96]. The coulomb charging energy E_N required to charge N holes into a QD may be expressed as

$$E_N = \frac{\left(N - \frac{1}{2}\right)q^2}{4\varepsilon_{GaAs}\varepsilon_0 D}$$

(3.3)

where D is the typical diameter of dots, ε_0 is the vacuum dielectric constant, and ε_{GaAs} is the dielectric constant of GaAs. The thermal activation energy of hole carriers in energy level of E_1 may be expressed as

$$E_a = E_{wt} - E_{QD} - E_N - \frac{qFh}{2} \tag{3.4}$$

where E_{wt}, and E_{QD} are the energy of the wetting layer (1.3 eV) and quantum dots 1.12 eV), F is the built in electric field and h is the height of the quantum dots.
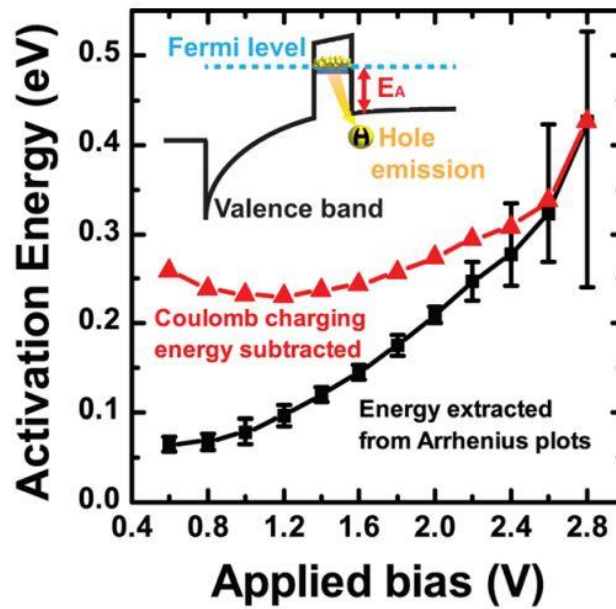
Figure 3.14: Activation energy extracted from Arrhenius plots and obtained by subtracting Coulomb charging energy of GaSb/GaAs QDs [97].

The activation energy extracted for the QDs increases with reverse bias, indicating a possible decrease in Coulomb charging energy in the QDs as holes are depleted with increasing reverse bias. The thermionic emission rate of holes, τ_{th}, can be approximated using [98],

$$\tau_{th} = \sigma_a \upsilon_{th} N_v \exp\left(\frac{-E_a}{\kappa T}\right) \tag{3.5}$$

where σ_a is the capture cross section for holes (between 10^{-16} to 10^{-13} cm^{-2}), υ_{th} is the thermal velocity of holes (1.3×10^7 cm.s^{-1}), N_V is the density of states in the valence band and E_a is the hole thermal activation energy.
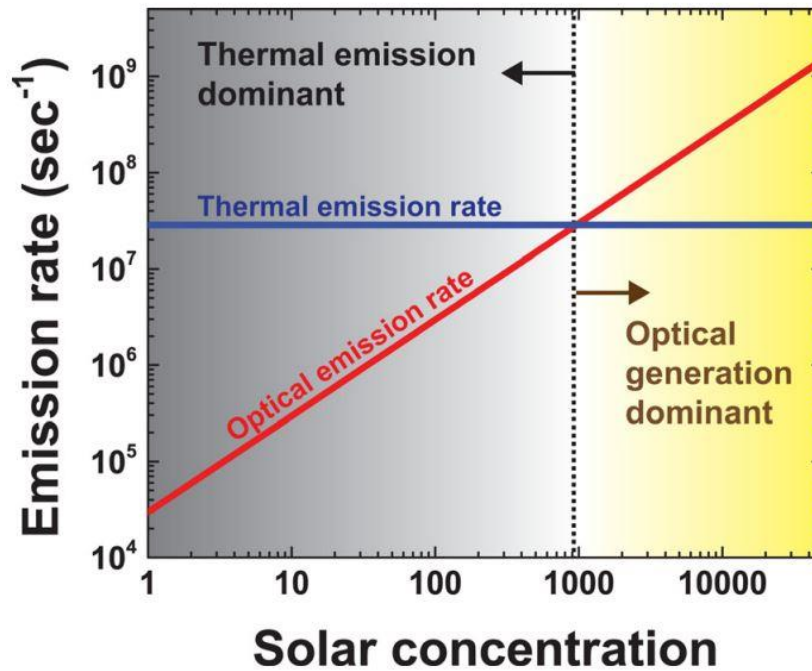
Figure 3.15: Optical (red) and thermal (blue) emission rates of holes in GaSb/GaAs QDs under different solar concentration [97]

The thermal emission rate of holes from QD states to the GaAs valence band may be compared to the optical generation rate [97]. A comparison of the optical and thermal emission rates under varying solar concentration is shown in Fig. 3.15, where thermal emission is dominant for AM1.5 illumination, whereas optical generation becomes dominant under full solar concentration. In order to further improve the solar cell performance, hole capture by QRs must be reduced, and/or the hole extraction rate from the QRs must be increased, not only for photocurrent enhancement but also to

improve V_{OC}. For this, a more detailed understanding of the photo-carrier dynamics is essential, especially under high solar concentration conditions under which these solar cells will be used. A slight increase in the efficiency (10.31 % vs 10.29) is reported for the GaSb QR device against the GaAs control device under solar concentration [99]. The QR samples shows recovery of V_{oc} under solar concentration (fig 3.16).
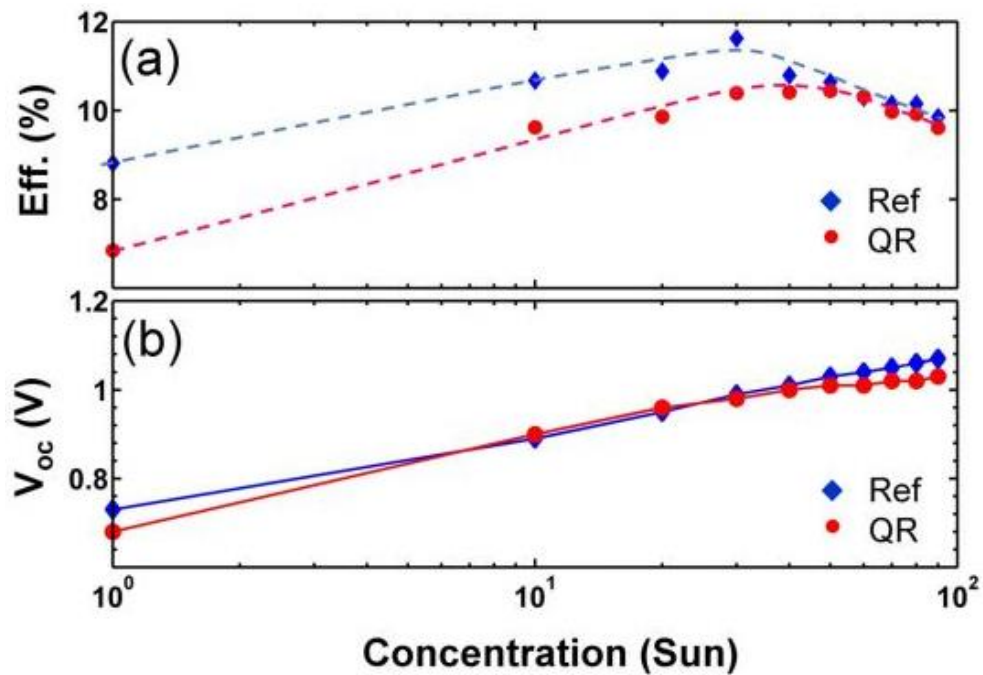
Figure 3.16: (a) The power conversion efficiencies of the reference and GaSb QR samples versus different concentration factor. The dashed lines are for eye-guiding only. (b) The V_{OC} under the same condition [99]

The behaviour of V_{OC} as shown in figure 3.16 is an indication of the enhanced two-photon transition. However, the two photon absorption processes will be offset under the one sun condition because of the strong non-radiative recombination and thermal capture/emission. The thermal emission process is the dominant hole escape mechanism compared to tunnelling and photo-excitation in the photocurrent of our GaSb/GaAs QRs solar cells. Although the tunnelling process gives relatively weak contribution to the photocurrent, this process could be enhanced by applying

additional reverse bias voltage [100]. This suggests that increasing the built-in electric

field surrounding the QRs in the intrinsic region of the GaAs p-i-n structure could

improve the QR solar cell performance. If the reverse bias voltage is increased, the

electric dipole moment is strongly enhanced due to the movement of electron and hole

along an opposite direction driven by applied bias [93]. This results in the decrease of

recombination probability accompanied by increase of tunnelling rate. The tunnelling

rate, τ_{tun} from QR can be expressed as in equation 6 [101] using the electric field F, the

heavy hole effective mass m_{hh}, and the tunnelling barrier height E_b,

$$\tau_{tun} \propto \exp\left(\frac{-4}{3\hbar eF} \sqrt{2m_{hh}E_b^3} \right)$$

(3.6)

Since the multi-layered self-assembled QDs possess thick tunneling barriers, the

photo-generated carriers have to tunnel through these barriers to reach the electrodes.

The barrier height can be reduced by further increasing the reverse bias voltage which

facilitates carrier tunnelling.

If most of the carriers created in the QRs by photon absorption escape before

recombining, the absorption will be directly proportional to the photocurrent [102].

Therefore the photocurrent measurements enable the absolute values for the

absorption strength (A) to be obtained by using the expression [103]

$$I = \frac{APe\lambda}{hc}$$

(3.7)

where I is the photocurrent, P is the total incident optical power of the laser at the

wavelength λ and h and c have their usual meaning. The transition energies of carriers

in QDs and in a WL can be determined by analysis of below-bandgap absorption

[104]. For the first time, Tian Li and authors used a measurement of EQE at room temperature to derive the spectral dependence of the QD absorption in type I InAs/GaAs QD solar cell. The absorption coefficient of quantum dots below the band gap depends exponentially on the photon energy given by the Urbach tail [104]

$$\alpha_{urbach} = \alpha_0 e^{\frac{E_g - \hbar\omega}{E_U}} \tag{3.8}$$

where E_U is the Urbach energy and α_0 is the scaling parameter. The absorption strength of QDs states could be calculated by the analysis of EQE measurement. The equation relating the EQE with the absorption coefficient is given by

$$\eta_{ext} = (1-R)(1-e^{-\alpha L})\eta_{int} \tag{3.9}$$

where η_{ext} is the external quantum efficiency, η_{int} is the internal quantum efficiency, R is the surface reflectivity (~0.3) and L is the layer thickness. Quantum dots and the wetting layer energy states contribute to the absorption coefficient in the QD devices. Hence the Urbach tail absorption can be written as:

$$\eta_t = \eta_{urbach} + \eta_{QD \& WL} \tag{3.10}$$

where η_t denotes the total measured EQE consisting the EQE contributions via Urbach tail absorption (η_{Urbach}) and the EQE contributions via QDs and WL absorption ($\eta_{QD\&WL}$).

The Urbach EQE is given by

$$\eta_{urbach} = (1-R)(1-e^{-\alpha_{urbach}L})\eta_{int} \tag{3.11}$$

Where, $\alpha_{urbach}L$ is given by the following expression,

$$\alpha_{urbach}L = -\alpha_0 e^{\frac{-1.424 \, -\hbar\omega}{E_U}} \qquad\qquad (3.12)$$
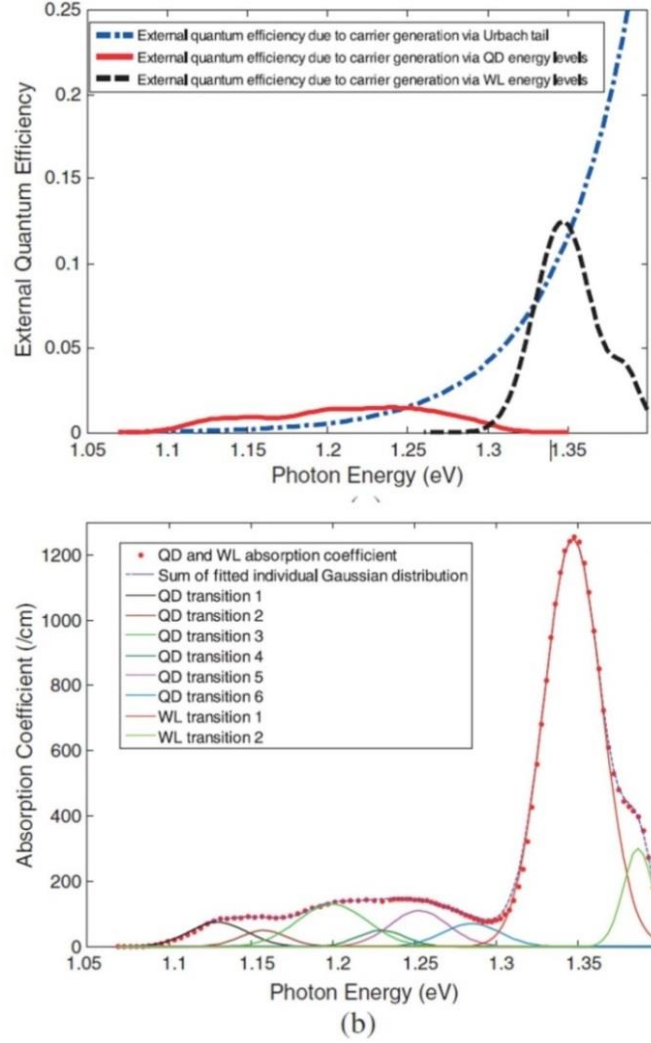
Figure 3.17: (a) External quantum efficiency due to carrier generation via the Urbach tail and the QD and WL energy levels (b) derived quantum dot and wetting layer absorption coefficient and the Gaussian line shape fitting for multiple transitions [104].

The absorption coefficient contribution of the QD and WL to $\eta_{QD\&WL}$ is given by the following expression:

$$\eta_{QD\&WL} = (1-R)(1-e^{-\alpha_{QD\&WL}L})\eta_{int}$$

<div align="right">(3.13)</div>

The Urbach energy E_u characterizes the degree of disorder within the semiconductor material. For the QD devices, the Urbach energy broadens because of the disruption to the lattice by built-up strain. This continuum tailing density of states provides a competing path for the carriers on the intermediate states to be directly collected. In this thesis, the Urbach tail absorption through EQE contribution from QDs and WL has been studied for type II GaSb/GaAs solar cell structures.

Chapter 4

Experimental techniques

The experimental work in this thesis covers the sample growth by molecular beam epitaxy (MBE), morphology imaging by atomic force microscopy (AFM), Device processing, photo-luminescence (PL) spectroscopy, photovoltaic I-V measurement, photocurrent spectroscopy and capacitance voltage measurements as detailed below.

4.1. Molecular Beam Epitaxy (MBE)

A VG V80H MBE system was available at Lancaster University. In an MBE system, there are three ultra-high vacuum chambers which are a load-lock preparation chamber; an intermediate transfer chamber and a growth chamber (figure 4.1). Each of these chambers is independently pumped. Transfer of the sample between chambers is accomplished using magnetically coupled transfer rods, allowing the sample to be moved without breaking vacuum states. These chambers are equipped with pump systems that give base pressures in the 10^{-11} Torr range. The MBE growth chamber is in ultra-high vacuum environment to guarantee formation of a molecular beam. Without this level of vacuum, the atoms or molecules leaving the effusion cells would be scattered as residual gas molecules and never form a beam. This beam is directed at a heated substrate. Similar to the spray of individual paint droplets from the nozzle of a spray–paint can, broad beams of individual atoms or molecules are generated by evaporation or sublimation of the pure source materials. However, unlike paint droplets, the atoms do not just stick where they land. Instead, the heated substrate allows the recently added atoms to migrate a short distance until they find

a favourable site to become part of the single crystal. An MBE growth is performed in a chamber consisting of a substrate manipulator, effusion cells and monitoring equipment. Each effusion cell is a source of one element in the film. The effusion cell, also called a Knudsen cell, contains the elemental form in very high purity (greater than 99.99999% for Ga and As). The cell is heated to encourage evaporation. For GaAs growth, the temperature is typically controlled for a vapor pressure of 10^{-2} to 10^{-3} Torr inside the effusion cell, which results in a transport of about 10^{15} molecules/cm^2 to the substrate when the shutter for that cell is opened. The shape and size of the opening in the cell is optimized for an even distribution of particles on the substrate. Due to the relatively low concentration of molecules, they typically do not interact with other molecules in the beam during the 5 - 30 cm journey to the substrate. The substrate is usually rotated, at a few rpm, to further even the distribution.
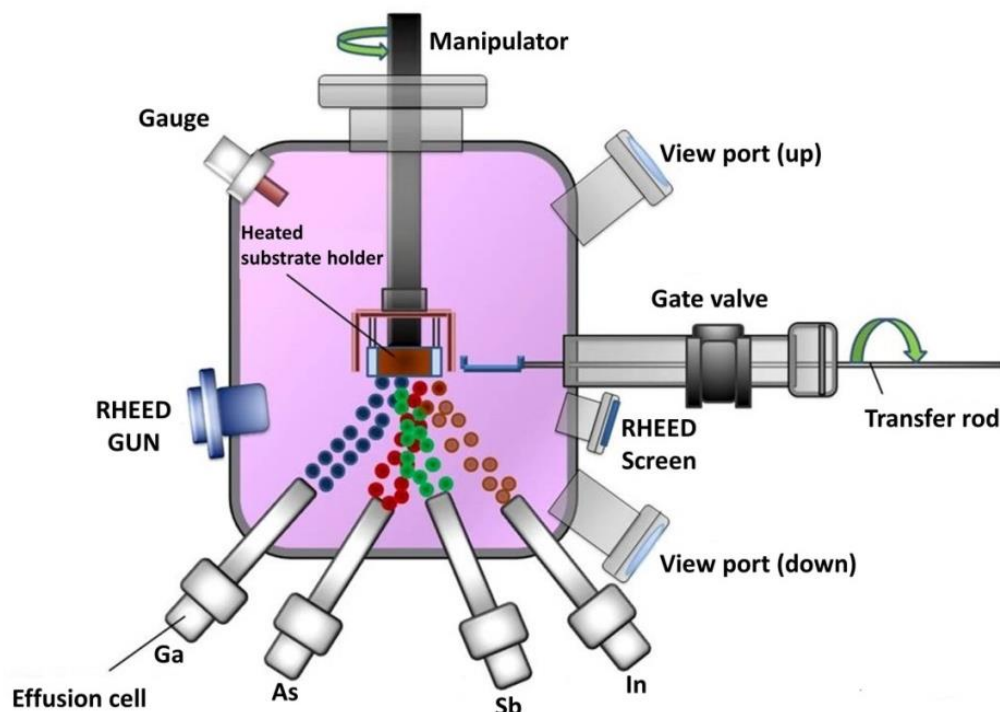
Figure 4.1: A schematic diagram of MBE sample growth chamber [105]

4.1.1. Growth of GaSb quantum ring Solar Cells by MBE

A series of undoped samples containing single, five and ten stacked layers of GaSb/GaAs QRs were grown on n-GaAs (001) substrates using a VG-V80H MBE reactor. Thermal effusion K-cells were used to supply the In, Ga and Al fluxes, and two (Veeco) valved cracker cells were used to provide Sb_2 and As_2. In situ reflection high-energy electron diffraction (RHEED) was employed to monitor surface reconstruction. The substrate temperature was measured using an infrared pyrometer calibrated using surface reconstruction transitions under a fixed As flux. A 300 nm GaAs buffer layer was first grown at 570 ^{0}C and then the temperature reduced under an As flux to 480 ^{0}C for GaSb deposition.
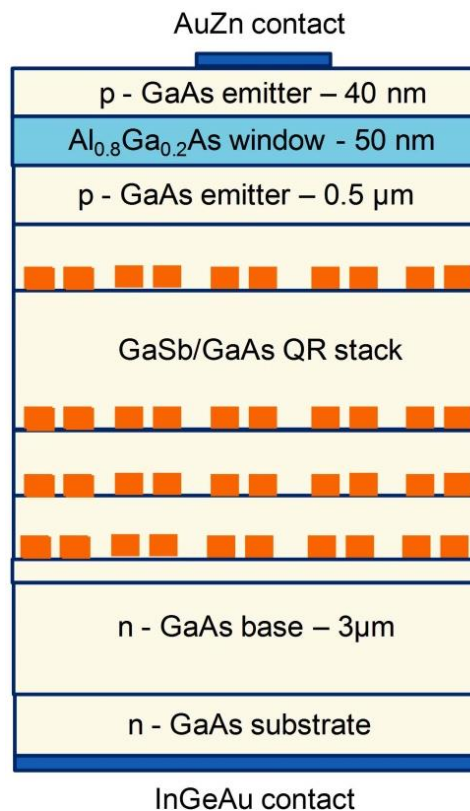
Figure 4.2: Generic structure of solar cell grown for this work by MBE at Lancaster containing a stack of GaSb quantum rings

The GaSb QRs were formed by firstly exposing the GaAs surface to an antimony flux for 30s, exploiting an efficient As-Sb exchange reaction to form a thin ~ 0.5 ML (monolayer) GaSb layer. Following the exchange procedure GaSb is directly deposited using a Ga growth rate of 0.3 ML/s, producing between 1.5 ML or 2.1 ML nominal thickness of GaSb. The formation of the QRs was detected by a change in the RHEED pattern from streaky to spotty after the deposition of approximately 1.3 ML of GaSb. The QRs were firstly capped by a thin 10 nm GaAs layer at the same growth temperature and then a 40 nm GaAs cap at 570 ^{0}C. The solar cells contains 5/10 layer QDs which is intrinsic region, p-doped region of a P-I-N diode and front & back contact. These cells containing 1.5 or 2.1 ML of GaSb QRs were grown and shown in figure 4.2. A 3 μm n-type GaAs:Te layer was grown first at 570 °C with a doping density of 10^{17} cm^{-3}. This was followed by an intrinsic region containing between 5 and 10 GaSb QR sheets as described above.
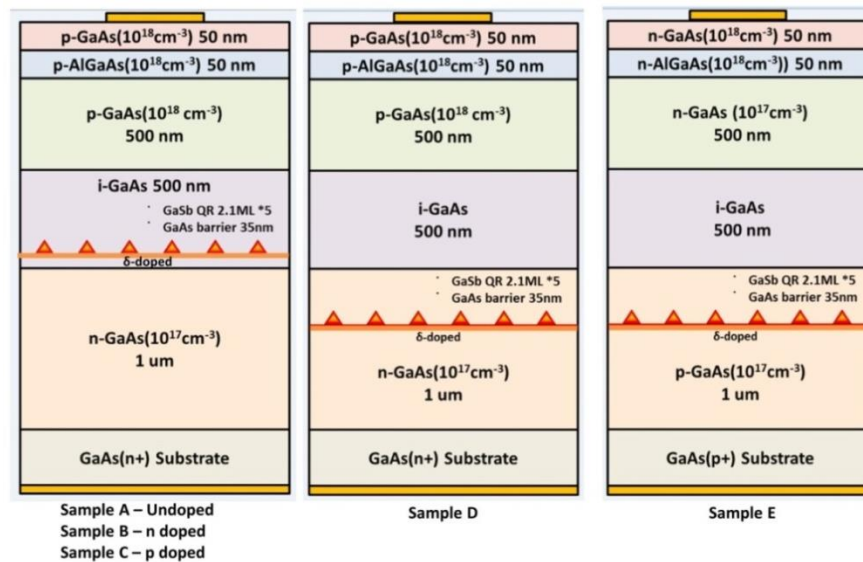
Figure 4.3: Schematic structure of QR SCs: Sample A-undoped QRs grown in intrinsic region, Sample B- n-doped QRs grown in intrinsic region, Sample C-p-doped QRs grown in intrinsic region, Sample D-n doped QRs grown in n-region, Sample E-p- doped QRs grown in p-region

Finally a 0.5 μm p-type GaAs:Be layer with doping density of 2×10^{18} cm^{-3} is grown followed by a 30 nm Al$_{0.8}$Ga$_{0.2}$As window layer and a 40 nm GaAs cap. Finally a GaAs control cell (without intrinsic layer) was also fabricated without quantum dots as a reference cell to compare the contribution of QDs in the solar cell performance. Delta-Doping is a technique used in MBE to get thin layers of high dopant concentration, if combined with annealing to get homogeneous doping. Delta doping can lead to higher mobilities since the carriers are, in the average, more distant from the ionized impurities than in the case of conventional homogeneous doping. Figure 4.3 shows the delta doped solar cell structure grown at Lancaster. The effects of Delta doping of GaSb QRs on the solar cell performance is studied in this thesis.

4.2. Device Processing

The solar cells were processed in the class 100 clean room at Lancaster University Physics Department using conventional photolithography and wet etching techniques. The processing consisted of seven steps; Bottom contact metallization, photolithography, top contact metallization, photolithography prior to mesa etch, mesa etch, device cleaving and mounting. Before any of these steps however, the sample was cleaned using acetone and propanol and distilled water to clean the impurities.

4.2.1. Bottom Contact Metallization

Evaporation of InGe: Au followed by thermal annealing at ~420°C for 3 seconds was used to form the bottom contacts on the devices. 20 mg of Indium and Germanium (1:1 ratio) and 3 cm gold wire was kept in the alumina coated crucible inside the thermal evaporator. The sample was placed in the Thermal evaporator and pumped to

~1x10^{-6} Torr. 20 nm of InGe and 200nm Au was deposited on the sample. The thickness was measured using thin film thickness monitor.

4.2.2.   Photolithography

Photolithography is a process that uses light to transfer a geometric pattern from photomask to a light sensitive chemical photoresist. The sample was held by vacuum in a spinner and few drops of LOR spun on at 3800 rpm for 45 seconds. The sample was then placed in hot plate at ~180°C for 4 minutes. Photoresist 1805 was spun on at 4000rpm for 30 seconds. Then the sample was placed in a hot plate at ~115°C to harden the resist before being placed under the required photolithography mask and aligned using an X-Y stage. Ultra-violet light from the mask aligner was then used to soften the photoresist by exposing the sample for about 1.2 seconds. The sample was then placed into developer for 30 seconds and rinsed in de-ionised water and dried using nitrogen. Acetone was used to remove the hardened resist after either the metallization or the mesa etching step and was controlled visually under a microscope.
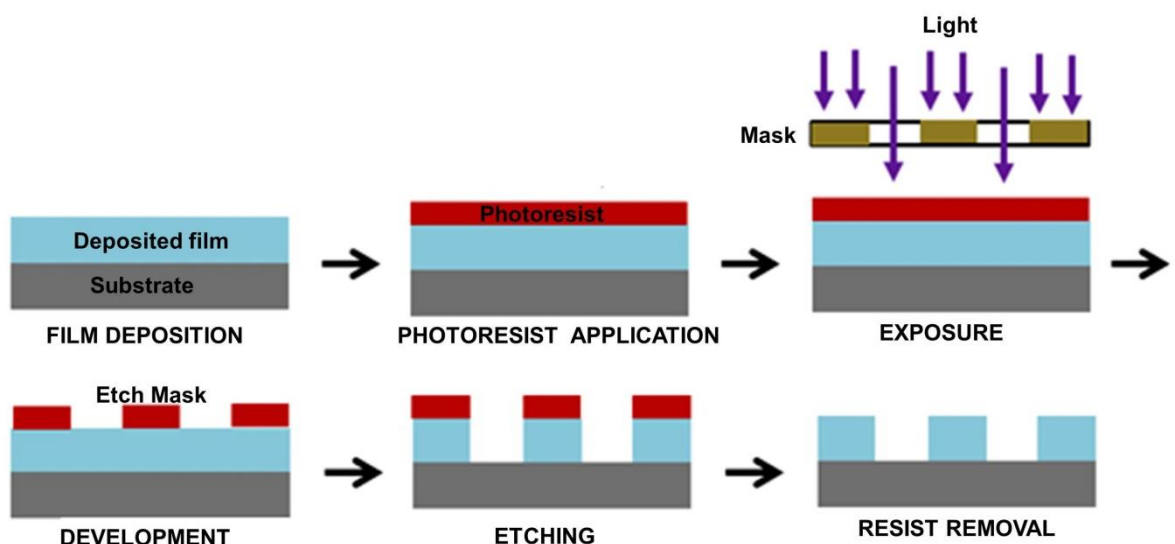
Figure 4.4: The process of Photolithography

4.2.3. Top Contact Metallisation

10 cm zinc wire and 3 cm gold wire was kept in the alumina coated crucibles inside the thermal evaporator. The sample was placed in the Thermal evaporator and pumped to ~1x10^{-6} Torr. 5 nm of Au, 10 nm Zn and 200nm Au was deposited on the sample. The thickness was measured using thin film thickness monitor.

4.2.4. Lift off

The sample was placed in the Remover PG for 30 minutes and stirred occasionally if needed followed by thermal annealing at ~320˚C for 3 seconds.

4.2.5. Mesa etching

After the required pattern had been placed on the sample via lithography, the sample was immersed in a solution of 1:1:1 acetic acid: hydrobromic acid: potassium dichromate for 40 seconds. The sample was then rinsed in deionised water and dried using nitrogen. The remaining photoresist was finally removed by soaking the sample in acetone. Finally, the above structure was processed into circular solar cells having a ring and a spider web contact.
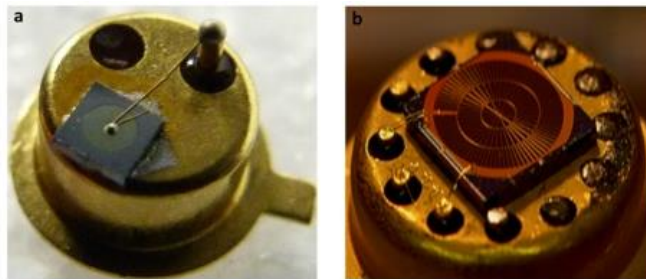
Figure 4.5: Images of the processed solar cells at Lancaster a) ring like mask design, b) spider web like mask design

4.3. Atomic force microscopy

The morphology of uncapped QDs, including their sheet density, shape and size, is characterized by atomic force microscopy (AFM). AFM has a cantilever with a sharp tip in micrometer scale size and nanometer-scale curvature to scan the sample surface. A Multimode Scanning Probe Microscope (MM-SPM) from Digital Instruments (see Figure 4.6) was used to obtain the structural information. In this system the sample is mounted on a `puck', a metal disc, and magnetically attached to the `Vertical J' piezo-actuator scanner tube beneath the probe. Rather than the probe move across the sample, in this setup, the piezo moves the sample under the probe in the x-y plane to create a raster scan of the surface. A `Vertical J' piezo-actuator scanner tube gives a large vertical range, ~5 µm, and a lateral range of 125 µm x 125 µm. The operation of MM-SPM in tapping mode was run in free air at room temperature. The tips used in the contact mode and tapping mode were Budget Sensors Tap300Al-G probes with a tip radius of <10 nm. Scan sizes range from 500 nm to 15 µm and scan rates range from 1.0 to 2.0 Hz. Sample topography is measured by tapping the surface with an oscillating cantilever at a resonance frequency of typically 300 kHz. Also contact mode in AFM operates by rastering a sharp tip (made either of silicon or Si_3N_4 attached to a low spring constant cantilever) across the sample. An extremely low force (~10^{-9} N, inter-atomic force range) is maintained on the cantilever, thereby pushing the tip against the sample as it raster's. The inter-atomic forces between the tip and the sample surface cause a measurable deflection of the cantilever. A laser beam is reflected from the top of the cantilever onto a mirror. This reflected beam is detected by a photodiode detector array or quadrant detector.

The movement of the tip on a surface can be thought as a sinusoidal wave with a fixed amplitude, thus, the laser signal on the photodiode array produces a sinusoidal

electrical signal. When topographical height of the sample is changed (indicative of material. change), phase and amplitude of the signal change. The piezo accommodates for this by adjusting the height of the sample puck so that the set point amplitude is reached. A height image is produced from the piezo movement (as in contact mode), an amplitude image from the amplitude, and a phase image from the change in phase.
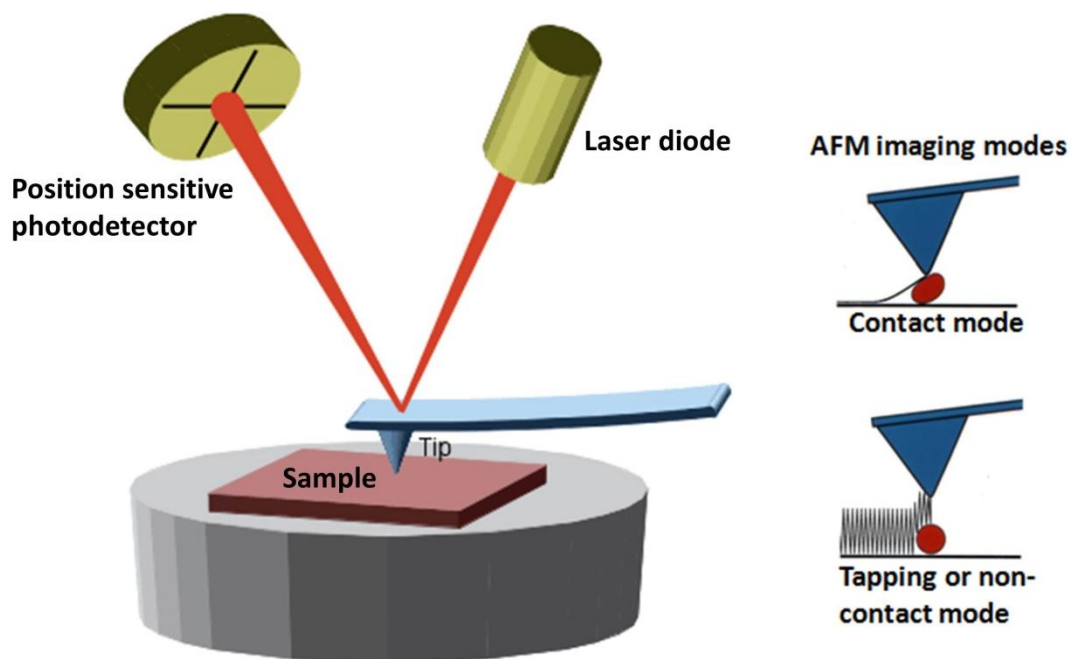
Figure 4.6: A schematic picture of Atomic force microscopy and its imaging modes [106]

The laser spot oscillates across the array as a result of the vibrating cantilever. The reflected laser beam reveals information about the vertical height of the sample surface. Either the repulsive force between the tip and sample or the actual tip deflection is recorded relative to spatial variation and then converted into an analogue image of the sample surface. The software controlling the SPM is Digital Instruments Vecco Nanoscope v4.43r8. It allows the user to control the scan size, scan rate and resolution. Windows Scanning X Microscopy (WSxM, where `x' indicates the range of microscopy modes) [107] is used for post-imaging manipulation of images and

measurement of layer thickness, as is the package, Scanning Probe Image Processer v 6.0.14 (SPIP).

4.4. Photoluminescence Spectroscopy

Photoluminescence spectroscopy is a contact-less, versatile, non-destructive method of probing the electronic structure of a material. Typically, a laser beam impinges a sample, where it is absorbed. The excess energy brought to the material can be dissipated through the emission of light, or luminescence. As the excitation of the sample is performed by light, this luminescence is called "photoluminescence".

The PL measurements were performed on all samples in the temperature range 4–300 K using a variable temperature continuous flow He cryostat. An Ar+ ion laser (514 nm, with maximum power density of 20 Wcm^{-2} at the sample) was used for excitation. The emitted radiation was analyzed using a 0.3 m (Bentham M300) monochromator and detected using-an InGaAs photodetector and digital lock-in-amplifier. However due to absorption and reflection losses in the optics only 10% reached the sample. The power was set using a Spectra Physics 2670 laser controller. A safety interlock system, plus laser goggles, was employed to prevent accidental exposure to the beam. The beam was modulated using an optical chopper, whose waveform was approximately sinusoidal. The chopper's frequency was usually set to 190 Hz; multiples of 50 Hz are noisy due to the mains supply. The beam was then directed into the cryostat using a series of mirrors and focussed to a spot size of 1 mm^2. An Oxford Instruments continuous-flow liquid helium-4 cryostat was used to cool the samples, which were held in place on a cold finger insert using thermally conductive Apezion N grease. A thermocouple was also mounted close to the sample on the cold finger to monitor the temperature. Gaseous helium was used as a heat

exchange gas within the cryostat. The liquid helium was provided by 120 litre Dewar (to allow pressure rising up to < 0.5 bar) and was pumped through the system with a Gast Manufacturing Ind. GF3 diaphragm pump via a transfer arm inserted into the cryostat. The temperature was held at the desired point using the Proportional-Integral-Derivative (PID) function of an Oxford DTC2 temperature controller. The outer jacket of the cryostat was continuously pumped by an Edwards's rotary pump during the course of the experiment to produce a vacuum of around 0.1 Torr. With this system, temperatures down to 4 K were routinely achievable. Three calcium fluoride (CaF_2) lenses were used to collimate the emitted radiation from the sample and channel it into a Bentham M300 monochromator, which had a focal length of 300 mm. A narrower slit on the entrance gave higher resolution, though a lower intensity. Internal baffles were used in order to reduce stray light, and the diffraction grating was blazed to a particular wavelength by adjusting the shape of the grooves in order to optimise it. The specific grating used featured 300 lines / mm and was blazed at 3.5 μm. The angle of the diffraction grating was automatically controlled using a Bentham PMC3B controller connected to a computer. A filter which was transparent to mid-infrared was used to block unwanted reflections of laser light from entering the monochromator, and an internal filter wheel removed higher order artefacts. Bentham indium gallium arsenide (InGaAs) photo-detector placed at the exit slit of the monochromator was used to measure the spectra. A low noise preamplifier (Type 450, Brookdeal Electronics Ltd.) was used to boost the signal and the signal was measured by an 86 Stanford SR810 DSP lock-in amplifier. The lock-in amplifier was linked to the chopper controller in order to account for frequency drift.
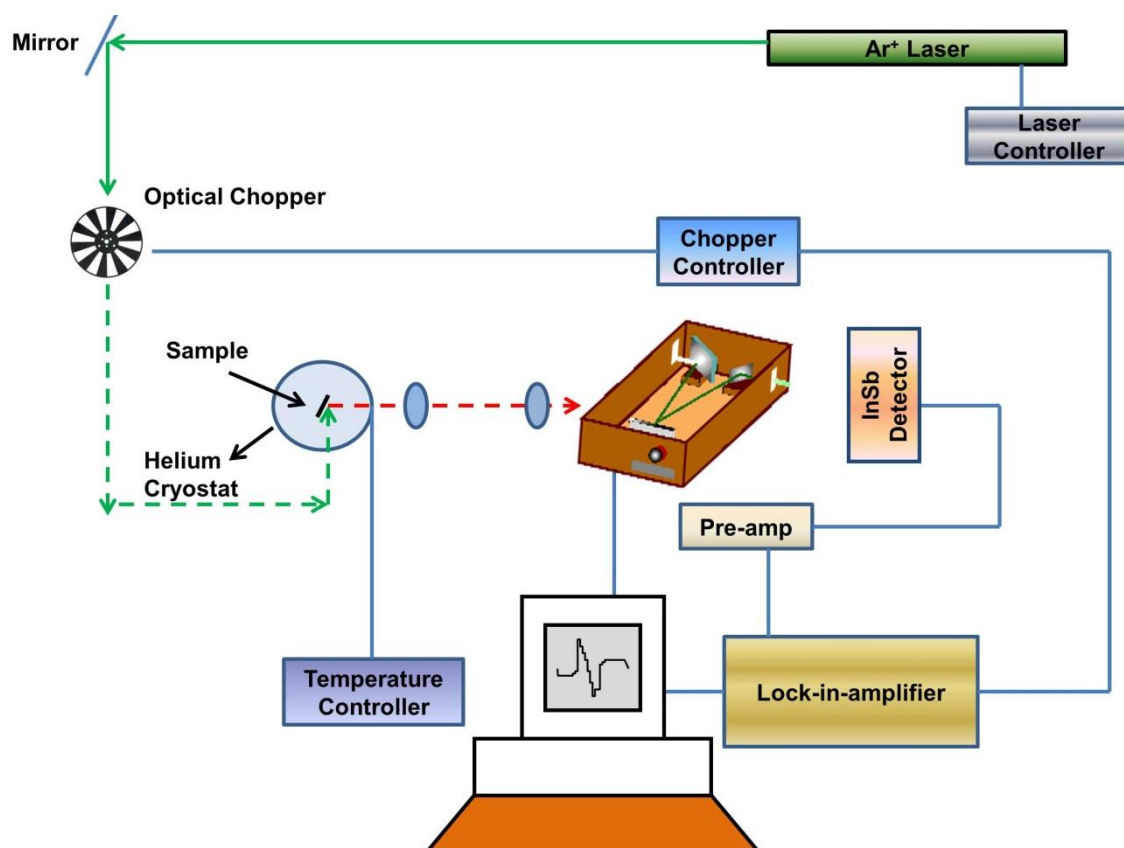
Figure 4.7: Schematic experimental set up for photoluminescence spectroscopy

The lock-in amplifier screened out signals from the photo-detector that didn't match the frequency and phase of the optical chopper, behaving similar to a band-pass filter. Both the lock-in amplifier and the monochromator were connected to a computer running Microsoft Windows XP Professional using a General Purpose Interface Bus (GPIB) IEEE-488 interface, where ranges for the monochromator to scan could be set and readings were logged using Lab VIEW based software. The spectra were then analysed using Origin 8.

The temperature dependence of the PL integrated intensity can be represented by the equation [108]

$$I_{PL}(T) = \frac{I_0}{1 + A\exp(-E_a/k_B T)} \tag{4.1}$$

where T is temperature, k_B is Boltzmann constant, I_0 is the integrated PL intensity near 0 K, A is a constant, and E_a is the thermal activation energy.
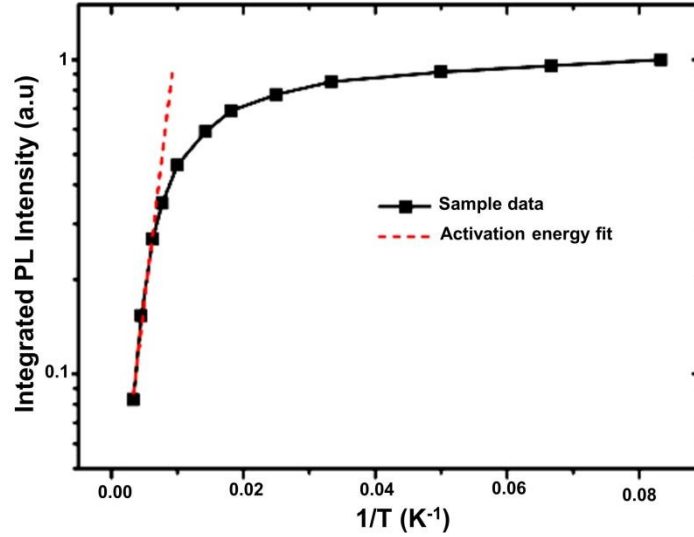
Figure 4.8: Arrhenius plots of normalized integrated PL intensities [109]

The PL intensity can be fit to the Arrhenius equation of the form

$$I_{PL} = I_0 \exp(-E_a/k_B T) \tag{4.2}$$

Where I_0 is the pre-exponential factor, E_a is the activation energy for hole escape from QRs and WL and k_B is the Boltzmann constant in eV. The above equation can be written equivalently as:

$$\ln(I_{PL}) = \ln(I_0) - \frac{E_a}{\kappa_B}(1/T) \tag{4.3}$$

Therefore the activation energy can be calculated from the slope of Arrhenius plot ie.

$$E_a = -(Slope) * k_B \tag{4.4}$$

Where k_B is the Boltzmann constant in eV.

4.5. Current-Voltage Measurements

I-V characteristics of solar cells can be used to determine the reverse current leakage, as well as the resistance at zero bias and the series resistance of the device from the gradient. A diagram of the I-V apparatus used is shown in figure 4.9, which is an overhead plan view. To measure the I-Vs in the dark, the device of interest was connected to the terminals of a Keithley 2400 Source Meter. It is a basic source-measurement unit, allowing measurements to be taken in the range between 80 pA to 1 A approximately. The use of the Keithley 2400 system is motivated by its short integration time – providing good accuracy when set at 1 power line cycle (PLC), i.e. 20 ms. The LabVIEW software was used to scan over different voltages and all measurements were recorded automatically. The scans were typically current limited (200 mA) to avoid damage of the device and the voltage range was set to -1.0 to + 1.5 V, with a delay of 100 ms between data points (200 scan point). Larger devices can handle a larger amount of current, though in some cases the limiting factor is the small gold bonding wire (50 μm).
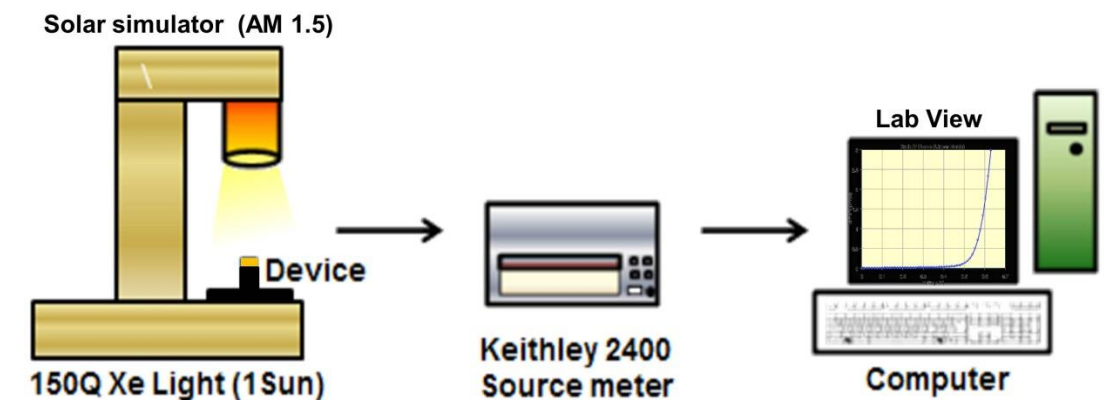
Figure 4.9: Schematic experimental set up for I-V measurement

Temperature dependant I-V measurements were done by placing the device in a cryostat controlled by temperature controller. Temperature dependent measurements

were conducted by first lowering the temperature to 100 K and letting the cell stabilize

for 1 hour. After each measurement, the temperature was raised to the next

temperature and allowed to stabilize for 5 minutes once the new temperature was

reached before taking the next measurement.
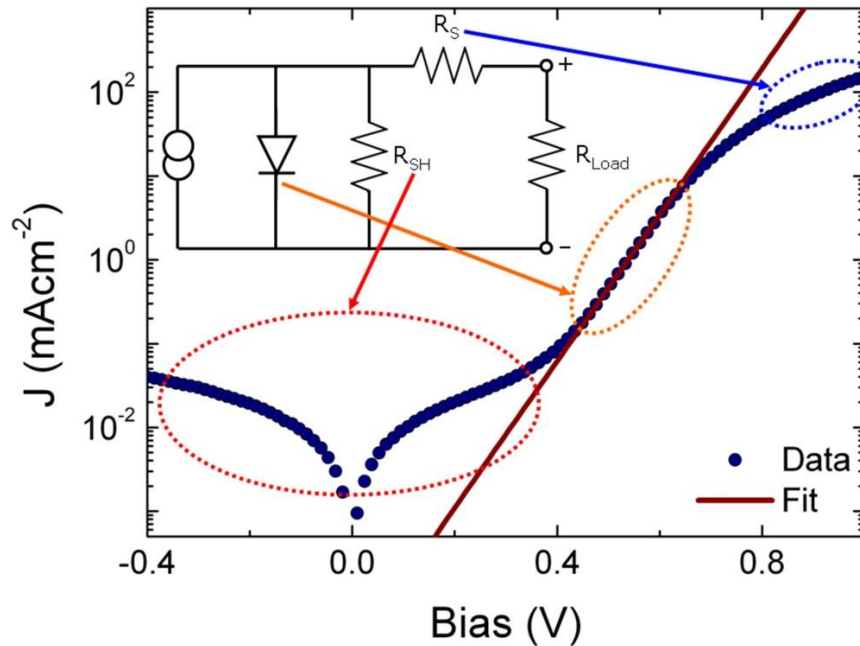
Figure 4.10: Dark JV curve showing the effect of resistances [110]. At low positive and negative

biases the current is limited by $R_{sh,}$ giving a linear response. At intermediate biases the current is

controlled by the diode, producing an exponential response. At high biases the current is limited by $R_{s,}$

yielding a linear response. Equation (2.6) is a fit to the diode portion on the curve to determine n and J_0.

For the photo current measurements, light produced by solar simulator, LS0160 150W

Xe Light Source and Manufacturer is LOT Oriel. Xe light source current rated was 7.5

Amps to maintain the 1 sun intensity (AM 1.5). Also the solar cell surface to light

source working distance was 8-10 cm for maximize the light intensity ~ 100 mW/cm2.

The scans were performed with the voltage range 0.0 to 0.8 V and current limited by

200 mA. But for the GaAs control cells scans voltage range was 0 to 1.1 V. Both

experiments (dark and light) were performed at room temperature rather than low

temperature so that the dopant atoms are mostly already excited. The measurement should be performed in a non-equilibrium situation.

The readings could also be affected if the light from the microscope above the sample is excessively bright. To determine the ideality factor and reverse saturation current, the diode equation (equation (2.6) is fitted to the diode portion of the dark IV curve. Figure 4.10 shows a sample dark IV curve where the effects of resistances are noticeable (assuming R_{sh} is much larger than R_s).

4.6. Photoresponse Measurements

The spectral response measurements were performed under a 100 W tungsten-halogen light source through a 1/4 metre (distance between the slit and image of grating) monochromator. Figure 4.11 depicts the setup of the spectral response measurement system for a solar cell. The lamp was allowed at least half an hour to warm up before any measurements were taken which is long enough to produce a stable current output from a solar cell. The device was mounted on the sample holder at a distance of 30 cm from the output slit of the monochromator after which a beam was modulated using an optical chopper where its frequency was set to 185 Hz. The beam was then directed into the device's front surface of the sample using a series of lenses that were focused to 1 cm^2. A lens was used to focus the light from the monochromator onto the cell, with the current output of the cell monitored during alignment, to ensure optimum positioning. A custom built LabVIEW program was used to run the monochromator and record the results. In order to measure the accurate spectral response, it is necessary to measure the reference device's spectral response, the Si diode and the InGaAs detector. Therefore it was obligatory to measure the spectral responses of the Si photodiode and the InGaAs detector. The measured output current was adjusted for

detector spectral sensitivity (data obtained from the manufacturer) before calculating

the number of output photons per second at each wavelength.
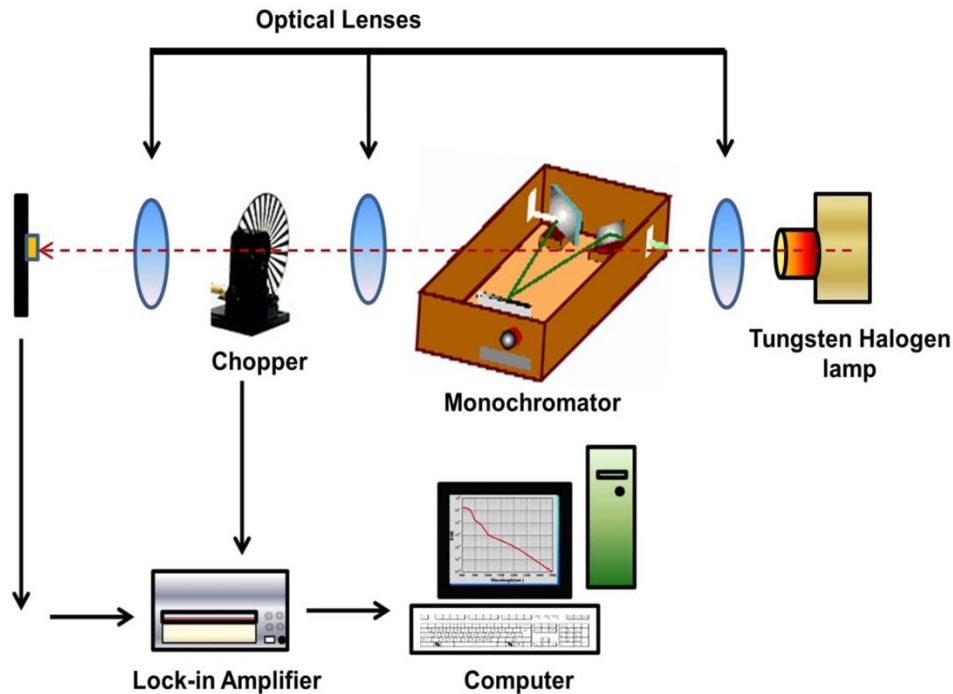
Figure 4.11: Schematic experimental set up for photoresponse spectroscopy

Furthermore, it is inherently necessary to optimise the signal sensitivity of the lock-in-

amplifier during the range of spectral response measurements. The spectroscopy is set

at a resolution of $\Delta\lambda = 5$ nm/point and time between 3000 monochromator steps, as

defined by the TMC 300 Mono program software. This pause ensures that the system

has settled at the wavelength. For bias dependence measurements, voltage was applied

to a solar cell whilst spectral response measurements were being performed. This

technique is helpful to determine how different electric fields in the device affect the

current output. For these measurements, the Keithley 2400 system was used for I-V

measurements. The external quantum efficiency is calculated using the equation:

$$EQE == \frac{I/q}{P_{ph}/E_{ph}}$$

(4.5)

where I, q, P_{ph} and E_{ph} are current, charge of one electron, total power of photons and energy of one photon respectively.

4.7. Photocurrent measurements by Direct Excitation of QDs

To measure the I-Vs, the device of interest was connected to the terminals of a Keithley 2400LV Source meter and LabVIEW software was used to scan over different voltages. The scans were typically current limited to avoid damage of the device. An infrared laser (1064 nm) where the photon energy was conveniently chosen below the bandgap of the GaAs matrix was used to directly excite the quantum dots. Two probe method was used to measure the photocurrent of QDs at room temperature. The infrared laser beam was launched into a monomode fibre and a small area of the device was illuminated. The Area of the device $\sim 7.54 \times 10^{-3}$ cm^2 and the Laser spot diameter ~0.18 mm. The solar cell device was placed on a gold plated chuck, which was mounted on an x-y stage that can be translated manually. Two 6-slot filter wheels were used to hold the specific neutral density filters and the excitation intensities of the laser beam were changed. For temperature dependent measurements, the devices were mounted in a variable temperature cryostat (77–300 K) and illuminated using a 1064 nm laser. The laser was focused to a spot size of 1 mm in diameter on the sample thus producing a maximum incident power density of ~2.6 Wcm^{-2} on the solar cell. Neutral density filters were used to attenuate the incident power for the power dependent measurements.

The photocurrent was measured by using a Keithley 2400 source-measure unit (SMU) which provided constant current and simultaneously measured the voltage on the device.
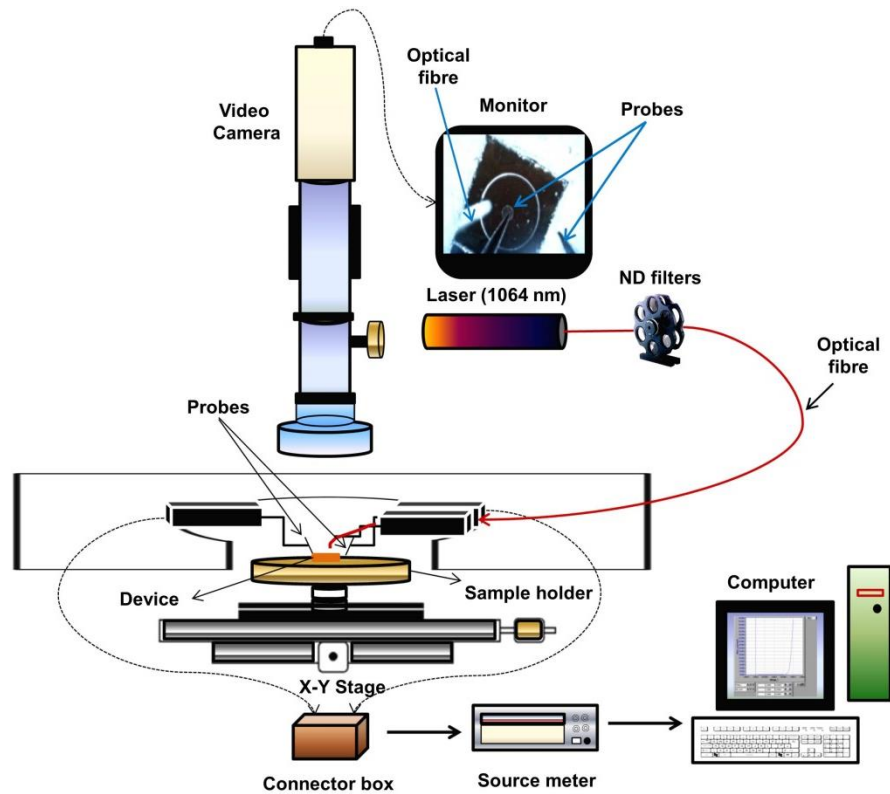
Figure 4.12: Schematic experimental set up for direct excitation of QDs by two probe method

4.8. Capacitance-Voltage Measurements

The standard tool to analyse the electronic properties of a semiconductor device and nanostructures is capacitance-voltage (C-V) spectroscopy. This can be used to investigate the electronic properties of quantum dots. C-V measurements were used to identify the biases at which charge accumulation and charge release occurred in quantum dot states. The application of an external voltage to a diode can increase or decrease the width of the depletion region which forms around the type junction. The change in the depletion width can be characterised through the measurement of the junction capacitance (C) as a function of the applied voltage (V).

The C-V curves are measured using an Agilent E4980A LCR meter with frequency range of 20 Hz to 2 MHz and 4-digit resolution output. Samples were kept with the set up as shown in the figure 4.12 in the dark under ambient conditions. A test signal level

of 25 mV and frequency of 1 MHz were used. The meter was first corrected for the

open circuit condition by probing the lower contact only. During sweeps, phase angles

were monitored to ensure that the data collected was valid, through verification that

the phase angle is around -90 °, i.e. the

device under test (DUT) is behaving as a capacitor. Measurements were further

routinely verified by taking results for various device diameters, which should scale

with the device area, and at different frequencies. The Capacitance was measured

across a series of applied biases from -1V to +1V. A LabVIEW program was used to

control measurements, record readings and calculate capacitance.

Chapter 5

Carrier dynamics of GaSb QRs (Results and discussion – I)

This chapter discusses the solar cell characteristics and the detailed behaviour of the photo-generated carriers in relation to the GaSb QRs by investigation of the optical and electrical properties at different temperatures and under different illumination conditions. Specifically, the carrier dynamics and extraction mechanisms occurring in the GaSb QRs are investigated using photoluminescence spectroscopy and current voltage characteristics as well as by direct laser excitation (1064 nm). The effects of positioning the QRs in different regions of the solar cell are also considered.

5.1. Photoluminescence spectroscopy

The management of carriers in the quantum rings is important for the successful performance of the solar cell. It is necessary for carriers generated in the QR states to fully escape into the conduction band for proper collection. Therefore it is of interest to investigate the activation energy of the quantum rings for carrier escape by photoluminescence measurements. Photoluminescence can be studied at room temperature, however at low temperatures; spectral lines become sharper and stronger, allowing more structure to be revealed. Also excitations normally masked by the high thermal phonon background at room temperature become observable at low temperatures. As discussed in Chapter 4, Photoluminescence (PL) measurements were performed using the 514.5 nm line of an Ar+ laser as the excitation source. Fig. 5.1 shows the 4 K PL spectra from a sample containing 10 stacked layers of 2.1 ML of GaSb QRs. A wetting layer peak at 1.34- 1.38 eV and a QR peak at 0.97 eV has been

reported previously at Lancaster [61]. In this case two peaks can be clearly identified; the wetting layer peak at 1.32eV and a peak at 1.05 eV for the stacked QRs. Figure 5.2 shows the corresponding band diagram with transition energies.
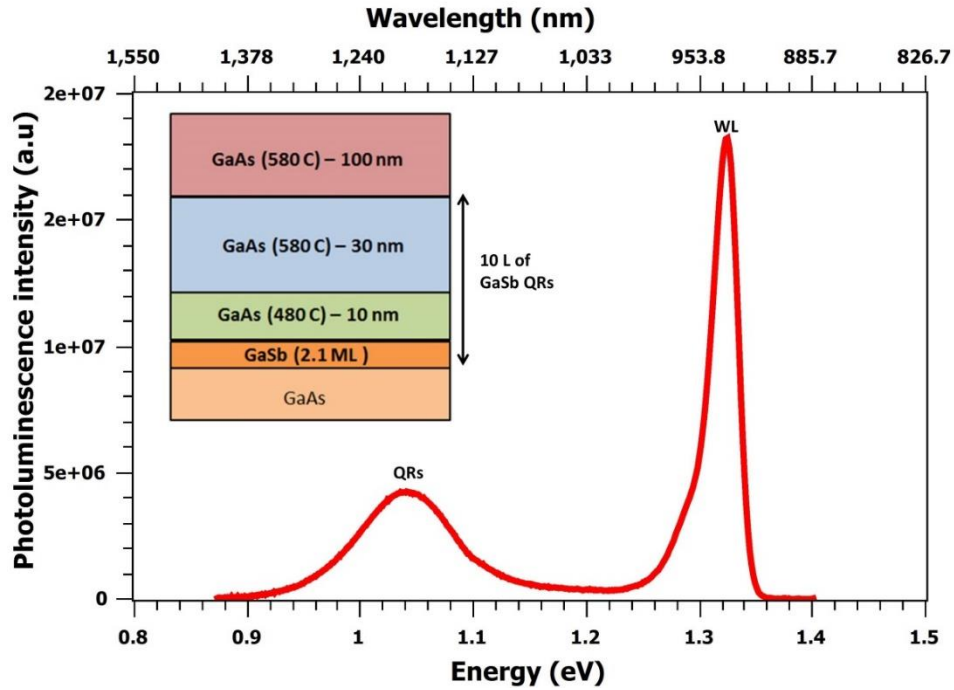
Figure 5.1: Photoluminescence spectra of the GaSb/GaAs QR structure at 4 K. The inset shows the sample structure
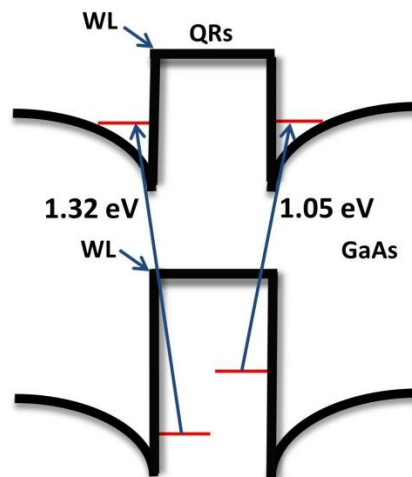
Figure 5.2: Band diagram for the GaSb/GaAs QR system illustrating the transition energies

The QRs studied here have a smaller PL energy of 1.05 eV compared with previously reported values of 1.24 eV [111] and 1.18 eV [112] for equal or similar temperature and excitation density. Also, the separation between QR and WL peak of 0.27 eV here is larger than the reported values of 0.11 eV [111], or 0.19 eV [113]. Both trends suggest that the QRs studied here are larger than those reported, leading to a stronger confinement within the QRs relative to the WL. The PL intensity of the WL is very high and 30–40 times higher than that of the GaSb QRs.

5.1.1. Temperature dependant Photoluminescence spectra

Temperature dependent photoluminescence measurements are performed on solar cells and are used in the study of thermal influence on device performance as well as carrier dynamics. Temperature-dependent PL intensity curves of the solar cell samples under excitation are presented in Fig. 5.3.
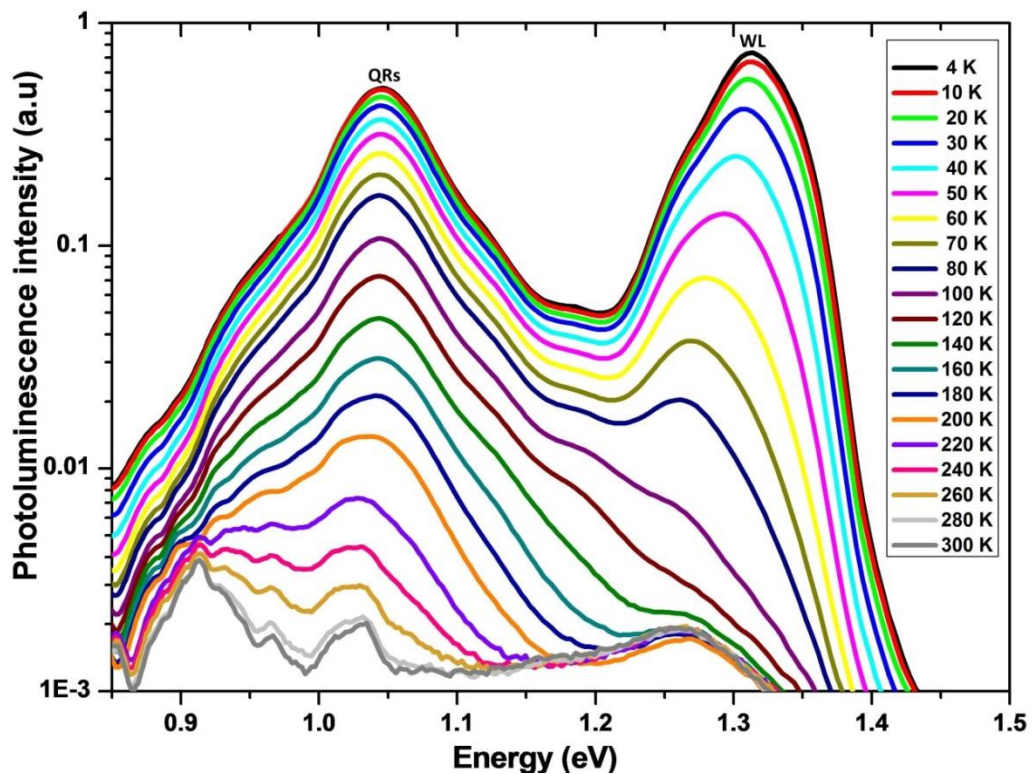
Figure 5.3: Temperature dependent photoluminescence spectra of GaSb/GaAs QR structure

Well defined peaks are observed at low temperatures for the WL and QRs but as the temperature increases the photoluminescence intensity starts quenching. The small distorted peaks at higher temperatures are due to elevated non-radiative recombination. That is, strong increase of electron - phonon interaction increases at room temperature. This leads to broadening of the photoluminescence bands and the overlapping of bands with close energies. Therefore, it is difficult to analyze the structure of the photoluminescence spectra at room temperature. Some carriers would be captured by the non-radiative centres, leading to a decrease in PL intensity. The wetting layer peak shows a large shift compared to the QR peaks and quenches with increasing temperature leading to a room temperature spectrum dominated only by the QR emission. The WL peak that virtually disappears at 100 K is again visible in the 140 K spectrum. This effect can be explained in terms of peak energies as function of temperature (figure 5.4). By fitting the PL spectra with a Gaussian peak, the emission peak energies and emission intensities are determined.
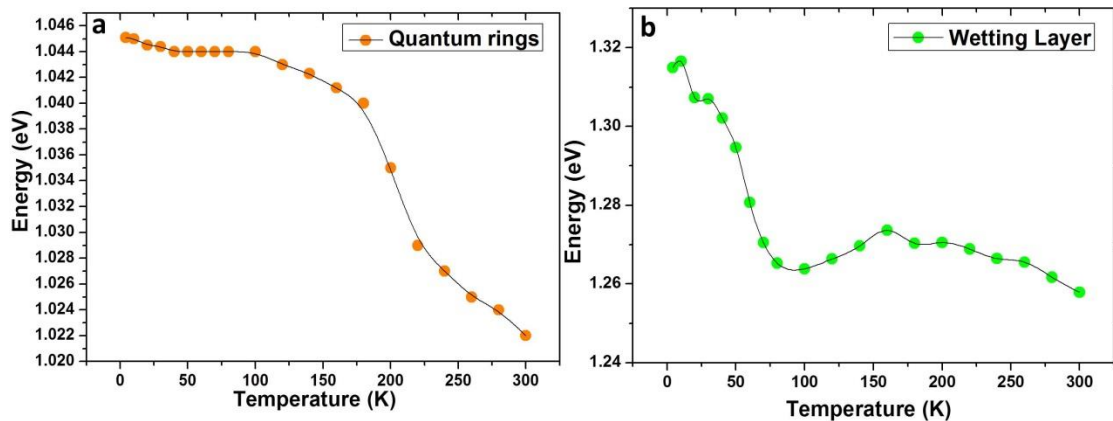
Figure 5.4: Temperature dependence of emission peak energies a) QR peak energy as a function of temperature b) wetting layer peak energy showing S shape behaviour as a function of temperature – The drawn lines are only guide to the eye

The QRs peak energy is almost constant up to 100 K and starts to decrease at higher temperature, as shown in figure 5.4a. This suggests the effective suppression of the non-

radiative processes and strong carrier confinement effect of the QRs at low temperature [114]. This behaviour is also comparable with the result observed by Takuya Kawazu et al, [115]. The potential distribution of the QRs describing possible processes of carrier transport, relaxation and recombination is shown in figure 5.5 The characteristic S-shaped behaviour of the WL peak energy (figure 5.4 b) with increasing temperature indicates the prominent carrier trapping in the band tail states leading to potential fluctuations [116]. At 4 K, the distribution of carriers is random among both deep and shallow potential minima caused by potential fluctuations associated with the inhomogeneous impurities or local defects [117] with the dominant radiative recombination process. As the temperature increases from 5 to 60 K, the holes which are localized in shallow states and relax down into the deep localization leading to the large redshift of 51 meV. At temperatures above 60 K, the thermalization of the carriers becomes more significant.
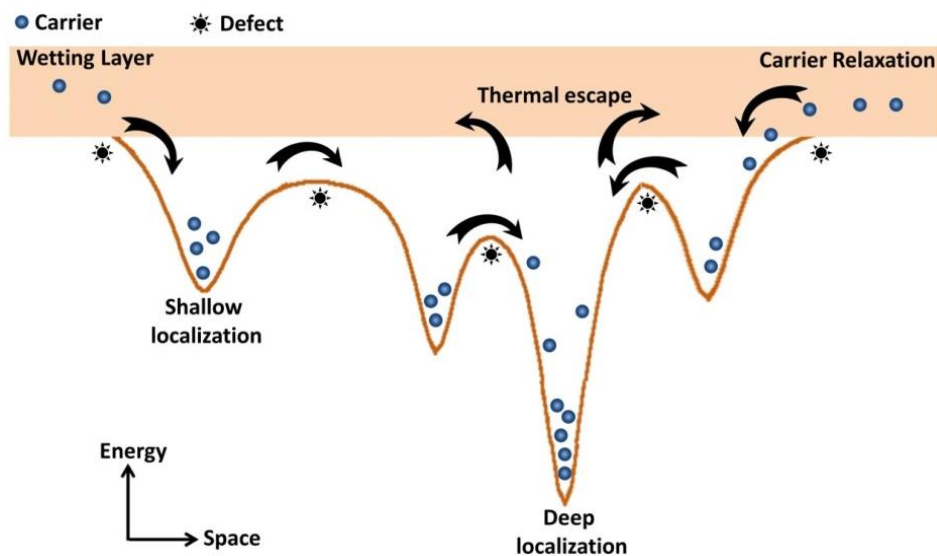
Figure 5.5: Schematic diagram of potential distribution of the non-isolated QRs describing possible processes of carrier transport, relaxation and recombination

Hence the carriers escape easily from the shallow localization and converge to fill in the deep localization centres by relaxation and recapture processes [118]. For

temperatures above 120 K, the carriers have sufficient energy to repopulate the shallow states. The non-radiative recombination then gradually dominates the recombination process, leading to a blue shift and rapid quenching of PL. A redshift of 16 meV is observed above 160 K because of temperature-induced shrinkage of bandgap. This smaller redshift observed at high temperature compared to 51 meV at low temperature indicates that some holes are trapped in the WL without being excited out [119]. Hence the presence of the wetting layer plays a major role in the carrier dynamics of GaSb/GaAs quantum dot solar cells. Also the reduction in V_{oc} which arises from a reduction in the total energy band gap is primarily due to the GaSb wetting layer near the conduction band [120].
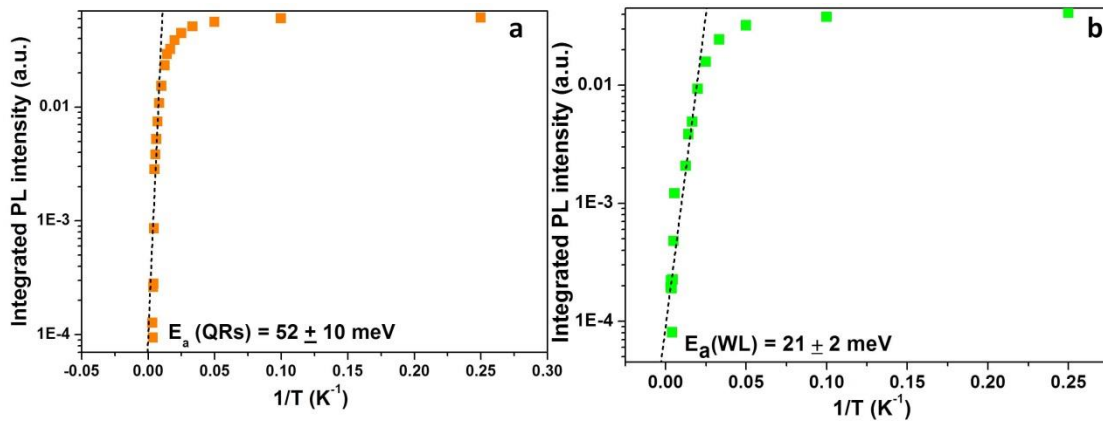
Figure 5.6: Arrhenius plots of normalized integrated PL intensities of a) QRs and b) WL. The fitting results are shown in the dashed lines.

In order to derive the activation energies of thermal quenching of PL, the temperature T dependence of the integrated PL intensity I_{PL} was fitted by the Arrhenius equation. The activation energy can be calculated from the slope of the Arrhenius plot as discussed in chapter 4. Figure 5.6 shows the Arrhenius plots for QRs and WL and the fitting results are shown as dashed lines. The activation energies of QRs and WL are calculated to be 52 ± 10 meV and 21 ± 2 meV using equation 4.3. The smaller activation energy for the

WL suggests that QR states are the effective escape channels for carriers confined in the WL.

The obtained value for the activation energy is somewhat lower than the hole localization energy in GaSb/GaAs quantum rings [121]. However, a similar value (65.7 meV) is reported in heavily charged GaSb/GaAs quantum rings with the coulomb charging effect being considered [122]. Using equation 3.3 and 3.4, the number of holes in the QRs in this case is calculated to be 8 holes/ring.

5.1.2. Power dependent Photoluminescence

Figure 5.7 shows the photoluminescence spectra of GaSb QRs measured at different excitation densities between 0.007– 670 mW at 4 K.
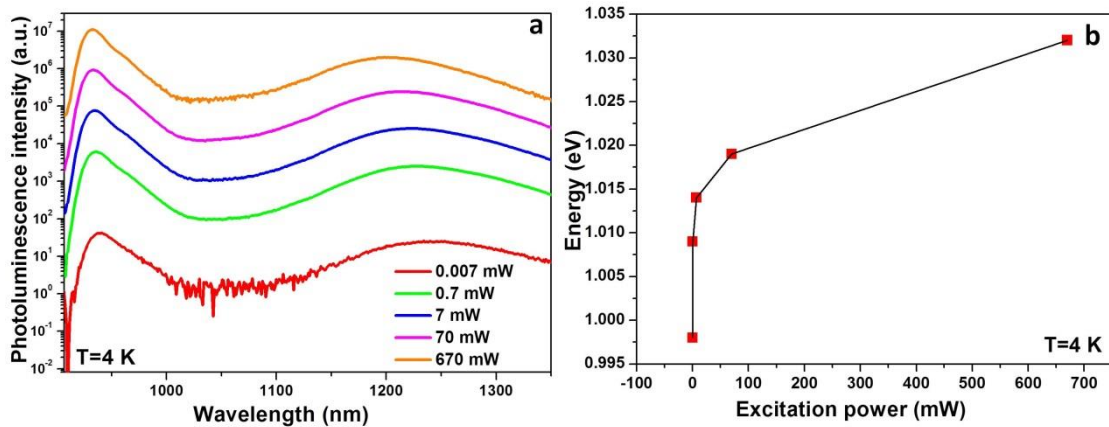
Figure 5.7: Power dependent PL spectra at 4 K a) QR and WL PL intensity at different excitation powers b) QR Peak energy showing blue shift as a function of excitation power (the power levels relate to laser output power)

As the power is increased, a slight blue shift of PL peak position appears due to the band filling effect in type II QRs [119]. For high excitation intensity (P = 670 mW), the carrier concentration is much higher and hence the majority of photo-generated carriers are trapped in deep localization states leading to band filling. For low excitation

intensity (P=0.007 mW) the carrier density is much lower leading to a decrease in the photoluminescence intensity.

5.2. Current voltage characteristics using AM1.5

Temperature dependent behaviour is described below, but first it is useful to note that the current – voltage (IV) characteristics of p-i-n solar cells (Lancaster processed) with 5 or 10 layers of Quantum rings and the GaAs control device were reported at Lancaster under 1 sun illumination using a 150 W Oriel solar simulator [74]. The area of the devices is 7.54×10^{-3} cm^{-2} with ring like mask design. A Keithley 2400 source meter was used to measure the IV curves of the samples. In this experiment voltage was used as the source and the current was measured. The solar cells containing 5 and 10 QR layers exhibit a lower open circuit voltage of V_{oc} ~0.6V compared with V_{oc} ~0.95V in the GaAs control cell without Quantum rings (Refer Fig 3.7 b.).The increase in photocurrent for 10 layer QRs is accompanied by a small decrease in V_{oc} compared to 5 layer QRs but with an increase in J_{sc}. The increase in the short circuit current is due to the absorption of extended wavelength photons by quantum rings.
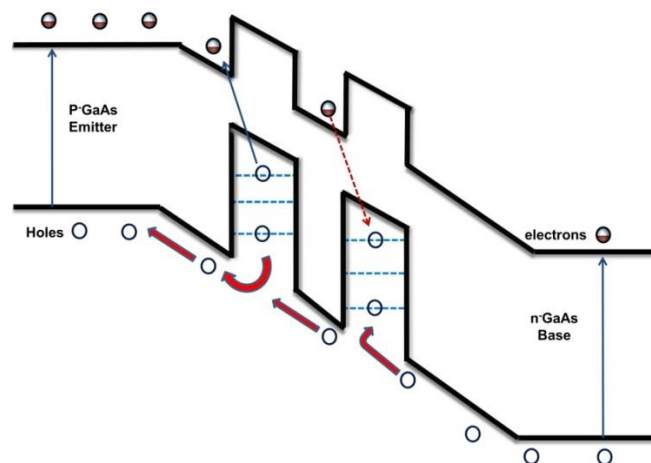
Figure 5.8: Schematic representation of band diagram of GaSb/GaAs structure showing drifting of holes from the base region

The photo-generated minority holes from the base region undergo drift across the depletion region and are captured by the QRs (thereby reducing the short-circuit current. These trapped holes then act as recombination centres, decreasing the open-circuit voltage. Figure 5.8 shows the schematic representation of the holes drift from the base region when the quantum rings are placed in the depletion region.

5.2.1.   Temperature dependent current-voltage characteristics using AM1.5

Temperature dependent I-V measurements were done by placing the device (Sheffield processed) inside a variable temperature cryostat capable of cooling to 80 K. (The area of the device is 0.096 cm^2 with spider web like mask design.) Solar cells are sensitive to temperature. Increases in temperature reduce the band gap of a semiconductor, thereby affecting the solar cell parameters viz., short circuit current density (Jsc), open circuit voltage (V_{oc}), fill factor (FF), efficiency (η) and hence the performance of solar cells [123]. As shown in figure Fig 5.9. I_{SC} increases slightly, while V_{OC} decreases more significantly.
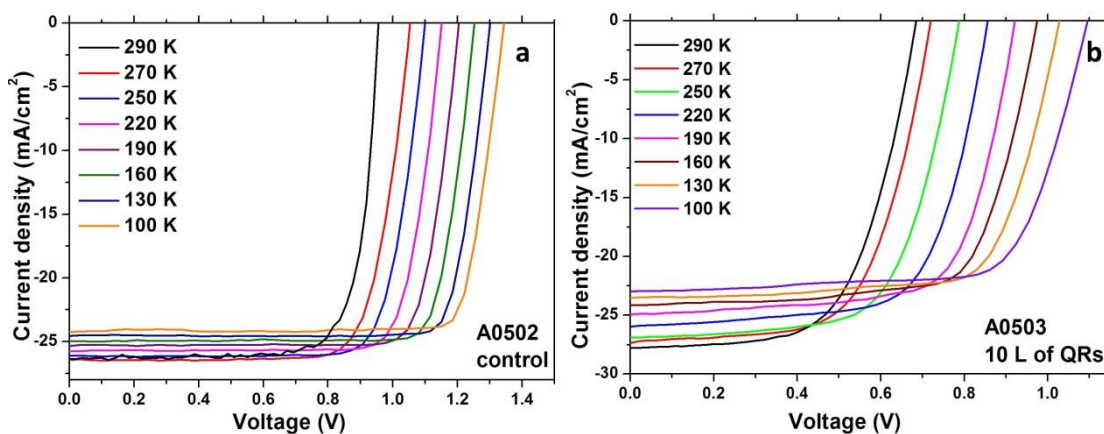
Fig 5.9: Current density- voltage curves for the GaAs control and GaSb/GaAs QR solar cells obtained using 1 sun AM 1.5 illumination at different temperatures

A small variation of short circuit current density (J_{SC}) with temperature is primarily due to the change in bandgap energy with temperature. As the cell heats up, the bandgap decreases, and hence the cell responds to longer wavelength portions of the spectrum, and therefore the short circuit current actually increases with temperature. Hence, the J_{SC} variation term is roughly proportional to the incident spectral intensity at wavelengths near the band edge [124]. Figure 5.10 shows a summary of the temperature dependence of the representative solar cell characteristics under 1 sun concentration, that is, short-circuit current density (J_{SC}), open-circuit voltage (V_{OC}), fill factor (FF) and efficiency. Both the QR sample and the control sample show a constant increase of J_{SC} with increasing temperature, resulting from the increased photo-absorption associated with the GaAs bandgap narrowing.
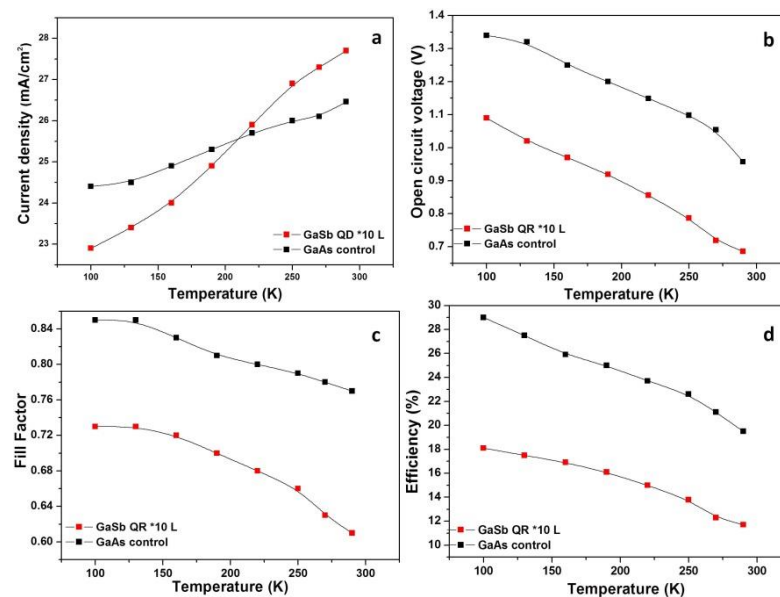
Figure 5.10: Temperature dependence of the representative solar cell characteristics for the GaAs control and GaSb quantum ring (QR) cells under a solar concentration equivalent to 1 sun; (a) J_{SC}, b)V_{OC}, c)FF and d) efficiency (-error bars lie within the thickness of the points).

At low temperature (100 K), J_{SC} for the GaSb QR cell is much lower than that of the GaAs control. However, J_{SC} starts to increase rapidly above 180K and surpasses the

GaAs control cell above 230 K. At the same time, V_{OC} for the GaSb QR cell shows a slight change of slope, and the FF starts to decrease rapidly above 180 K, resulting in a net reduction of the efficiency.

5.2.2.   Temperature dependent dark current-voltage characteristics

Figure 5.11 shows the temperature dependent dark J-V characteristics measured from the control and QR SCs. Both the devices do not display a steady increase in dark current with temperature. The change in the shape of the dark J-V curves with temperature depends on the concentration of different types of defects present in the sample with different temperature dependent carrier capture cross sections and tunnelling effects [125] [126].
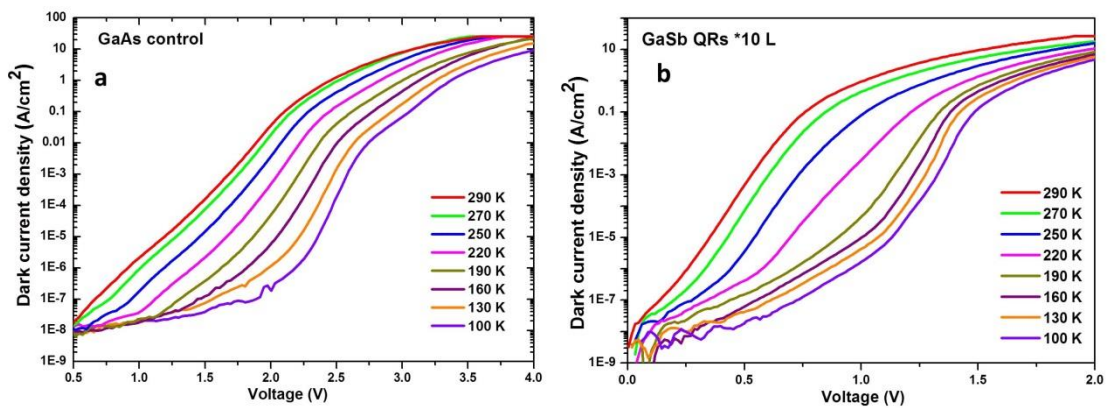
Figure 5.11: Temperature dependent dark J-V characteristics measured from the (a) GaAs control and (b) GaSb QR solar cells.

In the QR device, the presence of QRs in the depletion region introduces additional recombination paths via QR states to contribute to dark current, the amount of which largely depends on the carrier capture and recombination processes under different biases and temperatures. The temperature dependence of the ideality factors are presented in figure 5.12.
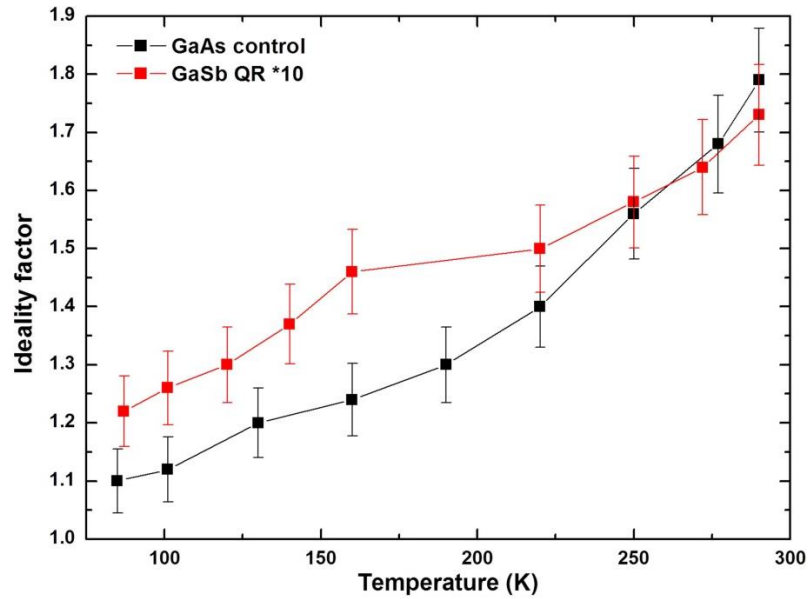
Figure 5.12: Temperature dependence of the ideality factor for (a) GaAs control and (b) GaSb QR solar cells.

At low temperatures the ideality factor is close to unity, indicating that diffusion current dominates, with the increase to 1.8 at room temperature and an increase in non-radiative recombination via trap levels in the depletion region. At low temperatures, the ideality factor of the QR SC is slightly higher than that of the control sample, but increases more slowly with temperature, reaching a similar value at room temperature. This behaviour has been observed previously in InGaAs/GaAs QD SCs [125] and was attributed to an increase in recombination of injected minority carriers with majority carriers trapped in the QDs. For the GaSb QR SCs we can assume that under forward bias, hole injection results in state filling within the QR layers close to the highly doped p-type emitter. Under these conditions, the QRs act as efficient recombination centres, capturing holes that recombine with injected minority electrons. (Also there is recombination via midgap traps in the depletion region which is characterised by an ideality factor of 2). Therefore in the QR SC, the combination of these different recombination paths gives rise to an ideality factor of 1.7.

5.3.   Current voltage characteristics using 1064 nm Laser

Figure 5.13 shows the room temperature current-voltage (I-V) characteristics under 1064 nm laser illumination obtained from single junction GaAs solar cell devices containing 5 and 10 layers of GaSb QRs in the active region.
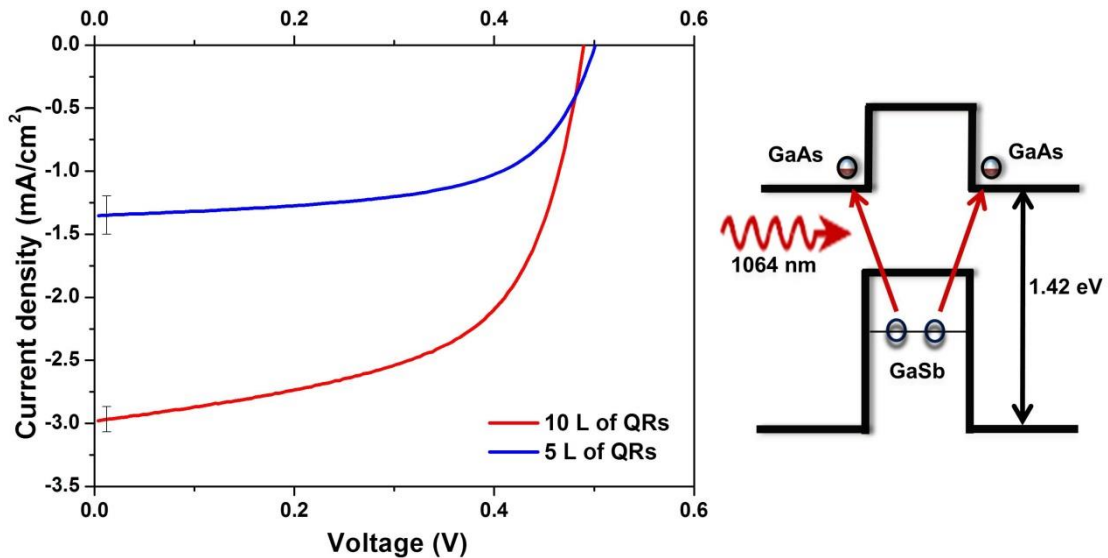
Figure 5.13: a) Photocurrent measurements from solar cells containing 5 and 10 layers of GaSb QR directly excited using a 1064nm laser (~ 2.6 Wcm^{-2}) at 300 K; b) Band diagram (strain induced band-bending is neglected here) showing direct excitation of GaSb QRs using 1064 nm Laser (error bars represent variation between 6 samples studied here)

The short-circuit current density (Jsc) obtained from the 10-layer sample is approximately twice that from the 5-layer sample. The QRs are seen to be effective at the generation of photocarriers as seen in the magnitude of Jsc although the open-circuit voltage is lower than that in a control cell (1.0 V) containing no QR. Fig. 5.14 shows the photocurrent as a function of the excitation intensity using different applied reverse bias voltages with the cell at 300 K.   The photocurrent shows a linear dependence on excitation intensity over several decades under all conditions, which indicates that there is no net accumulation of charge within the QR. Since a high density

of e-h pairs are created in the GaSb QR we can suppose that the hole escape rate from the quantum rings is faster than the recombination rate, even for the case of low laser excitation. Increasing the reverse bias, increases the internal electric field in the depletion region and decreases the hole confinement barrier in the QR.
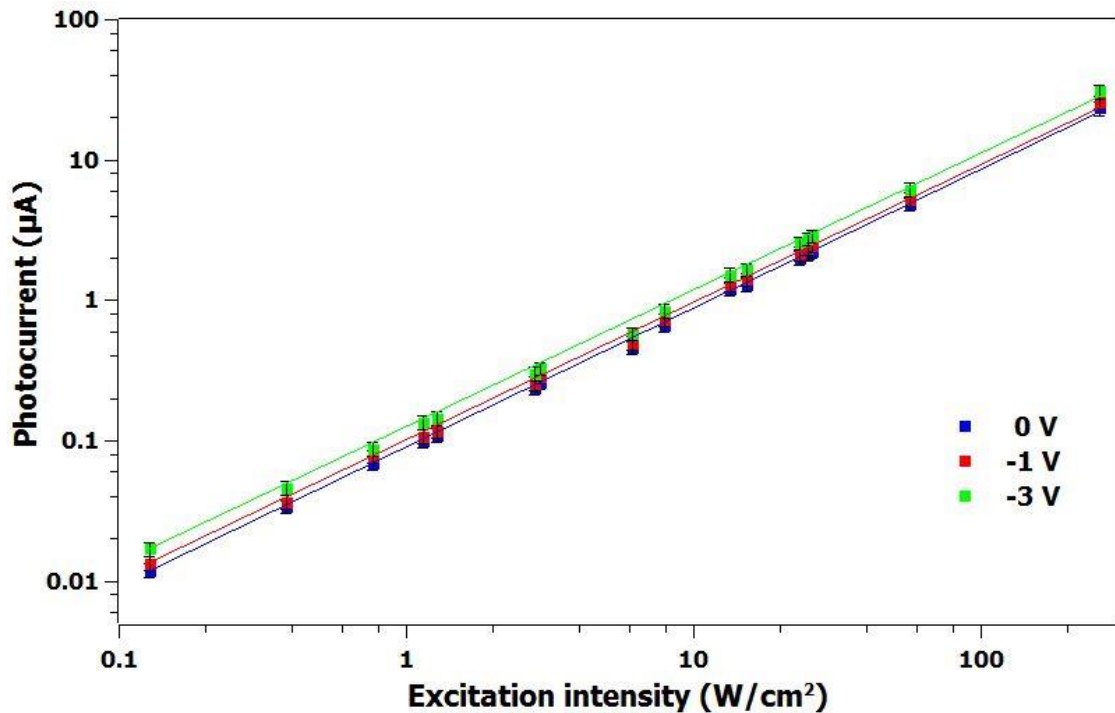
Figure 5.14: Photocurrent as a function of 1064 nm excitation intensity for different applied voltages measured at room temperature. (Solid lines are fits to the data)

This increases the tunnelling escape probability of the confined holes which would be expected to result in an increase of the photocurrent. However, this effect is masked at room temperature by the thermionic emission of holes as shown in Fig. 5.14 where there is hardly any change in photocurrent due to the applied reverse bias. The temperature dependent photocurrent measured using different laser excitation intensities and at zero bias is shown in figure 5.15.
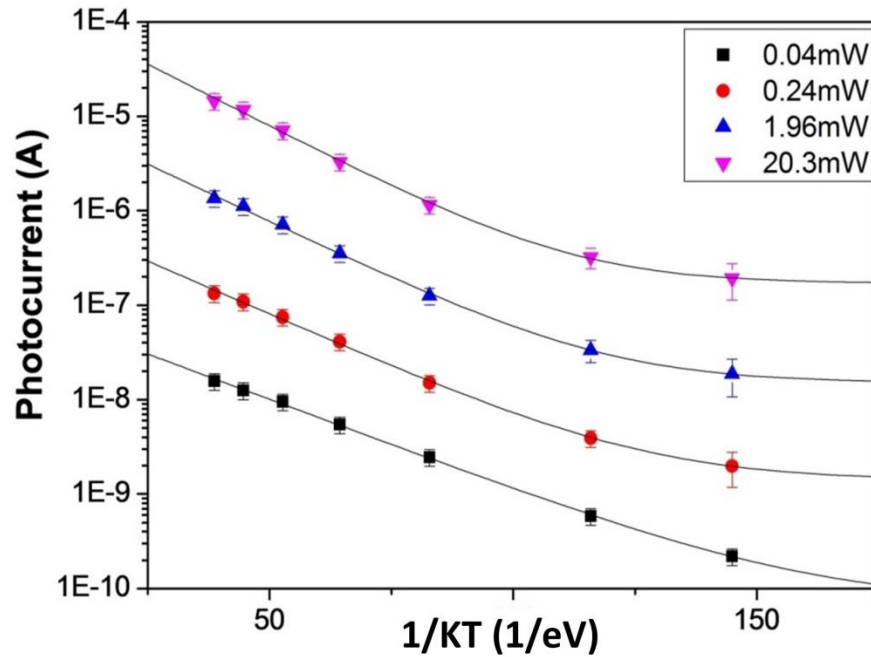
Figure 5.15: Temperature dependence of the photocurrent measured at different 1064 nm laser excitation intensities with the solar cell at zero bias.

With increasing temperature, the thermal escape rate increases and dominates over both the recombination rate and the tunnelling rate. Hence, the photocurrent from the QRs increases as shown in figure 5.14. By subtracting the temperature independent tunnel current contribution from each of the curves it is possible to extract the activation energy for thermionic emission of holes from the GaSb QR at each excitation intensity. The result is shown in figure 5.16. These values which are much lower than the hole localization energy ~ 600 meV deduced from previous DLTS and photoluminescence (PL) measurements [127] indicate significant coulomb charging of the QRs with holes. Figure 5.17 shows the reverse bias voltage dependence of the activation energy E_a. The activation energy increases from 44 to 61 meV at zero bias voltage with increasing laser intensity, although there is no significant laser intensity dependence above 0.5 V in reverse bias. Using representative values for our QR system we estimate that at the highest laser excitation intensity there can be up to 15 holes per QR using equation 3.3

and 3.4 as discussed in chapter 3. The activation energy tends to decrease if the number

of holes increases in the QRs.
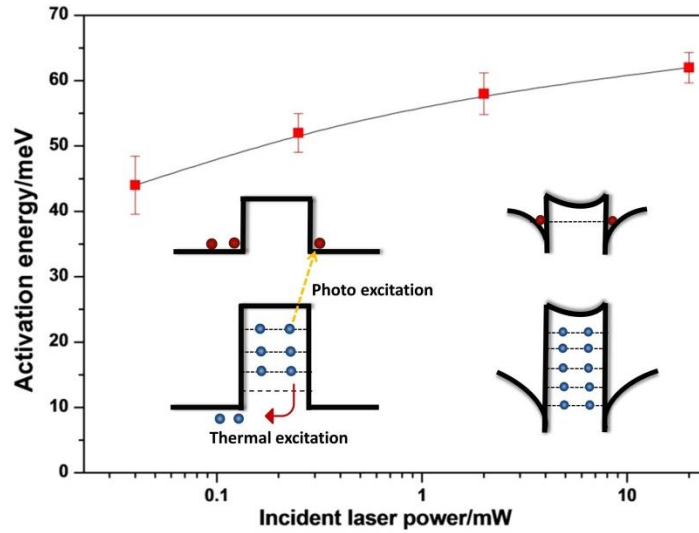
Figure 5.16: The thermal activation energy at different laser excitation intensities for thermionic emission of holes from the GaSb QRs as derived from the results in Fig. 5.14. The diagram shows the band bending produced by the charging of the QR with holes which increases the hole activation energy.
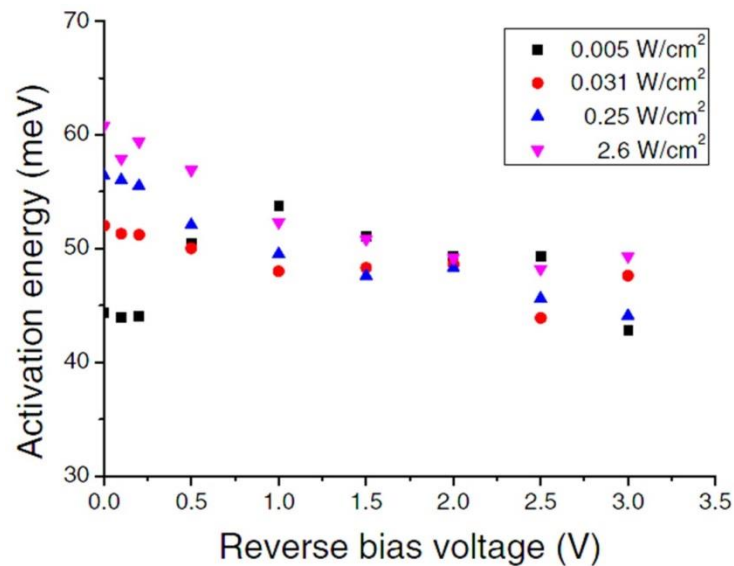
Figure 5.17: Reverse bias voltage dependence of the thermal activation energy at different excitation power density (error bars estimated from uncertainty in corresponding Arrhenius plots)

A trade-off between charging and temperature related effects should be understood here. Charging the QR with holes produces band bending which increases the potential barrier for hole escape and subsequently decreases the hole escape rate. However, this is a small effect since the change in activation energy is ~kT (300 K) and the highest activation energy obtained in our experiments was only 62 ± 5 meV i.e. ~2kT (300 K) and using a value of $E_a = 62 \pm 5$ meV, the thermal escape rate for holes can be calculated using the equation 3.5 (as discussed in chapter 3) and is shown in Fig. 5.18 for the highest laser excitation intensity (2.6Wcm^{-2}).

The escape rate increases rapidly with increasing temperature, ranging between 10^{11} to 10^{12} s^{-1} and at room temperature becomes much larger than the radiative recombination rate (~10^9 s^{-1}). Therefore, although under excitation the QR can accommodate many holes, most of these photogenerated holes should escape from the QRs before they can recombine and will contribute to the photocurrent. Therefore the infrared response is determined by the thermionic emission of holes from QRs [10].

The current–voltage characteristics revealed that the thermionic emission process produced the dominant contribution to the photocurrent and accounts for 98.9% of total photocurrent at 0 V and 300 K. Although the tunnelling process gives a relatively weak contribution to the photocurrent, this process could be enhanced by applying additional reverse bias voltage. This suggests that increasing the built-in electric field surrounding the QRs in the region of the GaAs p-i-n structure could improve the QR solar cell performance [137].

The illuminated laser intensity (2.6Wcm^{-2}) corresponds to a concentration of roughly 200 suns. This means the concentrated operation of GaSb QR solar cells could further degrade V_{OC} because of hole accumulation, unless thermal extraction can be increased [128].
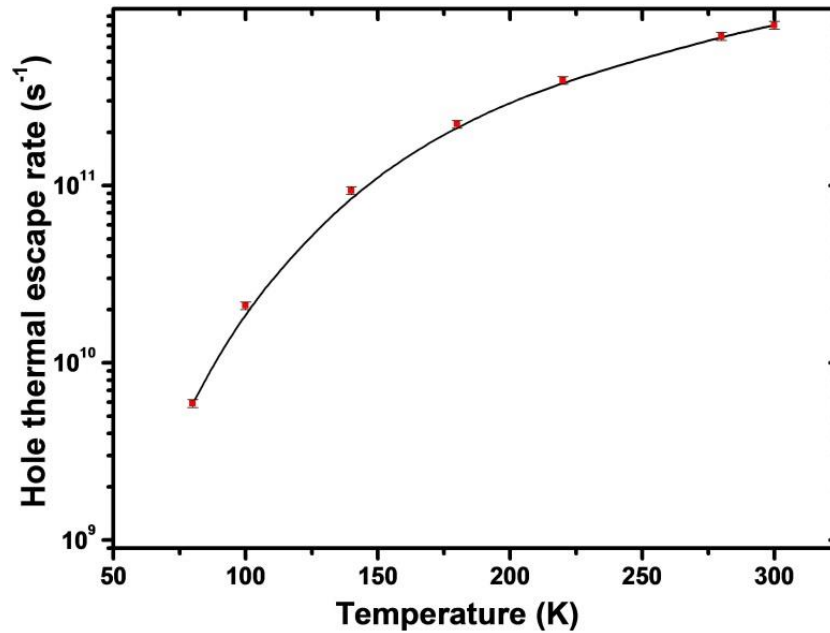
Figure 5.18: The calculated thermal escape rate for photogenerated holes in GaSb QR as a function of temperature, using direct excitation of 2.6Wcm^{-2} at 1064 nm (the solid line is a guide to the eye).

This is an important result for the development of concentrator solar cells because, in order to enhance the solar cell efficiency, a more detailed understanding of the behaviour of the photo-generated carriers is essential, especially under high solar concentration conditions under which these solar cells will be implemented.

5.4. Delta doping and positioning effects on current voltage characteristics

QR solar cells were fabricated from the epitaxial material as 2.5 mm diameter mesa etched diodes by using standard photolithography and wet etching techniques using a spider web like mask design at Lancaster Quantum Technology Centre. Figure 5.19 shows the location of the doped/undoped GaSb QRs at the different regions within the solar cell. The reduction in open circuit voltage and the influence of the location of QR layers and their delta doping within the solar cell is studied in this section.
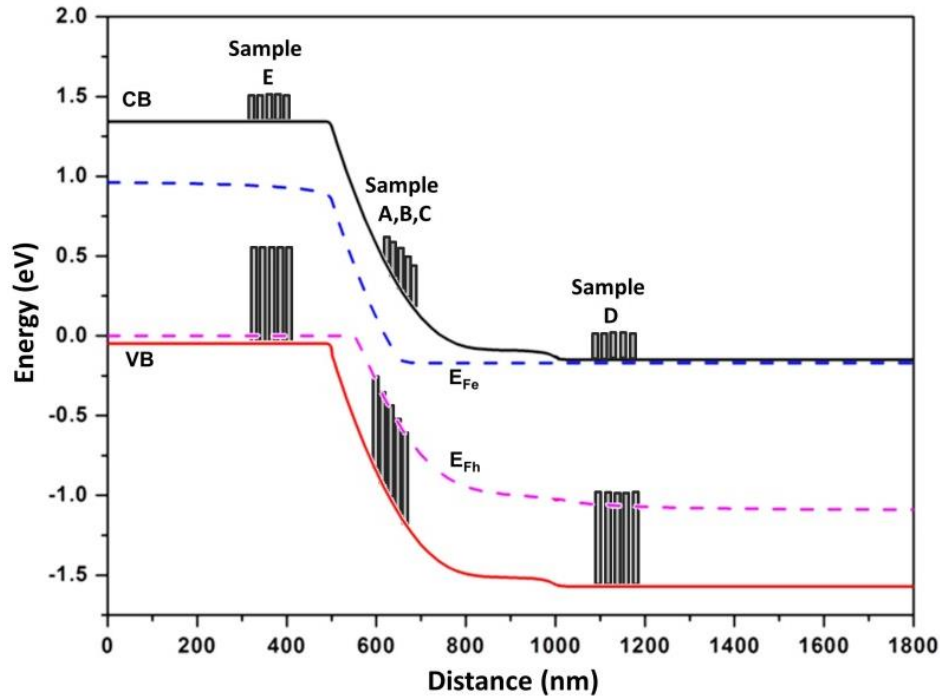
Figure 5.19: Energy band diagram showing the location of the doped/undoped GaSb QRs at the different

locations within the solar cell (band diagram shows the situation at short circuit illumination). Sample A-

undoped QRs grown in intrinsic region, Sample B- n-doped QRs grown in intrinsic region, Sample C-p-

doped QRs grown in intrinsic region, Sample D-n doped QRs grown in n-region, Sample E-p- doped QRs

grown in p-region

The solar cell structures contain 5 layers of delta doped QRs embedded in the intrinsic

(sample B and C), n doped (sample D) and p doped (sample E) regions of the GaAs p-i-

n junction, where the QRs in D and E are spatially separated from the depletion region.

Figure 5.20 shows the I-V characteristics of the quantum dot solar cells (QRSCs) and

the GaAs reference cell. The deduced values of J_{sc}, V_{oc}, Fill factor and conversion

efficiency are listed in Table 1. To begin with we consider the effect of delta doping of

QRs placed in the intrinsic region on the performance of the solar cell. The Voc of the

QR solar cell without delta doping (sample A) is 0.62 V, which is much lower than the

GaAs reference sample R. The reduction in the V_{oc} of sample A in the intrinsic region is

due to the accumulation of holes trapped within the quantum rings. The Photo-generated

minority holes from the base region undergo drift across the depletion region and are

captured by the QRs thereby reducing the short-circuit current. These trapped holes then act as recombination centres, decreasing the open-circuit voltage.
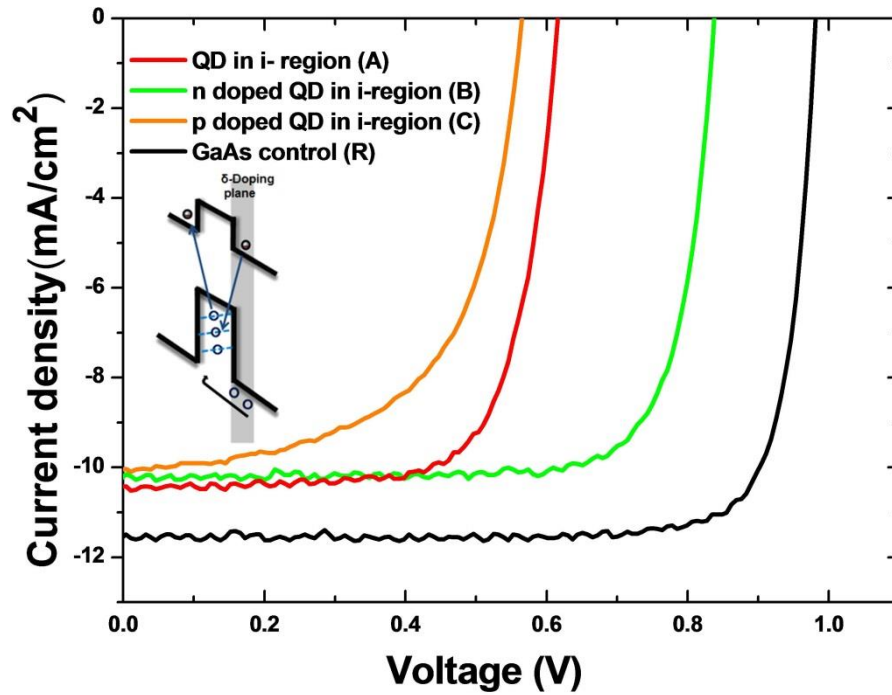
Figure 5.20: a) I-V characteristics of delta doped QRSCs in i-region

Improvements in V_{oc} are observed for n- doping of QRs (sample B) whereas the p-doping (sample C) further degraded the solar cell performance, i.e. both V_{oc} and J_{sc} are reduced.

	Sample R	Sample A	Sample B	Sample C	Sample D	Sample E
J_{sc} (mA/cm²)	11.5	10.4	10.2	10.04	10.9	11.2
V_{oc} (V)	0.98	0.62	0.84	0.56	0.86	0.89
Fill factor (%)	82	72	78	59	76	80
Efficiency (%)	9.2	4.6	6.6	3.3	7.1	8.0

Table 1: Comparison of Quantum dot solar cells to GaAs reference solar cell

The purpose of modulated n- doping is to partially fill the quantum rings with electrons to reduce recombination which helps to recover the V_{oc}. The device with p-doped QRs

placed in the intrinsic region shows the worst performance. As the intentionally doped holes are strongly localized in QRs more holes get accumulated in the QRs and recombine with electrons leading to the reduction of V_{oc}.
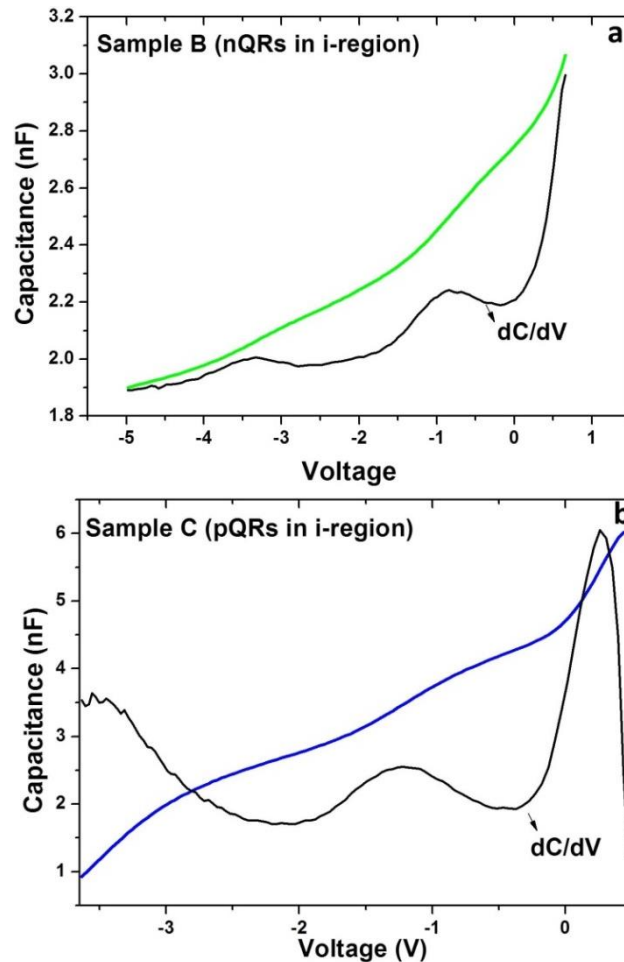
Figure 5.21: Capacitance voltage curves showing the plateau like features in the doped QR devices placed in the intrinsic region

Figure 5.21 a and b shows the C-V curve between a reverse bias of 0 and -4 V at a temperature of 300 K and a measurement frequency of 10 kHz. When the p or n delta doped QRs are placed in the intrinsic region, the charging effects are clearly seen. The C-V curves of doped QRs placed in the intrinsic region have a plateau-like feature that reflects the charge accumulation in the QR layer. The second derivative peaks of the

curve give the beginning and the end of the plateau from which the width of the plateau can be calculated.

The number of charge carriers accumulated in the QR layer can be estimated from, $Q=C_p\Delta V$ where C_p is the capacitance of the plateau region, and ΔV the width of the plateau. The number of holes per quantum dot is given by

$$Holes/QD = \frac{C_p \Delta V}{qN} \qquad\qquad (5.1)$$

Where q is the elementary charge and N is the density of the quantum rings. The number of holes per dot is estimated to be approximately 5 holes for sample B and 7 holes for sample C. For the sample B with 5 holes, the thermal activation energy is estimated to be ~112 meV.

For the sample C with 7 holes, the thermal activation energy is estimated to be 78 meV which is associated with a deeper bound state in the QRs [129]. The thermal escape rate of the holes in sample B and C are found to be $\sim 10^8$ - 10^9 s^{-1} using equation 3.5, which is less or equal to the radiative recombination rate 10^9 s^{-1}[130]. Hence, the recombination dominates most likely in the delta doped QR samples placed in the depletion region.

A trade-off is needed; i.e. to minimize the V_{oc} degradation while maximizing the short circuit current density (J_{sc}) due to sub-bandgap absorption. To achieve this, both the location and the doping of the QR layers needs to be optimised and therefore we studied the influence of the position of delta doped QRs in the n or p regions of the solar cell. Figure 5.22 shows the I-V characteristics of n and p delta doped QRs placed in the n or p regions of the solar cell. In both cases the V_{oc} of the delta doped QRs placed in n and p regions of the solar cells shows a significant recovery.
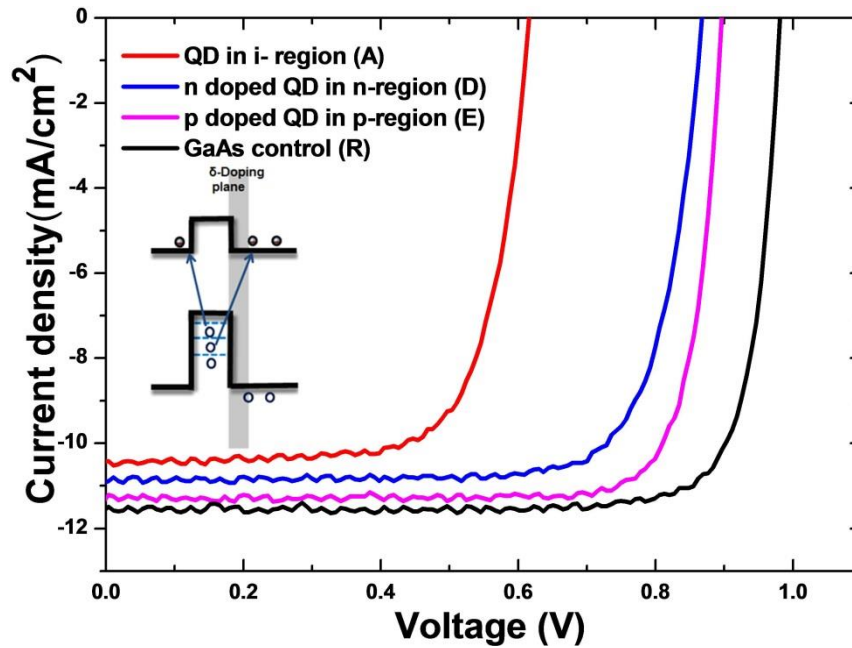
Figure 5.22: I-V characteristics of delta doped QRSCs in n or p-region

The J_{sc} and V_{oc} of Sample D (n-QRs in n-region) and Sample E (p-QRs in p-region) is greater than Sample B (n-QRs in i-region) and sample C (p-QRs in i-region) because the QRs are located in the flat band region away from the depletion region. The device with p-doped QRs placed in the flat band potential region (sample E) shows the highest conversion efficiency compared to other QR devices studied here. It has been previously shown that the n delta doping of QRs increases the low band gap absorption and also increases the conversion efficiency [131] [132]. These studies show the importance of positioning and doping of the QRs within the solar cell structure. In the device with n-delta doped QRs placed in the n region, the V_{oc} and J_{sc} is not fully recovered compared to the control cell. But, our results show that the device with n-doped QRs placed in the n-region has a higher open circuit voltage compared with n-doped QRs placed in the depletion region. The conversion efficiency could be further improved by finding an optimum doping level.

The effect of the introduction of dopants on the morphology of the GaSb QR nanostructures was analysed by HAADF-STEM at University of Cadiz [133]. The

results show the presence of well-developed GaSb QRs in both p-doped and n-doped heterostructures. However, in the undoped sample grown under the same conditions such well-developed QRs have not been observed. In the undoped GaSb/GaAs sample it is likely that QDs and small QRs coexist together. The driving force for the formation of QRs is a combination of the elastic energy and the surface energy of the system [134]. In doped structures, the introduction of a small number of different atoms produces an additional local strain that can tip the balance toward QR formation. It has been found that p-doping with Be stimulates the formation of QRs, whereas n-doping with Te results in the formation of GaSb nanocups. Therefore, the introduction of dopants in the growth of GaSb nanostructures has a significant effect on their morphology. Understanding the effect of the introduction of dopants in tailoring the opto-electronic properties of semiconductor nanostructures requires a careful analysis of their morphological characteristics, as this morphology can differ from that of undoped nanostructures.

Chapter 6

Absorption characteristics of GaSb QRs (Results and discussion - II)

This chapter discusses the absorption characteristics of GaSb QRs using the spectral response of the solar cell. External quantum efficiency (EQE) measurements are performed in order to study the enhanced infrared photo-response from GaSb/GaAs quantum ring solar cells. Bias and temperature dependent EQE measurements are performed to understand the hole extraction from the QRs. The extended Urbach tail of a QR device is analysed and the transitions in the QDs and WL are located.

6.1. The absorption of Type II GaSb QRs

Photocurrent measurements using direct excitation of the QR enable absolute values for the absorption strength (A) to be obtained using equation 3.7 given previously;

$$I = \frac{APe\lambda}{hc}$$

Where, I is the photocurrent, P is the total incident optical power of the laser at the wavelength λ and h and c have their usual meaning. A value of A=1.4x10^{-3} (or approximately 1.4x10^{-4} per layer) is calculated at a 1064 nm laser power of 2.6 Wcm^{-2} at room temperature. This is comparable to A=2x10^{-4} deduced previously for a single layer of type I InAs/GaAs QRs [135]. Despite the type II nature, the similarity may be accounted for by remembering that in type-II GaSb QR the electron is able to reside close to or within the QR itself by Coulomb attraction so that the e-h wavefunction overlap is restored and the corresponding matrix element for optical absorption is increased.
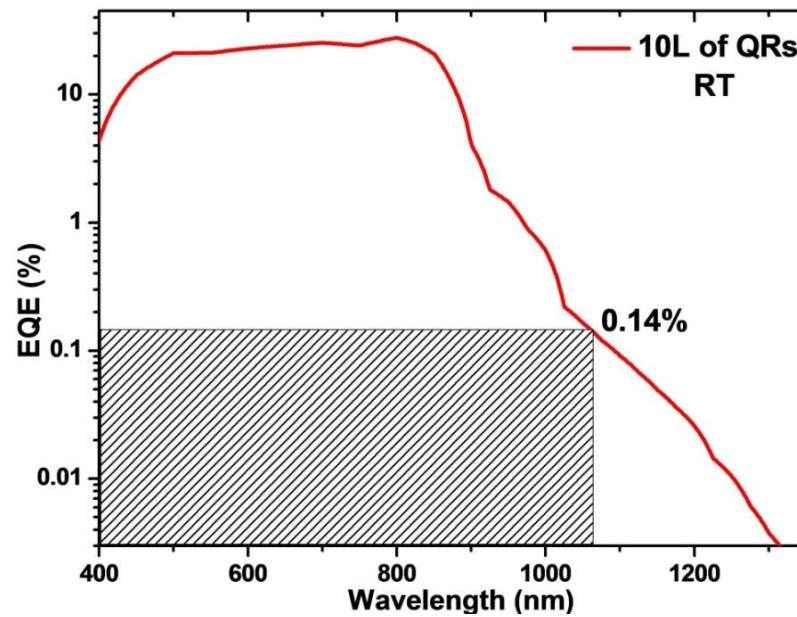
Figure 6.1: External quantum efficiency measured for one of the solar cells containing 10-layers of GaSb QRs obtained using white light illumination from a quartz-halogen lamp. The EQE of the quantum rings is indicated by the dashed line at 1064 nm.

Fig.6.1 shows the external quantum efficiency measured under white light illumination (quartz-halogen lamp) where the EQE of the quantum rings at 1064 nm is in good agreement with the calculated value for absorption strength (0.0014 or 0.14 %).

6.2.　Spectral response of the solar cell

Spectral response measurements were performed under a 100 W tungsten-halogen light source through a ¼ metre monochromator. In agreement with earlier work, the solar cells with QRs show an enhanced photo-conversion at longer wavelengths up to 1300 nm compared with the cells without rings (-see figure 3.7) as reported at Lancaster on similar samples [74]. The peak at 980 nm is due to absorption within the WL. The sub-band gap absorption from the GaAs SC at wavelengths longer than 870 nm is due to absorption from the highly doped p emitter. The long wavelength EQE is

increased by doubling the number of QR stacks. Although the QR solar cells show enhanced absorption below the GaAs bandgap, the EQE is reduced above the bandgap because the photo-generated minority holes from the base region undergo drift across the depletion region and are captured by the QRs.

6.2.1. Bias and temperature dependence

In order to understand the behaviour of photo generated minority holes further, bias and temperature dependant measurements were carried out. The photocurrent spectrum has been measured at 300 K and 77 K, under conditions of varying the external bias at 0 V,-3 V and -5 V, as shown in Figure 6.2. Two shoulders are clearly seen at room temperature (Fig. 6.2 a) around 980 nm and 1100 nm and are attributed to the WL and QR absorption respectively. However, the WL peak disappears and a change in the QR spectra is observed at 77 K. This behaviour of the WL is also noticed in temperature dependant PL measurements (figure 5.3).
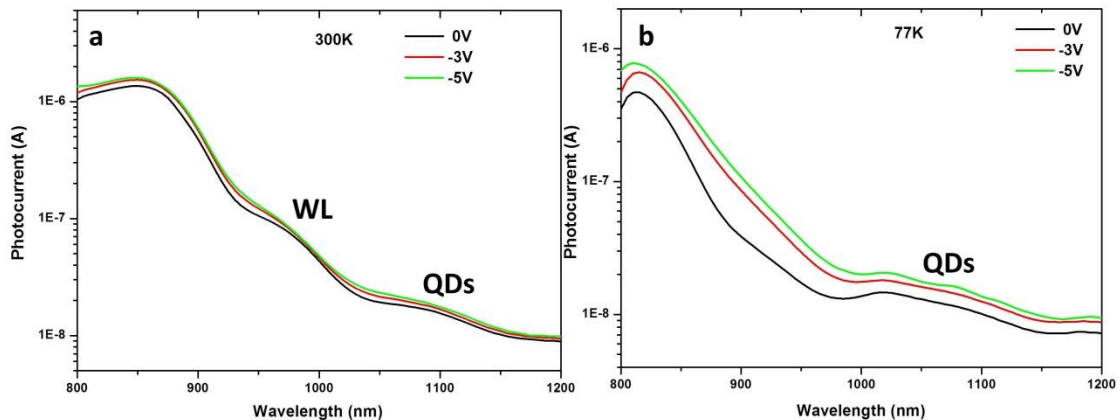
Figure 6.2: Photocurrent spectra of GaSb QRs at different bias conditions a) at room temperature 300 K the WL peak and QR peak are seen b) at 77 K the WL peak vanished and a broad QR peak is seen

At 77 K the photocurrent is clearly bias dependent - increasing as reverse bias is increases (Fig. 6.2 b). The enhancement in reverse bias results from the larger electron

hole overlap expected for reverse bias in type II heterostructures [136]. However, at 300 K the spectra show no difference as a function of reverse bias. This indicates the increase of the reverse bias does not enhance the tunnelling of holes from deeper confined levels (or from the shallower ones) at room temperature.
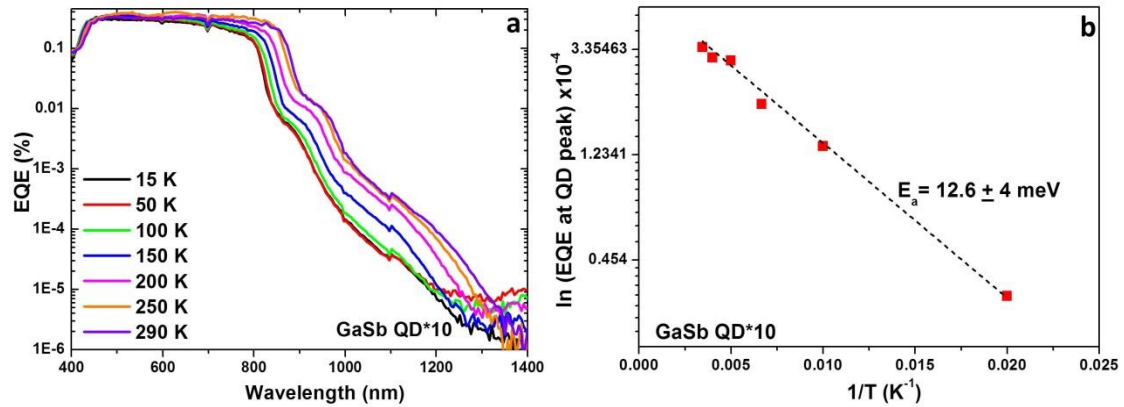
Figure 6.3: a) EQE of solar cells containing 10 layers of QRs as a function of different temperatures. b) Plot of the natural log of EQE of the QR peak vs inverse temperature. The gradient of the line gives the thermal activation energy.

The thermalization of carriers starts around 77 K leading to the escape of carriers from the WL to the QRs and the virtual disappearance of the WL peak. At high enough temperatures, the WL peak re-appears because the carriers have sufficient thermal energy to re-populate the WL. This effect is clearly seen in EQE spectra for GaSb QR solar cells measured from 15 K to 290K as shown in figure 6.3 a.

The EQE spectra for the GaAs control and GaSb QR solar cells measured at 100 and 290K are shown in Figure 6.4. Characteristics associated with the carrier behaviour in the GaSb QR are observed in the EQE spectra at low temperature. At room temperature (290 K), the EQE shows no significant difference except for the extended infrared response of the GaSb QR cell. However, below 100 K, the EQE of the GaSb QR cell is notably reduced, especially at longer wavelengths (above 600 nm).
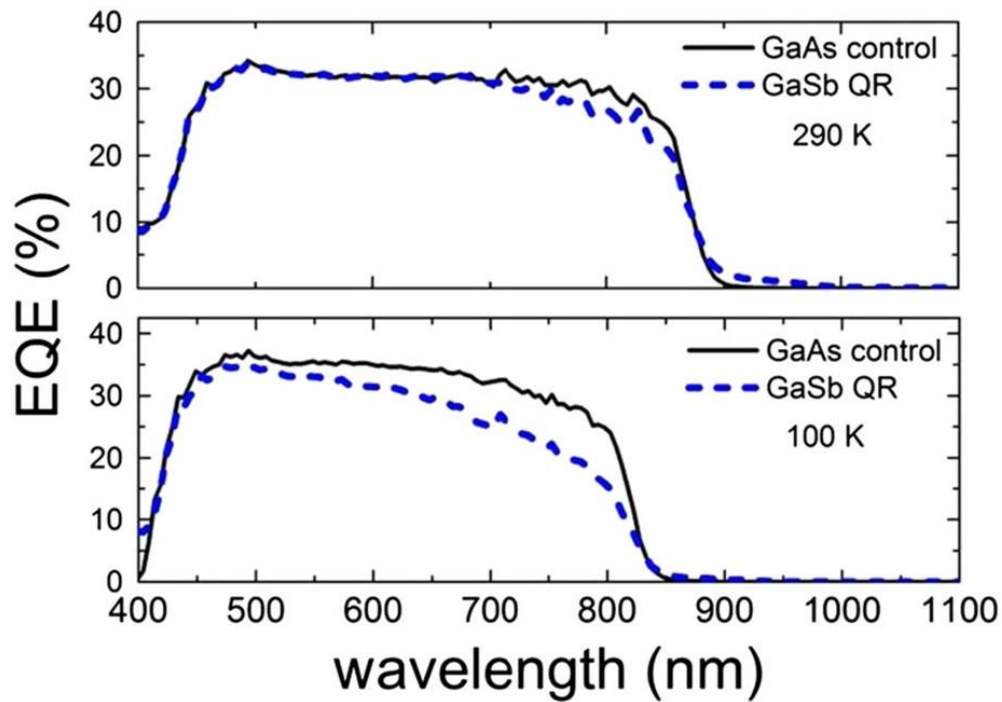
Figure 6.4: External quantum efficiency (EQE) spectra for the GaAs control (solid line) and GaSb quantum ring (QR) solar cells (dotted line) measured at 100 and 290 K [128].

Because of the wavelength dependence of the absorption coefficient in GaAs, photons with short wavelength (<500 nm) are mainly absorbed within the emitter of the solar cell (<0.5 μm), whilst photons with long wavelengths (>700 nm) can easily penetrate a few microns of the GaAs. For short wavelengths, photo-excited minority carriers (electrons) in the top p-GaAs region diffuse towards the n-GaAs bottom region via the intrinsic region. There is no electron confining potential around the QR; therefore, electrons can easily pass through the intrinsic region. On the other hand, for long wavelengths, photoexcited minority carriers (holes) generated within the n-GaAs base of the cell diffuse towards the p-GaAs top via the intrinsic region. Because of the large valence band offset at the GaAs/GaSb QR interface, some of these holes become trapped by the QRs and must be extracted by thermal excitation in order to contribute to the external photocurrent. This thermal extraction of holes is significantly reduced

at low temperatures, leading to the observed decrease in the EQE. The small reduction in room temperature EQE at long wavelengths (around 800 nm) suggests that the rate of thermionic hole emission might be insufficient at room temperature. An activation energy of 12.6 ± 4 meV is deduced from the plot of the natural log of EQE of the QR peak vs inverse temperature (see figure 6.3 b). This activation energy corresponds to the highest bound hole state of the QRs [137].
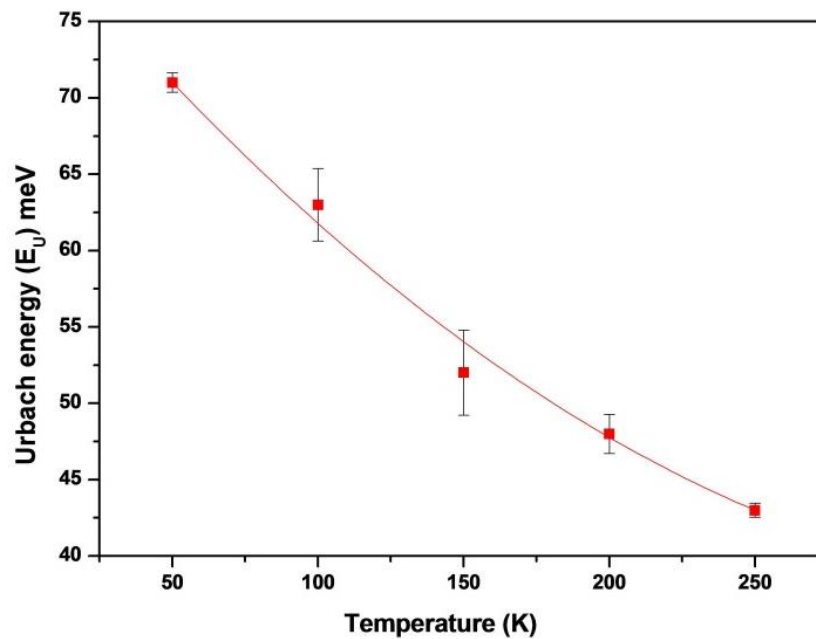
Figure 6.5: Temperature dependence of Urbach energy of GaSb/GaAs quantum dot solar cell

In GaAs, the extended energy states near the band edge facilitate the below-bandgap absorption. This can be described by an Urbach tail as a consequence of a break from a perfect lattice periodicity i.e. defects in the sample. The Urbach tail absorption width or Urbach energy (E_U) is calculated by using the equation 3.8 from EQE measurements at different temperatures. The below band gap absorption tail is due to the radiative recombination between trapped electrons and trapped holes in tail states and structural disorder. The Urbach energy decreases as a function of temperature as shown in figure 6.5. Such a decrease of the Urbach energy can be explained to be due

to the reduction of structural disorder associated with the defects in the sample. This is elaborately discussed later in this chapter.

6.3. Delta doping and positioning effects on spectral response

The influence of delta doping and positioning on the current voltage characteristics was examined in section 5. This also affects the spectral response of the solar cell and is considered further in this section. The EQE of solar cells containing QR with different delta-doping is shown in figure 6.6, where the influence on below bandgap absorption is clearly evident. The modulated n- doping of QRs (Sample B earlier), partially fills the quantum rings with electrons to reduce recombination and helps to recover the V_{oc} as discussed in chapter 5. But the transition probability of electrons from the valence band to conduction band is reduced in these QRs, which unfortunately weakens the absorption in the long wavelength range (figure 6.6). In the case of sample C, although the photocurrent of the cell is reduced, the sub-bandgap photoresponse is greatly increased. It is interesting that a strong extended photoresponse is observed for p-doped quantum rings in the intrinsic region (Sample B), higher than that of the undoped solar cell (Sample A). This is because the transition probability of an electron from the valence band to the conduction band via the QR hole states (which could be considered as an intermediate band) is greatly increased. The photocurrent contributions by the sub-band gap photons can be calculated by integrating the product of EQE and spectral irradiance of the tungsten halogen light source (see Table 2 and figure 6.7). Thus the contribution from the p doped QRs and sub-band gap photons to the total short circuit current (as shown in table 1) is higher than in the other devices studied here.
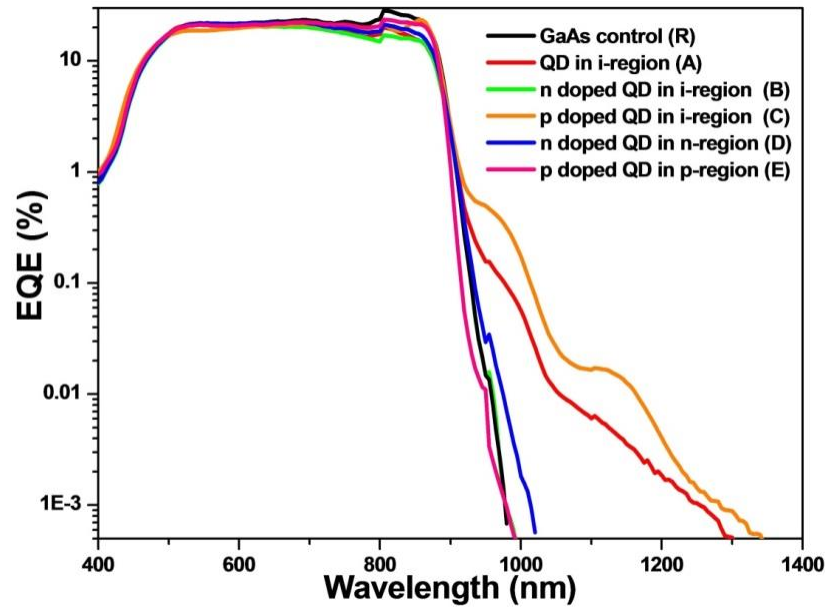
Figure 6.6: EQE of delta doped QRSCs in depletion and flat band regions

For sample E, there is almost no contribution to the sub-band gap photocurrent from the QRs. This behaviour is in contrast to sample C (p QRs in i-region) which gave the highest photoresponse. Hence, the p-doping of QRs placed in the i or p region does not favour the overall solar cell performance.

	Sample R	Sample A	Sample B	Sample C	Sample D	Sample E
Integrated J_{sc} from EQE above 930 nm ($\mu A/cm^2$)	1.5	29	1.7	85	3.9	0.75

Table 2: Comparison of Quantum dot solar cells to GaAs reference solar cell

However, for sample D, the small increase in the long wavelength photo-response is promising and can be attributed to the increased electron population in the QR arising from the n-δ-doping. But, this is limited due to the electrons around the QRs on the n-

side. The sub bandgap photocurrent could be further increased by stacking additional layers of QRs without compromising the open circuit voltage.
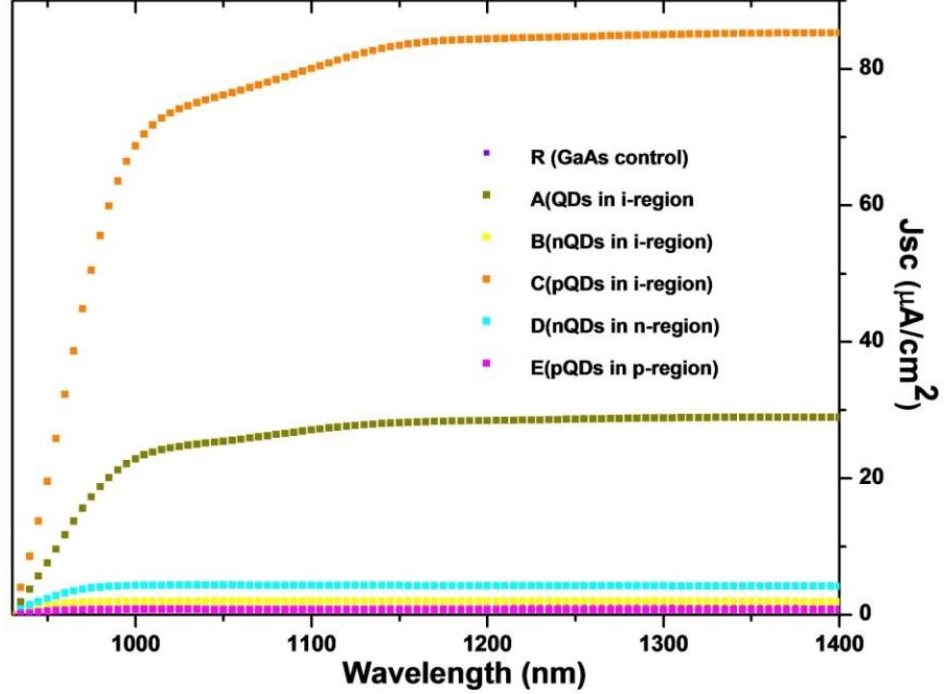
Figure 6.7: Photocurrent contributions by the sub-band gap photons calculated by integrating the product of EQE and spectral irradiance of the tungsten halogen light source

6.4. Urbach tail – Below band gap absorption analysis

An approach to derive the below-bandgap absorption in GaSb/GaAs self-assembled quantum ring (QR) devices using external quantum efficiency measurements [104] at room temperature is presented. As shown in figure 6.8, the EQE measurements below the band gap follow an exponential dependence on photon energy as the absorption coefficient. The measured data for the GaAs control device is fitted using equation,

$$\eta_{urbach} = \alpha_0 e^{\frac{E_g - \hbar\omega}{E_U}}$$

(6.1)

and the Urbach energy (E_U) of 0.0158 eV or 15.8 $\pm$ 0.2 meV is determined. This value is higher than 7 meV in intrinsic GaAs [138]. For the GaAs control device, the Urbach tail width is mainly determined by the doping level of the main absorption layer. The extended Urbach tail absorption in QR devices is demonstrated clearly in figure 6.8. To describe the tailing density of states in QR devices the energy states of both QR and WL have to be considered. For the quantum dot solar cell samples A, C and D, the Urbach energy is found by fitting the data using the equation 3.12 for αL. The Urbach energy for QR samples A, C and D is found to be 49.7 $\pm$ 0.3 meV, 53.4 $\pm$ 0.5 meV and 20.0 $\pm$ 0.2 meV which are larger compared to the GaAs Urbach energy of 15.8 meV. The αL values are then substituted in equation 3.11 and η_{Urbach} values are obtained. For the QR devices, the built-up strain creates disruption to the lattice, which is characterized by a much larger Urbach energy broadening.

Figure 6.8 shows the Urbach tail fitting (dashed lines) for the external quantum efficiency (η_{Urbach}) of a control device and the quantum dot solar cells. The p- delta doped QR sample C shows the higher absorption width of 53.4 meV compared to the other devices studied here. This is attributed to the presence of defects in the depletion region where QRs are inserted leading to V_{oc} reduction. According to equation 3.10, the carrier generation efficiency via the QR and WL transition levels ($\eta_{QR\&WL}$) can be obtained by subtracting η_{Urbach} from the measured η_t.

In Figure 6.9, the contribution of WLs and QRs is plotted based on their transition energies for all the devices. The contribution of the QR and WL to the absorption coefficient $\eta_{QR\&WL}$ is given by the following expression:

$$\eta_{QD\&WL} = (1-R)(1-e^{-\alpha_{QD\&WL}L})\eta_{int} \tag{6.2}$$
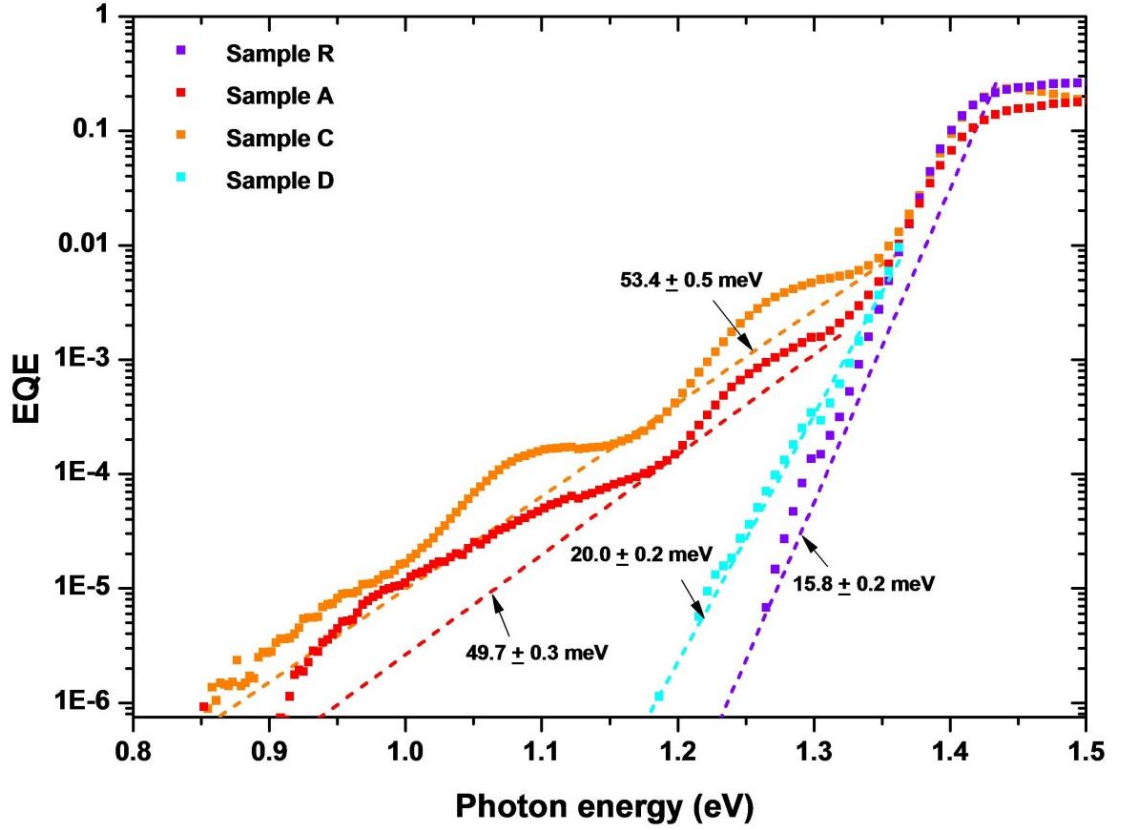
Figure 6.8: External quantum efficiency of a control device (R) and the quantum dot solar cells (A, C, D) with their respective Urbach tail fitting.

Where, η_{int} is the internal quantum efficiency, R is the surface reflectivity (~0.3) and L is the layer thickness (~20 nm). When the absorption coefficient is sufficiently small, the above equation can be further simplified to

$$\eta_{QD\&WL} = (1 - R)\alpha_{QD\&WL}L\eta_{int} \tag{6.3}$$

Assuming that the internal quantum efficiency is 100% through the energy range of interest, the dependence of $\alpha_{QR\&WL}$ in energy can then be plotted [138]. The absorption curve for sample A is fitted with Gaussian line shapes centred at photon energies as

shown in figure 6.10. The local maxima of the first derivative were used to identify

the centre of the peaks to fit for QR and WL transitions.
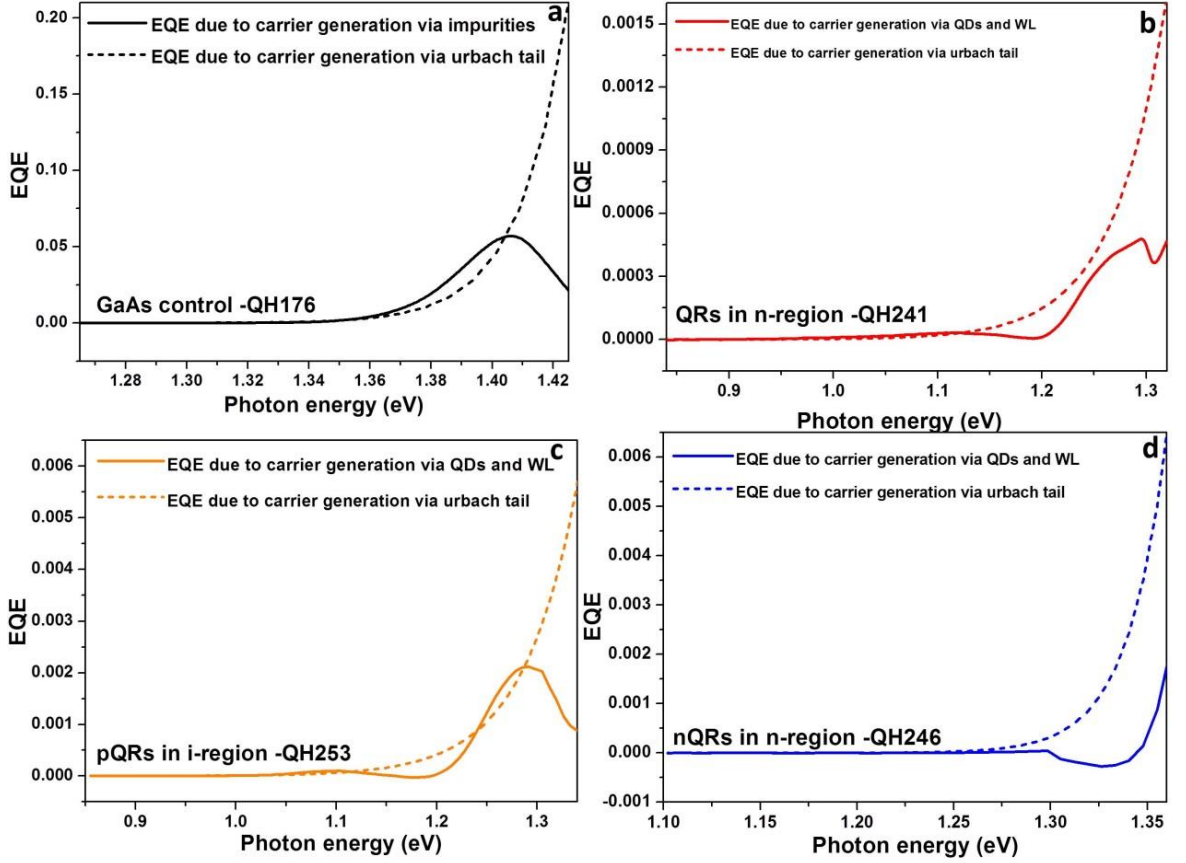
Figure 6.9: External quantum efficiency due to carrier generation via the Urbach tail and the QR and

WL energy levels; a) Control device sample R, b) Sample A, c) Sample C, d) Sample D

The two transitions of sample A are found to be centred at 1.30 eV corresponding to

the WL, and 1.13 eV corresponding to the QRs. Hence the absorbance due to the

transition energies for sample A is given by the following equation:

$$\alpha_{QD\&WL}L = 40.05e^{-0.5\left(\frac{x-1.30}{0.047}\right)^2} + 3.1e^{-0.5\left(\frac{x-1.13}{0.06}\right)^2} \tag{6.4}$$
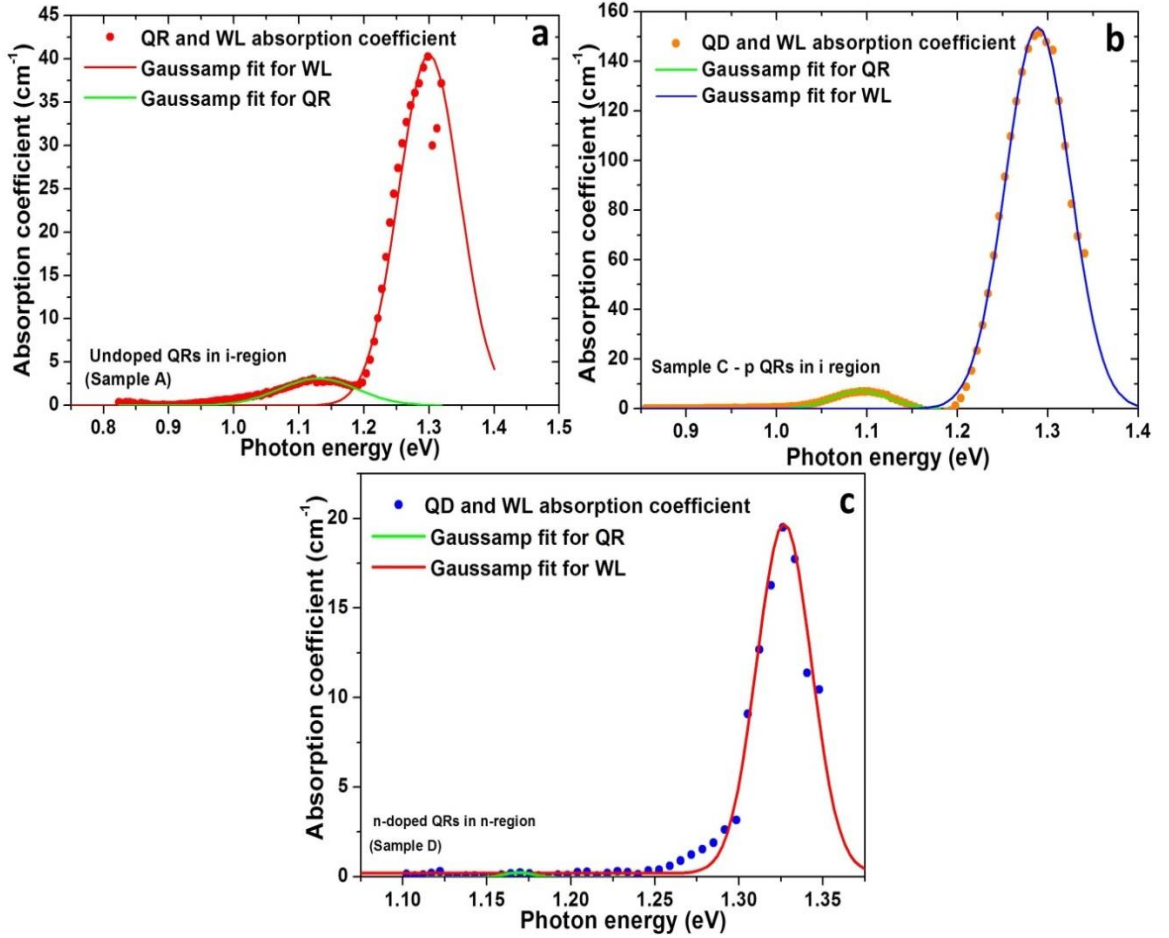
Figure 6.10: Derived quantum dot and wetting layer absorption coefficient with Gaussian line shape fitting for; a) sample A, b) sample C and c) sample D

The two transition states of sample C are found to be centred at 1.29 eV corresponding to the WL and 1.13 eV corresponding to the QDs. Hence the absorbance due to the main transition energies is given by the following equation:

$$\alpha_{QD\&WL}L = 153.8e^{-0.5\left(\frac{x-1.29}{0.035}\right)^2} + 7.10e^{-0.5\left(\frac{x-1.13}{0.031}\right)^2} \tag{6.5}$$

Similarly the two main transition states of sample D are found to be centred at 1.33 eV corresponding to WL and 1.17 eV corresponding to QDs. Hence the absorbance due to the transition energies is given by the following equation:

$$\alpha_{QD\&WL}L = 19.6e^{-0.5\left(\frac{x-1.33}{0.015}\right)^2} + 2.5e^{-0.5\left(\frac{x-1.17}{0.02}\right)^2}$$

(6.6)

The measurement of EQE at room temperature is used to derive the spectral dependence of the QD absorption. Mostly researchers have used photoluminescence, photoreflectance, electroluminescence, and differential transmission measurements. The fitted results obtained here are in good agreement with the results obtained via other methods [41][112]. The advantage of this method is that it gives the absorption strength of QDs and WL transition levels directly. Potentially, even higher resolution can be obtained by taking the measurements at lower temperatures.

The integral of the absorption coefficient over frequency for the ground state transition of the QRs is directly related to the spontaneous lifetime in QRs given by the following expression [139] [140]:

$$\int \alpha_{QD_{ground}transition} dv = \frac{3N\lambda^2}{8\pi n^2 \tau_{sp}}$$

(6.7)

where τ_{sp} = 1 ns [141] and n is the index of refraction, N is the density of QD ground states in the absorber and is twice the QR density, which is 1.5×10^{16} cm^{-3}. The theoretically integrated absorbance via QR ground states is therefore calculated as 1.04×10^{15} cm^{-1}s^{-1} according to Equation 5.4, which is in a reasonable agreement of the experimental derived value 8.1×10^{15} cm$^{-1} \cdot$ s^{-1}.

Therefore, the common main transition energies extracted in all the three samples are 1.3 eV for WL and 1.1 eV for GaSb QRs. Using these transition energies and the GaAs energy gap of 1.42 eV, the heavy hole confinement energies for the QRs (1.42eV - 1.1 eV= 320 ± 20 meV) and for the WL (1.42 eV − 1.3 eV= 120 ± 10 meV) are estimated [136]. The calculated values are shown in Figure 6.11.
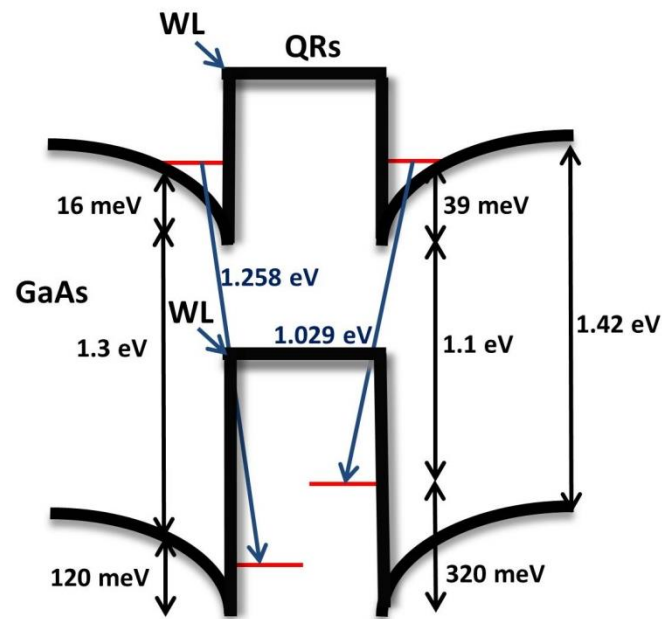
Figure 6.11: Energy band diagram showing the origin of the PL transition energies (blue colour line) and the transition energies obtained from EQE measurements at 300 K.

It has been reported that various factors could affect the localization energy of holes, i.e., the geometry; the GaSb/GaAs interface composition, as well as doping effects when relating the extended response of the solar cell with the structural characteristics of type-II quantum structures [142]. The transformation of GaSb quantum rings into ring-like structures could also alter the localization energy [143] [144]. The localization energy calculated with a value of 320 meV is small compared to values previously determined for the same material system [145] [146]. But this value matches the one determined by T. Nowozin and authors [147]. They suggest that

small hole confinement energy might be because the QRs are very small or have a small Sb content at the centre. In our case this is confirmed by high angle annular dark field (HAADF)-scanning transmission electron microscopy (STEM) images of GaSb QRs in which the Sb content is missing at the centre - Figure 6.12 a. Structural defects have not been found and the QRs appear as two bright lobes.
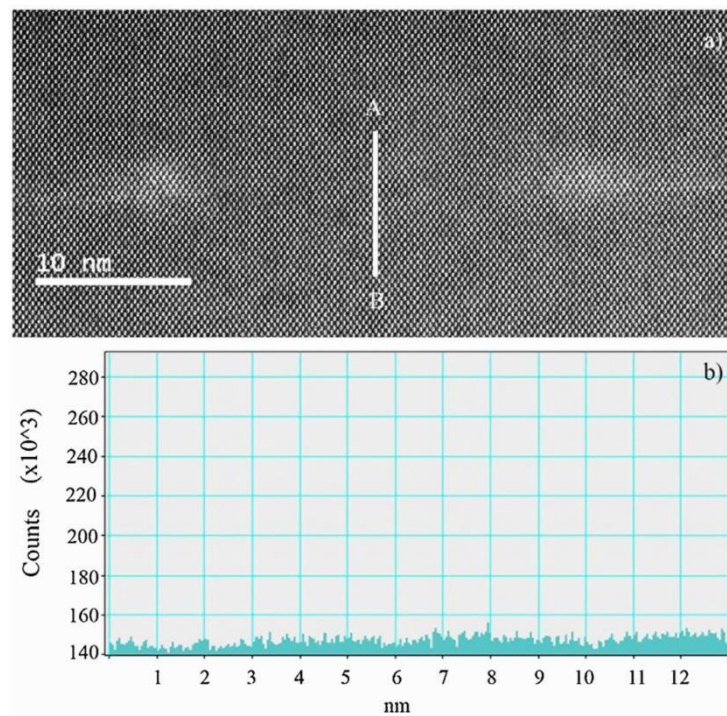
Figure 6.12: (a) HAADF-STEM image of the sample C in cross sectional view, where a single GaSb QR can be observed; (b) intensity profile taken in the line A–B in the image of Fig. 1(a), showing the absence of intensity related to the presence of Sb [133].

Chapter 7

Conclusion

In this thesis, electrical and optical characterization studies of GaSb QRs in GaAs solar cells were undertaken to investigate carrier dynamics and absorption characteristics.

To begin with, basic photoluminescence spectroscopy results indicate that the presence of the wetting layer plays a major role in carrier dynamics of GaSb/GaAs quantum ring solar cells. The activation energies for thermal quenching of QRs and WL were found to be 52 ± 10 meV and 21 ± 5 meV respectively, in agreement with earlier work.

The properties of the hole escape from stacked layers of the GaSb QR embedded within the GaAs solar cells have been investigated by using photocurrent measurements made under direct excitation of the QR with a 1064 nm laser. It was found that the photocurrent increased linearly with increasing excitation power without saturation, indicating that the thermal emission rate of the holes ($\sim 10^{11}$ to 10^{12} s^{-1}) is faster than the recombination rate ($\sim 10^{9}$ s^{-1}). The photocurrent was analyzed by separating the temperature independent component associated with tunneling from the temperature dependent thermionic component to extract the thermal activation energy for the thermionic hole emission. The hole activation energy of $\sim 40 \pm 10$ meV extracted from the temperature dependent measurements revealed that the holes generated in the QRs can readily escape and contribute to the photocurrent without a significant recombination at 300 K. The thermal activation energy was found to be

weakly dependent on the incident light level and increased by only a few meV over several orders of excitation intensity. This effect was related to charging of the QR with up to 15 holes, which results in band bending. The calculated absorption strength of our QRs when directly probed by using a 1064 nm laser with an optical power of 2.6 Wcm^{-2} was found to be $\sim 1.4 \times 10^{-4}$ per layer of the QRs. The thermal escape rate of the holes was calculated and found to be $\sim 10^{11}$ to 10^{12} s^{-1} which is much faster than the radiative recombination rate 10^{9} s^{-1}. This behavior is beneficial for the concentrator solar cell performance and has the potential to increase solar cell efficiency under a strong solar concentration.

The EQE measurements reveal a reduction in the photocurrent generation in the GaAs base and depletion regions in the QR SC which reduces the overall J$_{sc}$. This loss mechanism is enhanced at low temperatures due to the slow hole thermal emission rate from the QRs. An activation energy of 12.6 meV is deduced which corresponds to the highest bound hole state of the QRs. This suggests that the rate of thermionic hole emission might be insufficient at room temperature.

The effects of delta doping and positioning of GaSb QRs on the performance of GaAs single junction solar cells in terms of current-voltage characteristics and photoresponse were established. The V$_{oc}$ for the solar cell with delta doped QRs located in the p or n region is recovered compared to that for undoped QRs in the intrinsic region. This voltage recovery is attributed to the position of the QRs away from an area of highest electric field and reduced SRH recombination. The approach of placing QRs in the n-region of the solar cell instead of the depletion region may be

useful in helping to increase the conversion efficiency of solar cells because the long wavelength response could be further improved by stacking more layers of QRs.

The introduction of dopants into GaSb nanostructures was shown to influence the formation of QRs. Doping with Be $(2 \times 10^{18} \, \text{cm}^{-3})$ assists the formation of GaSb QR containing no Sb in their centre. By comparison, Te doping $(1 \times 10^{17} \, \text{cm}^{-3})$ was less efficient at removing Sb and consequently GaSb nanocups were produced. Hence, understanding the effect of the introduction of dopants in tailoring the opto-electronic properties of semiconductor nanostructures requires a careful analysis of their morphological characteristics, as this morphology can differ from that of undoped nanostructures.

The temperature dependent I-V characteristics were studied for a 10 layer GaSb QR and GaAs control solar cell (SC). Both the QR sample and the control sample showed a steady increase of J_{SC} with increasing temperature, resulting from the increased photo-absorption associated with the GaAs bandgap narrowing. An increase in dark current was observed in the GaSb QR SC due to introduction of additional recombination paths via the QR confined states, which also gives rise to an ideality factor near 2 at room temperature, which is similar to that in the GaAs control sample.

The Urbach tail contributions from an EQE measurement for both QR and control devices at room temperature were obtained. The impact of extended Urbach tail absorption in a GaSb/GaAs QRs solar cell was discussed. For a bulk GaAs device, the Urbach tail width was mainly determined by the doping level of the main absorption layer. The derived Urbach energy for the GaAs control device was 15.8 ± 0.2 meV, and for the QR devices, a much larger Urbach energy broadening of up to

53.4 $\pm$ 0.5 meV (p doped QR device) was obtained. The analysis of below-bandgap absorption has enabled quantitative determination of the transition energies in QDs and in the WL. Using the transition energies, the heavy hole confinement energies for the QRs (320 $\pm$ 20 meV) and for the WL (120 $\pm$ 10 meV) were estimated and compared.

7.1. Suggestions for future work

Based on the results of this study, the following recommendations on possible work in the future are given below:

- The maximum of 10 GaSb QR layers embedded in GaAs was studied in this work. More layers of QRs could be grown by MBE (considering strain balancing techniques) in order to increase the absorption and photocurrent in the solar cell. Systematic experiments to study the effect of QR stack number on solar cell performance and the carrier transport in the QR region could be performed.

- The QD size and density are dependent on the growth conditions such as the V/III flux ratio, substrate orientation, growth temperature, and material of the buffer layer. These conditions could possibly be further optimized to get an ultra-high QR density of 1×10^{12} cm^{-2} in the single layer with increased uniformity.

- The approach of placing QRs in the n-region of the solar cell could be studied further by applying different delta doping concentrations.

- The QD-IBSC concept could be implemented by adjusting the spacer layer thickness during growth process. This approach has great potential provided

the intermediate band can be effectively de-coupled from the conduction and valence bands.

- For further understanding of intermediate-band transitions in GaSb QRs, studies based on multiphoton quantum-efficiency measurements are needed. Conventional monochromatic EQE spectroscopy cannot determine the gain in photocurrent via Two step photon absorption processes (TSPA); instead an IR bias light could be used to promote TSPA that induces a change in the EQE

- Such structures would benefit from measurements using high solar concentration - more similar to the actual operating conditions for CPV - to see if two photon events result in increased efficiency.

- Internal quantum efficiency should be determined in addition to external quantum efficiency by adding absorption measurements to the suite of characterizations. Once this has been accomplished, poor performance can be attributed to either low absorption or poor electrical characteristics. This provides direction towards understanding the mechanisms that limit the cell's overall performance.

- In order to investigate the dynamics of carrier recombination in GaSb QRs, the time-resolved PL lifetime measurements could be undertaken and correlated with calculations of carrier emission and capture rates to/from the QRs

- Time-resolved cathodoluminescence (TRCL) measurements could also be performed, provided a long wavelength detector is available.

- By changing the GaAs barrier to AlGaAs, the quantum ring energy levels could be situated deeply enough to achieve transition energies nearly matching the ideal IBSC. Also the reduction in open circuit voltage could be minimized because of the increase in the total bandgap of the GaSb/AlGaAs structure.

- The behavior of the ring-shaped GaSb QDs under external magnetic fields could be studied to understand Aharonov- Bohm oscillations. Their period and amplitude could be varied with the magnetic field.

- FDTD modelling and simulations of GaSb QD/QR solar cell structure could be developed using *Lumerical* DEVICE software which would enable accurate modeling of solar cell operation and simulation of electrical characterization as well as plasmonic enhancements.

- Finally, the GaSb QRs should ultimately be incorporated into existing multi-junction cells as a means to increase the overall efficiency. However, there are many considerations before this can be achieved in practice.

List of figures and Tables

131

Bibliography

[1] Global Energy Trends – BP Statistical Review, 2014

[2] IEA (2006), p. 127

[3] Chemviews /Greenpeace, European Photovoltaic Industry Association (EPIA), Renewables 2011, Biofuels Platform

[4] Image from Earth's Energy Budget, NASA

[5] National renewable research laboratory, 1975-2015 solar cell efficiency chart

[6] Solopower solutions technology/thin-film-photovoltaics/

[7] Yablonovitch, Eli; Miller, Owen D.; Kurtz, S. R.. "The opto-electronic physics that broke the efficiency limit in solar cells", 38th IEEE Photovoltaic Specialists Conference. p. 001556, 2012

[8] Hubbard, S. M., Bailey, C.Polly, S. Aguinaldo, R.; Forbes, D. Raffaelle, R. Proc, "Characterization of quantum dot enhanced solar cells for concentrator photovoltaics" 34th IEEE Photovolt. Spec. Conf, 2009

[9] William Shockley and Hans J. Queisser, "Detailed Balance Limit of Efficiency of p-n Junction Solar Cells", Journal of Applied Physics, Volume 32, pp. 510-519, 1961

[10] Albert Polman & Harry A. Atwater, "Photonic design principles for ultrahigh efficiency photovoltaics" Nature Materials 11, 174–177, 2012

[11] Renewable and Alternative Energy Resources: A Reference Handbook, By Zachary Alden Smith, Katrina D. Taylor.

[12] Integrated nanomaterials laboratory/ PROJECTS/ High efficiency Quantum dot solar cells

[13] A. Luque, and A. Martí, "Increasing the efficiency of ideal solar cells by photon induced transitions at intermediate levels", Phys. Rev. Lett. 78, 5014, 1997

[14] C. G. Bailey, D. V. Forbes, R. P. Raffaelle, and S. M. Hubbard, "Near 1 V open circuit voltage InAs/GaAs quantum dot solar cells," Appl. Phys. Lett. 98(16), 163105, 2011

[15] Carrington PJ, Wagener MC, Botha JR, Sanchez AM, Krier A, " Enhanced infrared photo-response from GaSb/GaAs quantum ring solar cells" Applied Physics Letters. 3;101(23): 231101, 2012.

[16] Daniil Feldman "Nanostructures Capable of Emission and Absorption in Near Infrared for Biochemical Applications" Forest Hills HS, Forest Hills, NY 11375

[17] Takuya Kawazu, "Electric states in laterally and vertically arrayed type-II quantum dots" Japanese Journal of Applied Physics 54, 04DJ01, 2015

[18] Carrington PJ, Mahajumi AS, Wagener MC, Botha JR, Zhuang Q, Krier A, "Type II GaSb/GaAs quantum dot/ ring stacks with extended photoresponse for efficient solar cells" Physica B; 407: 1493, 2012

[19] Hwang, J., Martin, A.J., Millunchick, J.M., Phillips, J.D, "Thermal emission in type-II GaSb/GaAs quantum dots and prospects for intermediate band solar energy conversion", J. Appl. Phys., 111, p. 074514, 2012

[20] Wiley and Sons Chichester, Renewable Energy and Climate Change/ Figure 2: Structure and processes of a solar cell

[21] Allport, Christopher, Sines, Paul, Schreiner, Brandon & Das, Biswajit,"Education in Three Dimensions: Using Virtual Reality in Education for Illustrating Spatial Relationships" ICEE'99, Czech Republic, Paper No. 334

[22] Luque, Antonio; Steven Hegedus (29 March 2011). Handbook of Photovoltaic Science and Engineering. John Wiley & Sons.

[23] B. Van Zeghbroeck, Principles of Semiconductor Devices, Chapter 4: "p-n junctions", 2011

[24] Gupta, Sanjeev Electronic Devices & Circuits. new delhi: Dhanpat Rai Publications, 2011

[25] C. Papadopoulos, Solid-State Electronic Devices: An Introduction, Springer Science+Business Media New York 2014

[26] pvmeasurements/ figure/Air Mass AM0 AM1 0 AM1 5

[27] Nelson, Jenny. The Physics of Solar Cells. London: Imperial College Press, 2003.

[28] pveducation.org/pvcdrom/appendices/standard-solar-spectra

[29] Mathew Guenette, "The efficiency of photovoltaic solar cells at low temperatures" Page 9, Honours Thesis, 2006

[30] Cuevas A. The Recombination Parameter J_0. Energy Procedia

[31] Lindholm FA, Fossum JG, Burgess EL. " Application of the superposition principle to solar-cell analysis". IEEE Transactions on Electron Devices.;26:165–171, 1979

[32] Eduardo Lorenzo (1994). Solar Electricity: Engineering of Photovoltaic Systems. Progensa. ISBN 84-86505-55-0.

[33] Antonio Luque and Steven Hegedus (2003). Handbook of Photovoltaic Science and Engineering. John Wiley and Sons. ISBN 0-471-49196-9.

[34] Jenny Nelson, "The Physics of Solar Cells. Imperial College" Press. ISBN 978-1-86094-340-9, 2003

[35] pveducation.org/pvcdrom/solar-cell-operation/fill-factor

[36] Part II – Photovoltaic Cell I-V Characterization Theory and LabVIEW Analysis Code, white paper, National instruments tutorial, May 10, 2012

[37] pveducation.org/pvcdrom/solar-cell-operation/quantum-efficiency

[38] http://www.pveducation.org/pvcdrom/solar-cell-operation/quantum-efficiency

[39] Nezam Uddin, Md.Motiur Rahman, Tanvir Ahmed & Atiqulislam, "Performance Analysis of Quantum Dot Intermediate Band Solar Cell (QD IBSC)", Global Journal of Researches in Engineering ,Volume XV Issue I Version I 13, 2015

[40] N.S. Beattie ,n, G. Zoppi, P. See, I. Farrer , M. Duchamp , D.J. Morrison , R.W. Miles , D.A. Ritchie , " Analysis of InAs/GaAs quantum dot solar cells using Suns-V_{oc} measurements" Solar Energy Materials & Solar Cells 130, 241–245, 2014

[41] F. Hatami, M. Grundmann, N. N. Ledentsov, F. Heinrichsdor, R. Heitz, J. BÄohrer, D. Bimberg, S. S. Ruvimov, P. Werner, V. M. Ustinov, P. S. Kop'ev, and Zh. I. Alferov, "Carrier dynamics in type-II GaSb/GaAs quantum dots", Phys. Rev. B 57, 4635, 1998

[42] C.-K. Sun, G. Wang, J. E. Bowers, B. Brar, H.-R. Blank, H. Kroemer, and M. H. Pilkuhn, "Optical investigations of the dynamic behavior of GaSb/GaAs quantum dots" Appl. Phys. Lett. 68, 1543, 1996

[43] IUPAC, Compendium of Chemical Terminology, 2nd ed. (the "Gold Book") (2006 corrected version).

[44] J. Tatebayashi, A. Khoshakhlagh, S. H. Huang, L. R. Dawson, G. Balakrishnan, and D. L. Huffaker, "Formation and optical characteristics of strain-relieved and densely stacked GaSb/GaAs quantum dots" Appl.Phys.Lett.89, 203116, 2006

[45] M. Geller, C. Kapteyn, L. Müller-Kirsch, R. Heitz, and D. Bimberg, "450 meV hole localization in GaSb/GaAs quantum dots," Applied Physics Letters, vol. 82, no. 16, pp. 2706–2708, 2003

[46] L. Muller-Kirsch, R. Heitz, A. Schliwa, O. Stier, and D. Bimberg, "Many-particle effects in type II quantum dots" Appl. Phys. Lett. 78, 1418, 2001

[47] Hiromi Fujita, Juanita James, Peter J Carrington, Andrew R J Marshall, Anthony Krier, Magnus C Wagener and Johannes R Botha, "Carrier extraction behaviour in

type II GaSb/GaAs quantum ring solar cells, Semicond. Sci. Technol. 29, 035014 (5pp), 2014

[48] Phu Lam , Sabina Hatch , Jiang Wu , Mingchu Tang , Vitaliy G. Dorogan , Yuriy I. Mazur , Gregory J. Salamo , Iñigo Ramiro , Alwyn Seeds , Huiyun Liu, "Voltage recovery in charged InAs/GaAs quantum dot solar cells", Nano Energy 6, 159–166, 2014

[49] Antonio Luque and Antonio Marti,"The Intermediate Band Solar Cell: Progress Toward the Realization of an Attractive Concept", Adv. Mater, 22, 160–174, 2010

[50] A. Kechiantz, A. Afanasev, J.-L. Lazzari 'Impact of Spatial Separation of Type-II GaSb Quantum Dots from the Depletion Region on the Conversion Efficiency Limit of GaAs Solar Cells' Mesoscale and Nanoscale physics, arXiv:1310.5075

[51] Stephen J Polly, David V Forbes, Kristina M Driscoll, Seth M Hubbard 'Delta Doping Effects on Quantum Dot Solar Cells' IEEE journal of Photovoltaics Vol.4, No.4.

[52] D. Zhou, P.E. Vullum, G. Sharma, S.F. Thomassen, R. Holmestad, T.W. Reenaas, B.O. Fimland "Positioning effects on quantum dot solar cells grown by molecular beam epitaxy" Appl. Phys. Lett., 96, p. 83108, 2010

[53] Yeongho Kim1 , Keun-Yong Ban1,3 , Darius Kuciauskas2 , Patricia C Dippo2 and Christiana B Honsberg "Impact of delta-doping position on photoluminescence in type-II InAs/GaAsSb quantum dots" Semicond. Sci. Technol. 30, 035006 (6pp), 2015

[54] Harald Brune, "Epitaxial Growth of Thin Films" Chapter 20, Page 421

[55] Rainer Timm PhD thesis, TU Berlin, 2007

[56] Stranski, I. N.; Krastanov, L.. "Zur Theorie der orientierten Ausscheidung von Ionenkristallen aufeinander". Sitzungsber. Akad. Wiss. Wien. Math.-Naturwiss. 146: 797–810, 1938

[57] Venables, John "Introduction to Surface and Thin Film Processes". Cambridge: Cambridge University Press. ISBN 0-521-62460-6, 2000

[58] K. Oura, V.G. Lifshits, A.A. Saranin, A.V. Zotov, and M. Katayama Surface Science: An Introduction. Berlin: Springer. ISBN 3-540-00545-5, 2003

[59] Chiu, C.-h.; Z. Huang; C. T. Poh. "Formation of Nanostructures by the Activated Stranski-Krastanow Transition Method". Physical Review Letters 93 (13): 36105, 2004

[60] Handbook of Self Assembled Semiconductor Nanostructures for Novel Devices in Photonics and Electronics by Mohamed Henini/ page 556

[61] Carrington, Peter James; Mahajumi, Abu Syed; Wagener, Magnus C.; Botha, Johannes Reinhardt; Zhuang, Qiandong; Krier, Anthony, "Type II GaSb/GaAs quantum dot/ring stacks with extended photoresponse for efficient solar cells" Physica B: Condensed Matter, Vol. 407, No. 10, p. 1493-1496,2012

[62] Koichi yamaguchi, Kunihiko yujobo and Toshiyuki kaizu, "Stranski-Krastanov Growth of InAs Quantum Dots with Narrow Size Distribution" Jpn. J. Appl. Phys. Vol. 39, pp. L 1245–L 1248, 2000

[63] P. J. Carrington, M. C. Wagener, J. R. Botha, A. M. Sanchez, and A. Krier, "Enhanced infrared photo-response from GaSb/GaAs quantum ring solar cells" Appl. Phys. Lett. 101, 231101, 2012

[64] Chi-Che Tseng, Shu-Cheng Mai, Wei-Hsun Lin, Shung-Yi Wu, Bang-Ying Yu, Shu-Han Chen, Shih-Yen Lin, Jing-Jong Shyue, and Meng-Chyi Wu, "Influence of As on the Morphologies and Optical Characteristics of GaSb/GaAs Quantum Dots" IEEE JOURNAL OF QUANTUM ELECTRONICS, VOL. 47, NO. 3, MARCH 2011

[65] Shih-Yen Lin and Wei-Hsun Lin "Type-II gallium antimonide quantum dots and rings for optical devices, SPIE Newsroom,2012

[66] M. A. Kamarudin, M. Hayne, R. J. Young, Q. D. Zhuang, T. Ben, and S. I. Molina, "Tuning the excitonic properties of self-assembled GaSb/GaAs quantum rings" Phys. Rev. B 83, 115311, 2011

[67] Peter J. Carrington, Robert J. Young, Peter D. Hodgson, Ana M. Sanchez, Manus Hayne, and Anthony Krier, "Long-Wavelength Photoluminescence from Stacked Layers of High Quality Type-II GaSb/GaAs Quantum Rings" Cryst. Growth Des., 13, 1226−1230, 2013

[68] Peter J. Carrington, Robert J. Young, Peter D. Hodgson, Ana M. Sanchez, Manus Hayne, and Anthony Krier, "Long-Wavelength Photoluminescence from Stacked Layers of High-Quality Type-II GaSb/GaAs Quantum Rings" Crystal Growth & Design, 13 (3), 1226-1230, 2013

[69] Jos´e Mar´ıa Rom´an, "State-of-the-art of III-V Solar Cell Fabrication Technologies, Device Designs and Applications", Advanced Photovoltaic Cell Design EN548, 2004

[70] Brendan M. Kayes, Hui Nie, Rose Twist, Sylvia G. Spruytte, Frank Reinhardt, Isik C. Kizilyalli, and Gregg S. Higashi, "27.6% conversion efficiency, a new record for single-junction solar cells under 1 sun illumination" IEEE, 978-1-4244-9965-6/11, 2011

[71] Hubbard, S.M., Bailey, C., Polly, S., Aguinaldo, R., Forbes, D., Raffaelle, R. 'Characterization of quantum dot enhanced solar cells for concentrator photovoltaics'. Proc. 34th IEEE Photovolt. Spec. Conf., vol. 1, pp. 1–6, 2009

[72] Hubbard, S.M., Cress, C.D., Bailey, C.G., Raffaelle, R.P., Bailey, S.G., Wilt, D.M. 'Effect of strain compensation on quantum dot enhanced GaAs solar cells', Appl. Phys. Lett., 92, p. 123512, 2008

[73] Sugaya, T., Furue, S., Komaki, H., et al. 'Highly stacked and well aligned In0.4Ga0.6As quantum dot solar cells with In0.2Ga0.8As cap layer', Appl. Phys. Lett., 97, p. 183104, 2010

[74] Carrington, P.J., Wagener, M.C., Botha, J.R., Sanchez, A.M., Krier, A.: 'Enhanced infrared photo-response from GaSb/GaAs quantum ring solar cells', Appl. Phys. Lett., 101, (23), p. 231101, 2012

[75] Wu J, Shao D, Li Z, Manasreh MO, Kunets VP, Wang ZM, Salamo GJ. Intermediate-band material based on GaAs quantum rings for solar cells. Applied Physics Letters; 95: 071908, 2009

[76]Linares PG, Martí A, Antolín E, Farmer CD, Ramiro Í, Stanley CR, Luque A. "Voltage recovery in intermediate band solar cells" Solar Energy Materials and Solar Cells; 98: 240, 2012

[77] Hwang, J., Martin, A.J., Millunchick, J.M., Phillips, J.D.: 'Thermal emission in type-II GaSb/GaAs quantum dots and prospects for intermediate band solar energy conversion', J. Appl. Phys., 111, p. 074514, 2012

[78] M. Hayne, J. Maes, S. Bersier, V. V. Moshchalkov, A. Schliwa, L. Muller-Kirsch, C. Kapteyn, R. Heitz, and D. Bimberg, "Electron localization by self-assembled GaSb/GaAs quantum dots." Appl. Phys. Lett. 82, 4355, 2003

[79] Carrington PJ, Wagener MC, Botha JR, Sanchez AM, Krier A. "Enhanced infrared photo-response from GaSb/GaAs quantum ring solar cells", Applied Physics Letters; 101: 23110, 2012

[80] Fujita H, James J, Carrington PJ,Marshall ARJ, Krier A, Wagener MC, Botha JR. Carrier extraction behaviour in type II GaSb/GaAs quantum ring solar cells. Semiconductor Science and Technology; 29: 035014, 2014.

[81] Juanita Saroj James, Hiromi Fujita, Peter J. Carrington, Andrew R.J. Marshall, Anthony Krier , "Carrier extraction from GaSb quantum rings in GaAs solar cells using direct laser excitation" IET Optoelectron., Vol. 8, Iss. 2, pp. 76–80, 2014

[82] A. Kechiantz, A. Afanasev, J.-L. Lazzari 'Impact of Spatial Separation of Type-II GaSb Quantum Dots from the Depletion Region on the Conversion Efficiency Limit of GaAs Solar Cells' Mesoscale and Nanoscale physics, arXiv:1310.5075

[83] J. Hwang, A. J. Martin, K. Lee, S. Forrest, J. Millunchick, and J. Phillips. "Preserving Voltage and Long Wavelength Photoresponse in GaSb/GaAs Quantum Dot Solar Cells". 39th IEEE Photovoltaic Specialists Conference Tampa, FL, 2013

[84] Stephen J Polly, David V Forbes, Kristina M Driscoll, Seth M Hubbard 'Delta Doping Effects on Quantum Dot Solar Cells' IEEE journal of Photovoltaics Vol.4,No.4.

[85] D. Zhou, P.E. Vullum, G. Sharma, S.F. Thomassen, R. Holmestad, T.W. Reenaas, B.O. Fimland "Positioning effects on quantum dot solar cells grown by molecular beam epitaxy" Appl. Phys. Lett., 96, p. 83108, 2010

[86] Yeongho Kim, Keun-Yong Ban, Darius Kuciauskas, Patricia C Dippo and Christiana B Honsberg "Impact of delta-doping position on photoluminescence in type-II InAs/GaAsSb quantum dots" Semicond. Sci. Technol. 30, 035006 (6pp), 2015

[87] Bai, W., Q. Gan, F. Bartoli, J.Zhang, L.Cai, Y.Huang and G. Song, 2009. Design of plasmonic back structures for efficiency enhancement of thin-film amorphous Si solar cells. Opt.Lett., 34:725-3727

[88] Zongheng Yuan, Xiaonan Li and Huang Jing, "Absorption enhancement of thin-film solar cell with rectangular Ag nanoparticle" J. Applied Sci., 14 98): 823-827, 2014

[89] Hiromi Fujita, Juanita James, Peter J Carrington, Andrew R J Marshall, Anthony Krier, Magnus C Wagener and Johannes R Botha, "Carrier extraction behaviour in type II GaSb/GaAs quantum ring solar cells" Semicond. Sci. Technol. 29, 035014, 2014

[90] M. Hayne, J. Maes, S. Bersier, and V. V. Moshchalkov, "Electron localization by self-assembled GaSbÕGaAs quantum dots" Appl. Phys. Lett., Vol. 82, No. 24, 16, 2003

[91] M. Hayne, O. Razinkova, and S. Bersier , "Optically induced charging effects in self-assembled GaSb/GaAs quantum dots" PHYSICAL REVIEW B 70, 081302(R), 2004

[92] Kai Cui, WenquanMa, JianliangHuang, YangWei, YanhuaZhang, YulianCao ,Yongxian Gu, TaoYang, "Multilayered type-II GaSb/GaAs self-assembledquantumdotstructure" Physica, E45, 173–176, 2012

[93] Monte, A.F.G., Qu, F.: 'Nonlinear effects of the photocurrent in self assembled InAs/GaAs quantum dots', J. Appl. Phys., 109, p. 053722, 2011

[94] Chang, W.-H., Hsu, T.M., Huang, C.C., et al.: 'A carrier escape study from InAs self-assembled quantum dots by photocurrent measurement', Phys. status solidi, b, , 224, (1), pp. 85–88, 2001

[95] Chang W-H, Hsu TM, Huang C C, Hsu S L, Lai C Y, Yeh N T, Nee T E and Chyi J-I, Phys. Rev. B 62 6959, 2000

[96] Hwang, J., Martin, A.J., Millunchick, J.M., Phillips, J.D.: 'Thermal emission in type-II GaSb/GaAs quantum dots and prospects for intermediate band solar energy conversion', J. Appl. Phys., 111, p. 074514, 2012

[97] Jinyoung Hwang, Andrew J. Martin, Joanna M. Millunchick, and Jamie D. Phillips, " Thermal emission in type-II GaSb/GaAs quantum dots and prospects for intermediate band solar energy conversion" J. Appl. Phys. 111, 074514, 2012

[98] Ibáñez, J., Leon, J., Vu, R., et al.: 'Tunneling carrier escape from InAs self-assembled quantum dots', Appl. Phys. Lett., 79, p. 13, 2001

[99] Che-Pin Tsai, Shun-Chieh Hsu, Shih-Yen Lin, Ching-Wen Chang, Li-Wei Tu, KunCheng Chen,Tsong-Sheng Lay, and Chien-chung Lin, "Type II GaSb quantum ring solar cells under concentrated sunlight" Vol. 22, No. OPTICS EXPRESS A364, 2014

[100] Hiromi Fujit, Juanita James, Peter J Carrington, Andrew R J Marshall, Anthony Krier1, Magnus C Wagener, "Carrier extraction behaviour in type II GaSb/GaAs quantum ring solar cells and Johannes R Botha3" Semicond. Sci. Technol. 29, 035014, 2014

[101] Hiromi Fujita, Juanita James, Peter J Carrington, Andrew R J Marshall, Anthony Krier, Magnus C Wagener and Johannes R Botha, "Carrier extraction behaviour in type II GaSb/GaAs quantum ring solar cells" Semicond. Sci. Technol. 29 035014, 2014

[102] Skolnick, M.S., Mowbray, D.J.: 'Self-assembled semiconductor quantum dots: fundamental physics and device applications', Annu. Rev. Mater. Res., 34, pp. 181–218, 2004

[103] Fry, P.W., Harris, L., Parnell, S.R., et al.: 'Modal gain and lasing states in InAs/GaAs self-organized quantum dot lasers', J. Appl. Phys., 87, p. 615, 2000

[104] Tian Li and Mario Dagenais, "Below-bandgap absorption in InAs/GaAs self-assembledmquantum dot solar cells" Prog. Photovolt: Res. Appl, 2014

[105] Adnano/ Technology of Ultra high vacuum Molecular beam epitaxy

[106] Atomic Force Microscope: A Tiny Record Player/University of California, Santa Barbara/Undergraduate research

[107] I Horcas, R Fernandez, J M G omez-Rodr guez, J Colchero, J Gomez- Herrero, and a M Baro. WSXM: a software for scanning probe microscopy and a tool for nanotechnology. The Review of scienti c instruments, 78(1),013705, 2007.

[108] Heikki Collana) and Kari Hjelt, "Does the low-temperature Arrhenius plot of the photoluminescence intensity in CdTe point towards an erroneous activation energy?" J. Appl. Phys. 81 (3),1997

[109] Jun Zhang, Wu Tian, Feng Wu, Shichuang Sun, Shuai Wang, Jiangnan Dai, Yanyan Fang, Zhihao Wu, Changqing Chen, Jiali Tai, Mingkai Li, and Yunbin He," Optical properties of the nonpolar a-plane MgZnO films grown on a-GaN/r-sapphire

templates by pulsed laser deposition" Optical Materials Express Vol. 4, Issue 11, pp. 2346-2354, 2014

[110] Shawn Willis, Advanced Optoelectronic Characterisation of Solar Cells, Figure 2.1 in Thesis, Oriel college

[111] Jun Tatebayashi, Baolai Liang, David A. Bussian, Han Htoon, Shenghong Huang, Ganesh Balakrishnan, Victor Klimov, L. Ralph Dawson, Diana L. Huffaker, "Formation and optical characteristics of type-II strain-relieved GaSb/GaAs quantum dots by using an interfacial misfit growth mode" IEEE Transactions on Nanotechnology, Vol 8, 2009

[112] L. Müller-Kirsch, R. Heitz, U. W. Pohl, D. Bimberg, I. Häusler, H. Kirmse, and W. Neumann, "Temporal evolution of GaSb/GaAs quantum dot formation" Appl. Phys. Lett. 79, 1027,2001

[113] M Ahmad Kamarudin, M Hayne, Q D Zhuang, O Kolosov, T Nuytten, V V Moshchalkov and F Dinelli, "GaSb quantum dot morphology for different growth temperatures and the dissolution effect of the GaAs capping layer" J. Phys. D: Appl. Phys. 43, 065402 (5pp),2010

[114] Je-Hyung Kim , Donia Elmaghraoui , Mathieu Leroux, Maxim Korytov, Philippe Vennéguès, Sihem Jaziri, Julien Brault and Yong-Hoon Cho, "Strain- and surface-induced modification of photoluminescence from self-assembled GaN/Al0.5Ga0.5N quantum dots: strong effect of capping layer and atmospheric condition" Nanotechnology 25, 305703, 2014

[115] Takuya Kawazu, Takeshi Noda, Takaaki Mano, Yoshiki Sakuma, and Hiroyuki Sakaki, "Growth and optical properties of GaSb/GaAs type-II quantum dots with and without wetting layer" Japanese Journal of Applied Physics 54, 04DH01,2015

[116] V K Dixit, S Porwal, S D Singh, T K Sharma, Sandip Ghosh and S M Oak, "A versatile phenomenological model for the S-shaped temperature dependence of photoluminescence energy for an accurate determination of the exciton localization energy in bulk and quantum well structures" J. Phys. D: Appl. Phys. 47, 065103 (14pp), 2014

[117] Eunsoon Oh, Hyeongsoo Park and Yongjo Park, "Influence of potential fluctuation on optical and electrical properties in GaN" Appl. Phys. Lett. 72, 1848 1998

[118] Guo-En Weng, Wan-Ru Zhao, Shao-Qiang Chen, Hidefumi Akiyama, Zeng-Cheng Li, Jian-Ping Liu and Bao-Ping Zhang, "Strong localization effect and carrier relaxation dynamics in self-assembled InGaN quantum dots emitting in the green" Weng et al. Nanoscale Research Letters,2015

[119] P. D. Hodgson, R. J. Young, M. Ahmad Kamarudin, Q. D. Zhuang, and M. Hayne, "Hole migration and optically induced charge depletion in GaSb/GaAs wetting layers and quantum rings" Physical review B 88, 155322,2013

[120] N.S. Beattie,n , G. Zoppi , P. Se , I. Farrer , M. Duchamp, D.J. Morrison, R.W. Mile, D.A. Ritchie, "Analysis of InAs/GaAs quantum dot solar cells using Suns-V_{oc} measurements" Solar Energy Materials & Solar Cells 130,241–245, 2014

[121] Geller M, Kapteyn C, M"uller-Kirsch L, Heitz R and Bimberg D, "450 meV hole localization in GaSb/GaAs quantum dots" Appl. Phys. Lett. 82 2707, 2003

[122] Hwang J, Martin A J, Millunchick J M and Phillips J D, " Hwang J, Martin A J, Millunchick J M and Phillips J D" J. Appl. Phys. 111 0745142012 J. Appl. Phys. 111 074514, 2012

[123] Priyanka Singh n, N.M. Ravindra," Temperature dependence of solar cell performance an aQDnalysis" Solar Energy Materials & Solar Cells 101,36–45, 2012

[124] G. Landis, "Review of Solar Cell Temperature Coefficients for Space," Proc. XIII Space Photovoltaic Research and Technology Conference, NASA CP-3278, NASA Lewis Research Center, 385-400, 1994.

[125] Hao Feng Lu, Lan Fu, Greg Jolley, Hark Hoe Tan, Sudersena Rao Tatavarti, and Chennupati Jagadish, "Temperature dependence of dark current properties of InGaAs/GaAs quantum dot solar cells" APPLIED PHYSICS LETTERS 98, 18350920

[126] R. Kachare, B. E. Anspaugh, and G. F. J. Garlick, Solid-State Electron. 31, 159 1988

[127] Nowozin T, Marent A, Bonato L, Schliwa A, Bimberg D, Smakman EP et al. "Linking structural and electronic properties of high-purity self-assembled GaSb/GaAs quantum dots". Physical review b. Jul 6; 86(3): 035305, 2012

[128] Hiromi Fujita, Peter J. Carrington, Magnus C. Wagener, Johannes R. Botha, Andrew R. J. Marshall, Juanita James, Anthony Krier, Kan-Hua Lee and Nicholas John Ekins-Daukes, "Open-circuit voltage recovery in type II GaSb/GaAs quantum ring solar cells under high concentration" Prog. Photovolt: Res. Appl., 2015

[129] Hiromi Fujita, Juanita James, Peter J Carrington, Andrew R J Marshall, Anthony Krier, Magnus C Wagener and Johannes R Botha, "Carrier extraction behaviour in type II GaSb/GaAs quantum ring solar cells" Semicond. Sci. Technol. 29, 035014, 2014

[130] Skolnick, M.S., Mowbray, D.J.: 'Self-assembled semiconductor quantum dots: fundamental physics and device applications', Annu. Rev. Mater. Res., 34, pp. 181–218, 2004

[131] Stephen J Polly, David V Forbes, Kristina M Driscoll, Seth M Hubbard 'Delta Doping Effects on Quantum Dot Solar Cells' IEEE journal of Photovoltaics Vol.4,No.4.

[132] K. Sablon, J. Little, V. Mitin, A. Sergeev, N. Vagidov, and K. Reinhardt, "Strong Enhancement of Solar Cell Efficiency Due to Quantum Dots with Built-In Charge", NanoLett., 11, pp. 2311-2317, 2011.

[133] N. Fernández-Delgado∗ M. HerreraS.I. Molina,C. Castro S. Duguay J.S. James, A. Krier "Effect of doping on the morphology of GaSb/GaAs nanostructures for solar cells" Applied Surface Science 359, 676–678, 2015

[134] R. Songmuang, S. Kiravittaya, O.G. Schmidt, Shape evolution of InAs quantumdots during overgrowth, J. Cryst. Growth 249, 416–421, 2003.

[135] Skolnick, M.S., Mowbray, D.J.: 'Self-assembled semiconductor quantum dots: fundamental physics and device applications', Annu.Rev. Mater. Res., 34, pp. 181–218, 2004

[136] Diego Alonso-Álvarez, Benito Alén, Jorge M. García, and José M. Ripalda, "Optical investigation of type II GaSb/GaAs self-assembled quantum dots" Applied physics letters 91, 263103, 2007

[137] Hiromi Fujita, Juanita James, Peter J Carrington, Andrew R J Marshall, Anthony Krier, Magnus C Wagener and Johannes R Botha, "Carrier extraction behaviour in type II GaSb/GaAs quantum ring solar cells" Semicond. Sci. Technol. 29 035014 (5pp), 2014

[138] Tian Li and Mario Dagenais, "Below-bandgap absorption in InAs/GaAs self-assembledmquantum dot solar cells" Prog. Photovolt: Res. Appl., 2014

[139] Alén B, Bickel F, Karrai K, Warburton RJ, Petroff PM. "Stark-shift modulation absorption spectroscopy of single quantum dots". Applied Physics Letter; 83: 2235–7. DOI: 10.1063/1.1609243, 2003

[140] Birkedal D, Bloch J, Shah J, Pfeiffer LN,West K. "Femtosecond dynamics and absorbance of self-organized InAs quantum dots emitting near 1.3 μm at room temperature". Applied Physics Letters; 77: 2201–2203, 2000

[141] Harbord E, Spencer P, Clarke E, Murray R. "Radiative lifetimes in undoped and p-doped InAs/GaAs quantum dots" Physical Review B; 80: 195312. DOI: 10.1103/PhysRevB.80.195312, 2009

[142] D. Bimberg, M. Grundmann, and N. N. Ledentsov, "Quantum Dot Heterostructures" (John Wiley & Sons, Chichester, 2001.

[143] A. J. Martin, J. Hwang, E. A. Marquis, E. Smakman, T. W. Saucer, G. V. Rodriguez, A. H. Hunter, V. Sih, P. M. Koenraad, J. D. Phillips, and J. Millunchick, " The disintegration of GaSb/GaAs nanostructures upon capping " Appl. Phys. Lett. 102, 113103, 2013

[144] M. C. Wagener, P. J. Carrington, J. R. Botha, and A. Krier, "Simulation of the enhanced infrared photoresponse of type-II GaSb/GaAs quantum ring solar cells" APPLIED PHYSICS LETTERS 103, 063902, 2013

[145] M. Geller, C. Kapteyn, L. Muller-Kirsch, R. Heitz, and D.Bimberg, "450 meV hole localization in GaSb/GaAs quantum dots," Applied Physics Letters, vol. 82, no. 16, pp. 2706–2708, 2003

[146] T. Nowozin, A. Marent, L. Bonato et al., "Linking structural and electronic properties of high-purity self-assembled GaSb/GaAs quantum dots," Physical Review B, vol. 86, no. 3, Article ID 035305, 6 pages, 2012

[147] T. Nowozin, A. Wiengarten, L. Bonato, D. Bimberg, Wei-Hsun Lin, Shih-Yen Lin, M. N. Ajour, K. Daqrouq, and A. S. Balamesh, "Electronic Properties and Density of States of Self-Assembled GaSb/GaAs Quantum Dots" Journal of Nanotechnology, Article ID 302647, 2013